Electronic Transport Properties of Strained Graphene Nanostructures

Diana Alexandra Gradinar

PhD Thesis

Submitted for the degree of Doctor of Philosophy

October 29, 2013

Declaration

Except where stated otherwise, this thesis is a result of the author's original work and has not been submitted in whole or in part for the award of a higher degree elsewhere. This thesis documents work carried out between September 2009 and August 2013 at Lancaster University, UK, under the supervision of Prof. V. I. Fal'ko and Prof. H. Schomerus.

Part of Chapter 2 has been published as D. A. Gradinar, M. Mucha-Kruczyński, H. Schomerus, and V. I. Fal'ko, *Transport signatures of pseudomagnetic Landau levels in strained graphene ribbons*, Phys. Rev. Lett. **110**, 266801 (2013). A longer paper, D. A. Gradinar, M. Mucha-Kruczyński, H. Schomerus, and V. I. Fal'ko, *Strain-induced modifications in the transport properties of graphene nanoribbons*, is ready for submission to Phys. Rev. B.

Chapter 3 is based on the original paper D. A. Gradinar, H. Schomerus, and V. I. Fal'ko, *Conductance anomaly near the Lifshitz transition in strained bilayer graphene*, Phys. Rev. B **85**, 165429 (2012).

Chapter 4 describes preliminary results of a project done in collaboration with J. R. Wallbank.

Diana Alexandra Gradinar

October 29, 2013

Acknowledgements

I would like to thank my supervisors Prof. V. I. Fal'ko and Prof. H. Schomerus for their guidance, support, and encouragement throughout the work done during my PhD. I would also like to thank my collaborators Dr. C. J. Pool, Dr. M. Mucha-Kruczyński, J. R. Wallbank, Dr. V. Cheianov for insightful discussions and advice given in various stages of my work.

Thanks to all my friends in the department for making this journey a fun experience by dragging me into Gradbar every Friday. Finally, I am truly grateful for all the help and support received from my parents and my husband, whom have been there for me every step of the way. Thank you!

Abstract

In this thesis we theoretically investigate the influence of mechanical deformations on the electronic transport properties of graphene structures, such as nanoribbons, bilayer graphene, and graphene on hexagonal boron nitrite substrates.

We find that homogeneous mechanical deformations can induce the formation of zero-conductance plateaus and conductance resonances in nanoribbons, and outline their robustness in the presence of 'double atom' edge disorders. Furthermore we emphasize that even small percentages of 'single atom' edge defects are strong enough to determine the smearing or even suppression of the observed resonant structure. For the case of inhomogeneous deformations we find that the inhomogeneity developed near the contacts aids the resonant transmission of charge carriers through a mode mixing mechanism or via the sublattice-polarized $n = 0$ pseudo-magnetic Landau level.

We also show that in homogeneously strained bilayer graphene the linear response conductance of an *n-p-n* junction has a non-monotonic dependence on doping and temperature, which varies in size and form as a function of the crystallographic orientation of the principal strain axis. We find that uniaxial strain changes the chirality of the electronic plane-wave states in the vicinity of the Lifshitz transition in the low-energy electron spectrum of this crystal, which results in the observed non-monotonicity of the linear response conductance.

Finally, we show that mechanical deformations alter the beating of the lattice mismatch in graphene and hexagonal boron nitride heterostructures, which leads to the formation of strained moiré superlattices. We observe that in some cases this determines the opening of minigaps in the second generation mini Dirac cones and finalize our study by identifying an extreme parametric regime where the moiré patterns become quasi-1D and the dispersion acquires additional Dirac cones.

Contents

List of Figures

List of Tables

Chapter 1

Introduction

Graphene is a one-atom thick crystalline membrane, formed of carbon atoms arranged in a honeycomb lattice. Even though carbon fibers have been studied and used since the 19^{th} century [100], before 2004 graphene was only studied theoretically as a starting point for describing properties of various carbon based materials. It was only after 2004, when A. Geim and K. Novoselov from the University of Manchester succeeded in isolating the first 2D layer of carbon atoms, that graphene physics [20, 39] became an active and rapidly expanding field of research in condensed matter rather than simply a toy model. This is largely due to the fact that graphene uniquely combines a series of properties such as mechanical strength, high electronic and thermal conductivities and impermeability, properties which make this material a suitable candidate for numerous future applications [84].

The fact that controlled deformations that result in measurable effects [80, 82] can be produced in this material has created a wave of excitement among theorists and experimentalists alike due to the peculiar way in which strain affects the already unusual electronic properties of graphene. Motivated by these recent discoveries, the work presented in this thesis is focused on the theoretical investigation of the transport properties of strained graphene structures such as nanoribbons, bilayer graphene, and monolayer graphene on hexagonal boron nitride substrates. We start by giving a brief introduction in **Chapter 1** to graphene physics and the systems that will be discussed in detail later on.

Graphene membranes suspended over metallic contacts may undergo unintentional mechanical deformations during the fabrication process. Using the recursive Green's function method for graphene ribbons, we systematically investigate the effect of both homogeneous and inhomogeneous deformations on the conductance of ballistic *n*-*p*-*n* junctions, as presented in **Chapter 2**. Here, we show that under small homogeneous strains the conductance of such devices can decrease, acquire a resonant structure, or be completely suppressed, depending on the amount of strain. Inhomogeneous deformations, on the other hand, act as valley-antisymmetric pseudo-magnetic fields which lead to the formation of localized states at the neutrality point. The peculiar $n = 0$ pseudo-magnetic Landau level can manifest itself in the transport characteristics of such ribbons, via two groups of low-energy conductance resonances.

Strain qualitatively changes the low-energy band structure of bilayer graphene, leading to the appearance of a pair of low-energy Dirac cones near each corner of the Brillouin zone, and a Lifshitz transition, (a saddle point in the dispersion relation) at an energy proportional to the strain [76]. In **Chapter 3**, we show that in the vicinity of the Lifshitz transition the conductance of a ballistic n-p and n-p-n junction exhibits an anomaly: a non-monotonic temperature and chemical potential dependence, with the size depending on the crystallographic orientation of the principal axis of the strain tensor. This effect is characteristic for junctions between regions of different polarity (*n*-*p* and *n*-*p*-*n* junctions), while there is no anomaly in junctions between regions of the same polarity (*n*-*n*′ and *n*-*n*′-*n* junctions).

Superlattices (SL) have been thought to provide the necessary means of controlling graphene's electronic spectrum. In **Chapter 4** we discuss the qualitative changes that emerge in the dispersion of monolayer graphene under the influence of two distinct SL structures. First we consider a periodic modulation of the electrostatic potential profile, formed of a periodically spaced square barrier system (an infinite series of *n*-*p*-*n* junctions), and find that it generates the appearance of pairs of Dirac points (DPs) in the electronic spectrum. We also outline the conditions

for the appearance of each pair, and discuss their position on the energy axes. We then continue our analysis and consider spatially periodic lattice potentials. Using a general symmetry based approach, we study the generic miniband structure for electrons in homogeneously strained monolayer graphene placed on a hexagonal boron nitride substrate. In particular we find that mechanical deformations couple to the misalignment angle between the two honeycomb lattices, alters the beating of the lattice mismatch, and leads to the formation of strained moiré superlattices. Furthermore, we identify an extreme regime where the moiré patterns become pseudo-1D and outline their effect on the electronic spectrum.

1.1 Monolayer Graphene

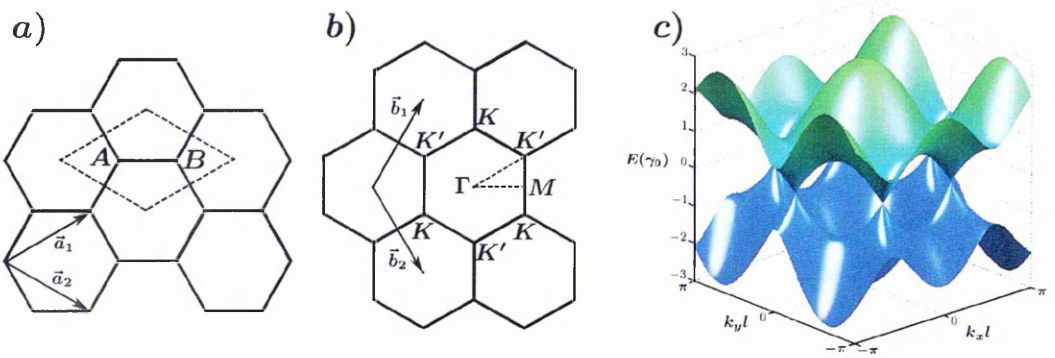

Figure 1.1: a) Real space hexagonal lattice and unit cell (dashed rhombus), b) the Brillouin zone, and c) the energy dispersion for π bands of two-dimensional graphite (graphene).

Graphene is the first known truly two-dimensional material, which possess an unusual electronic band structure: its valence and conduction bands cross at the corners of the hexagonal Brillouin zone [100] of the honeycomb lattice see Fig. 1.1(a, b). The crossing of the two bands occurs exactly at the Fermi level of neutral graphene, which makes this material a zero-gap semiconductor.

To describe graphene, we choose vectors $\vec{a}_1$ and $\vec{a}_2$ as our in-plane primitive lattice vectors and a rhombic unit cell as shown in Fig. 1.1(a). The corresponding reciprocal lattice vectors and the hexagonal Brillouin zone (BZ) are shown in Fig. 1.1(b). In the x, y coordinates the real space unit vectors of the hexagonal lattice are expressed as

$$\vec{a}_1 = \left(\frac{3}{2}l, \frac{\sqrt{3}}{2}l\right), \quad \vec{a}_2 = \left(\frac{3}{2}l, -\frac{\sqrt{3}}{2}l\right)$$

where $l = 1.42\text{Å}$ is the bond length between two adjacent sites. Consequently the reciprocal unit vectors can be found by imposing $\vec{b}_i \cdot \vec{a}_j = 2\pi\delta_{i,j}$, where $i, j = 1, 2$, and are

$$\vec{b}_1 = \left(\frac{2\pi}{3l}, \frac{2\pi}{\sqrt{3}l}\right), \quad \vec{b}_2 = \left(\frac{2\pi}{3l}, -\frac{2\pi}{\sqrt{3}l}\right). \tag{1.1}$$

We denote the two inequivalent corners of the Brillouin zone as $\boldsymbol{K}$ [at position $\boldsymbol{K} = (0, 4\pi/3\sqrt{3}l)$] and $\boldsymbol{K'}$ [at the position $\boldsymbol{K'} = (0, -4\pi/3\sqrt{3}l)$].

The basis functions of $2D$ graphite are given by the Bloch functions of the inequivalent A and B sites (the directions of their bonds to nearest neighbors are different). Then, the transfer integral matrix and the overlap integral matrix are given by [100]

$$\mathcal{H} = \begin{pmatrix} \varepsilon_{2p} + V_g & f \\ f^* & \varepsilon_{2p} + V_g \end{pmatrix}, \quad S = \begin{pmatrix} 1 & sf \\ sf^* & 1 \end{pmatrix}, \quad f = \gamma_0 \sum_{i=1}^{3} e^{i\vec{k}\cdot\vec{R}_i}, \tag{1.2}$$

respectively, where ε_{2p} is the orbital energy of the $2p$ level and V_g is the on-site potential energy. In f we perform the summation over the phase factors $e^{i\vec{k}\cdot\vec{R}_i}$ where $i = 1, \cdots, 3$ label the three nearest neighbor B atoms relative to an A atom, positioned at $\vec{R}_i$. Assuming $\varepsilon_{2p} = s = 0$ [When the overlap integrals become zero, the bonding π and anti-bonding π^* bands become symmetrical around $E = \varepsilon_{2p}$.]), the transfer integral and overlap integral matrices in momentum space become [100]

$$\mathcal{H} = \begin{pmatrix} V_g & f \\ f^* & V_g \end{pmatrix}, \quad S = \begin{pmatrix} 1 & 0 \\ 0 & 1 \end{pmatrix}. \tag{1.3}$$

Solving the secular equation $det(\mathcal{H} - ES) = 0$ one finds the energy dispersion[99] in Fig. 1.1(c),

$$E = V_g - \eta|f|, \quad \eta = \begin{cases} +1 & \text{valence } (\pi \text{ bonding}) \\ -1 & \text{conduction } (\pi^* \text{ anti-bonding}), \end{cases} \quad |f| = \sqrt{ff^*}. \tag{1.4}$$

Setting $V_g = 0$ and expanding f in terms of small deviations in momentum around the $\boldsymbol{K}$ point, one obtains Dirac-like Hamiltonian [122] describing the low-energy quasiparticles in graphene

$$\mathcal{H} = v \begin{pmatrix} 0 & p_x - ip_y \\ p_x + ip_y & 0 \end{pmatrix} = v\boldsymbol{\sigma} \cdot \boldsymbol{p}, \tag{1.5}$$

where $\boldsymbol{p}$ is a two dimensional quasiparticle momentum, $\boldsymbol{\sigma}$ are the two-dimensional Pauli matrices, and $v = \frac{3}{2}\gamma_0 l$ is the Fermi velocity which plays the role of the

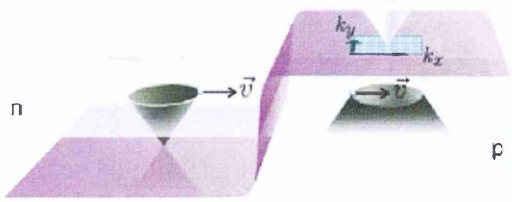

Figure 1.2: Sketch of an n-p interface in monolayer graphene (the picture is adopted from Ref. [26]).

speed of light with $\gamma_0 = 3\text{eV}$ as the hopping between adjacent sites. As it can be seen from Fig. 1.1(c), the spectrum of graphene is linear (approximately conical in shape) up to energies of about 1eV. The sublattice composition of the electronic Bloch states in graphene is fixed to the direction of their propagation , making charge carriers in monolayer and bilayer graphene 'chiral'. Therefore the projection of the 'isospin' operator, $\boldsymbol{\sigma}$, on the direction of motion, $\boldsymbol{p}$, takes the values ± 1 for electrons in the conduction bands ($E = vp$) and in the valence bands ($E = -vp$) respectively.

The absence of a gap enables one to vary the carrier density continuously from the valence to the conduction bands (from electrons to holes) by using external gates (or chemical doping). Two particular device designs that we consider in this thesis are a) suspended graphene controlled by suspended gates and b) graphene sandwiched between two hexagonal boron nitride films, with the layer on top used as a gate. Using such methods in different regions of the graphene flake, the doping in each region can be controlled independently to create n-doped or p-doped regions and obtain n-n'-n, n-p-n, or p-p'-p junctions (see Fig. 1.2 for an example of an n-p junction). Transport through such junctions will be discussed in detail throughout Chapters 2 and Chapter 3.

In contrast to conventional semiconductors, where an n-p junction is impenetrable for electrons due to the large band gaps in the electronic spectrum, it was realized [25, 26] that electron transmission through the interface between n and p-doped regions of graphene mimics optical refraction from materials with negative refractive index [91, 92]. This is because, in graphene, scattering on an electrostatic potential that is smooth on the scale of the lattice constant, preserves

the isospin (sublattice composition of Bloch states) of electrons, and therefore perfect backscattering, which requires inversion of isospin, is forbidden [106]. To satisfy this condition and keep the sign of the carrier's group velocity fixed when traversing the interface, the sign of the momentum must change. Therefore in the n-doped region $\mathcal{H} = v\boldsymbol{\sigma} \cdot \boldsymbol{p} = vp\boldsymbol{\sigma} \cdot \hat{\boldsymbol{n}}$, with $\boldsymbol{\sigma} \cdot \hat{\boldsymbol{n}} = 1$, and the charge carriers are electrons, whereas in the p-doped region $\boldsymbol{\sigma} \cdot \hat{\boldsymbol{n}} = -1$ and the charge carriers are holes. This effect, of perfect transmission at zero angle of incidence through an n-p-n junctions is known as Klein tunneling [47, 115] and it reflects the fact that a ballistic p-type region of graphene separating two n-type regions may act as an electrostatically controlled lens for electrons [Note that in monolayer graphene fermions exhibit chiralities that resemble those associated with spin 1/2] [73, 85].

1.2 Bilayer Graphene

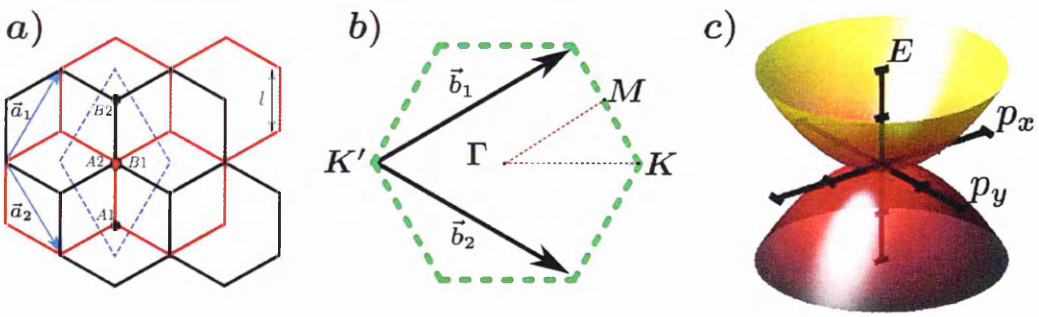

Figure 1.3: a) Schematic depiction of the bilayer graphene crystal lattice, where the top/bottom layer is shown in black/red, and the unit cell is the dashed blue rhombus. The real primitive lattice vectors are $\vec{a_1}$ and $\vec{a_2}$. b) The Brillouin zone is shown as a dashed green hexagon with the respective high symmetry points represented by $\boldsymbol{\Gamma}$, $\boldsymbol{M}$, $\boldsymbol{K}$ and $\boldsymbol{K'}$, and the reciprocal lattice vectors $\vec{b_1}$ and $\vec{b_2}$. c) The parabolic low-energy dispersion of bilayer graphene (trigonal warping has been neglected).

Bilayer graphene exhibits equally unusual electronic properties. Its high energy band structure is similar to that of monolayer graphene, however its low energy band structure is parabolic with massive quasiparticles rather than linear with massless quasiparticles.

We model bilayer graphene as two weakly-coupled monolayers of graphene, separated by a distance of $\approx 3.35\text{Å}$ [107], and arranged according to Bernal (AB)

stacking [8, 33]. We choose vectors $\vec{a}_1$ and $\vec{a}_2$ as our in-plane primitive lattice vectors and a rhombic unit cell as shown in Fig. 1.3(a). The corresponding reciprocal lattice vectors and Brillouin zone are shown schematically in Fig. 1.3(b), where $\vec{b}_1$ and $\vec{b}_2$ can be found by imposing that $\vec{b_i} \cdot \vec{a_j} = 2\pi\delta_{ij}$. We denote the two inequivalent corners of the Brillouin zone as $\boldsymbol{K}$ [at position $\boldsymbol{K} = (4\pi/3\sqrt{3}l, 0)$] and $\boldsymbol{K'}$ [at the position $\boldsymbol{K'} = (-4\pi/3\sqrt{3}l, 0)$].

The low-energy properties of bilayer graphene, near the $\boldsymbol{K}$ point, are described by the Hamiltonian

$$\mathcal{H} = -\frac{\hbar^2}{2m_e}\begin{pmatrix} 0 & (p_x - ip_y)^2 \\ (p_x + ip_y)^2 & 0 \end{pmatrix}, \tag{1.6}$$

where m_e is the electron mass. This effective Hamiltonian describes the electronic dispersion for energies close to the neutrality point while neglecting the higher energy bands or trigonal warping [32, 112]. The resulting electronic dispersion is given by

$$E = \pm\frac{\hbar^2}{2m_e}(p_x^2 + p_y^2), \tag{1.7}$$

in agreement with [72]. The energy dispersion shown in Fig. 1.3(c) consists of valley-degenerate bands which touch at the $\boldsymbol{K}$ or $\boldsymbol{K'}$ points. In contrast to monolayer graphene, where the low-energy dispersion is difficult to alter, the energy bands in bilayer graphene (conduction and valence bands) can be split by introducing an external transverse electric field [20, 71, 74, 86], or qualitatively altered by means of induced mechanical deformations [76].

In contrast to monolayer graphene, where an n-p junction can act as a focusing lens for electrons, in bilayer graphene massive chiral fermions are always perfectly reflected for angles close to normal incidence [47, 115]. The perfect reflection, as opposed to perfect transmission, can be understood as yet another facet of the Klein paradox since this effect is due to the charge-conjugation symmetry (in bilayer graphene fermions exhibit chiralities that resemble those associated with spin 1) [73, 85]. In this case the charge conjugation requires that a propagating electron with wavevector k transforms into a hole with wavevector ik (rather than

$-k$ as in the case of monolayer graphene) which is an evanescent wave inside the electrostatic barrier. However, depending on the ratio between the electrostatic potential and the energy of incoming electrons, there are angles at which perfect transmission can indeed occur [96] due to multiple reflections between the n-p and p-n interfaces which lead to the formation of Fabry-Pérot-like standing waves.

1.3 Graphene nanoribbons

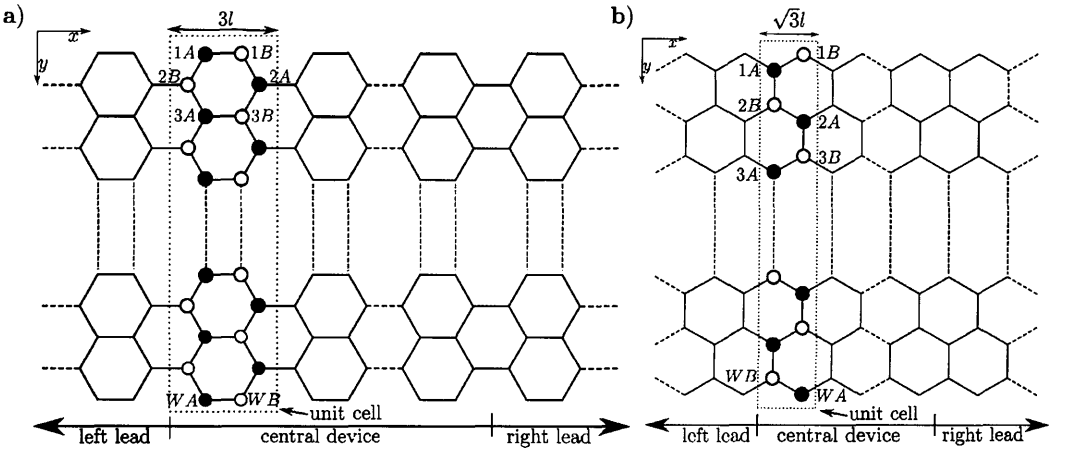

Figure 1.4: Structure of the graphene nanoribbon junctions with a) armchair boundaries (A-GNR) and b) zigzag boundaries (Z-GNR). Each ribbon is comprised of two ideal leads (left and right), and a central conductor. The dotted rectangles denote the respective unit cells and $W_{A/Z}$ defines the ribbon width.

The tight-binding Hamiltonian [99, 120] of graphene nanoribbon (GNR) junctions with armchair and zigzag houndaries, shown in Fig. 1.4, is given by

$$\mathcal{H} = \sum_i V_i c_i^\dagger c_i + \sum_{\langle ij \rangle} \gamma_{ij} c_i^\dagger c_j, \tag{1.8}$$

where c_i is a fermionic annihilation operator acting on a site i, $\langle ij \rangle$ denotes pairs of nearest neighbors, V_i is the on-site potential and the hopping matrix element is $\gamma_{ij} = \gamma_0 = 3\text{eV}$. The chemistry of the graphene strip edges (armchair (A-GNR) or zigzag (Z-GNR)), strongly influences the low-energy spectrum of the π-electrons. Similarly to the case of carbon nanotubes, the electronic band structure of graphene ribbons with armchair edges can be determined by making the

transverse wave number discrete in accordance with the boundary conditions. For ribbons with zigzag edges, on the other hand, the electronic band structure is not easy to find because the transverse wave number depends not only on the width of the ribbon, but also on the longitudinal wave number [99]. Thus, Z-GNR are not analogous to carbon nanotubes. This type of ribbons also possess localized edge states with energies close to the Fermi level, which are absent for ribbons with armchair boundaries [120]. These properties of A-GNR and Z-GNR will be discussed at length in the following sections.

The model we employ to study size and edge effects of graphene nanoribbons is shown in Fig. 1.4 (a-b). The width of the ribbons, W_A and W_Z, are determined by the number of dimer (two carbon site) lines for the armchair nanoribbons and the number of zigzag lines for zigzag nanoribbons [120]. The lengths are measured in terms of translational unit cells (dotted rectangles) comprising the ribbons, which are denoted by L_A and L_Z. Then the width and length of a ribbon in units of interatomic distance is $\mathcal{W}_A = \sqrt{3}W_A l$ with $\mathcal{L}_A = 3L_A l$ and $\mathcal{W}_Z = \left(\frac{3W_Z}{2} - 1\right) l$ with $\mathcal{L}_Z = \sqrt{3}L_Z l$ for armchair and zigzag edges respectively. Here $l = 1.42\text{Å}$ is the interatomic distance between neighboring sites.

1.3.1 Armchair nanoribbons

Brillouin Zone (BZ)

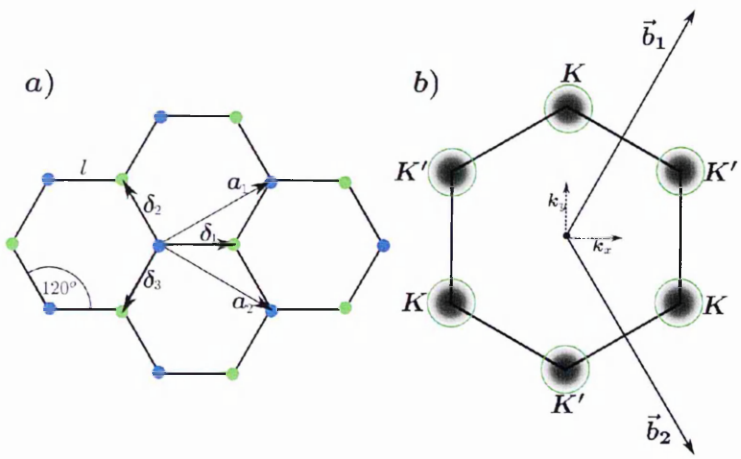

Figure 1.5: a) Real space hexagonal lattice and b) the Brillouin zone of armchair graphene ribbons.

In Fig. 1.5 we show (a) the unit cell and (b) the Brillouin zone of the A-GNR, where $\vec{a_1}$ and $\vec{a_2}$ are unit vectors in real space and $\vec{b_1}$ and $\vec{b_2}$ are reciprocal lattice vectors. In the cartesian coordinates, the real space unit vectors of the hexagonal lattice and the reciprocal unit vectors are

$$\vec{a}_1 = \left(\frac{3}{2}l, \frac{\sqrt{3}}{2}l\right), \quad \vec{a}_2 = \left(\frac{3}{2}l, -\frac{\sqrt{3}}{2}l\right)$$
$$\vec{b}_1 = \left(\frac{2\pi}{3l}, \frac{2\pi}{\sqrt{3}l}\right), \quad \vec{b}_2 = \left(\frac{2\pi}{3l}, -\frac{2\pi}{\sqrt{3}l}\right).$$

Two inequivalent high symmetry points are defined at the corners of the BZ, and are then located at $\boldsymbol{K} = \left(0, \frac{4\pi}{3\sqrt{3}l}\right)$ and $\boldsymbol{K'} = \left(0, -\frac{4\pi}{3\sqrt{3}l}\right)$ respectively.

Dispersion

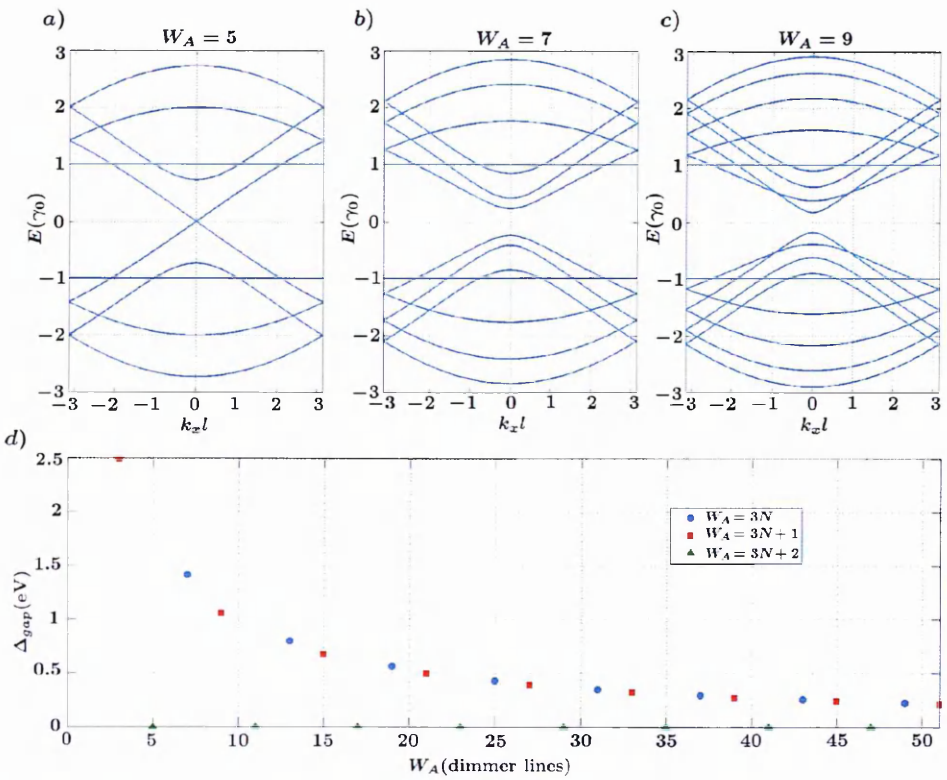

Figure 1.6: a-c) Dispersions and d) band gap as a function of increasing width, for the three types of A-GNRs numerically obtained using the procedure outlined in Apendix A.

In this work we will only consider the π energy bands because they are covalent and thus the most significant in determining the solid state electronic properties

of graphene [100]. As such, considering the contribution of the three nearest neighbors [see Fig. 1.5(a)],

$$\vec{\delta_1} = l\,(1,0)\,, \quad \vec{\delta_2} = \frac{l}{2}\left(-1,\sqrt{3}\right), \quad \vec{\delta_3} = \frac{l}{2}\left(-1,-\sqrt{3}\right), \tag{1.9}$$

we can explicitly find that $f = \gamma_0\left(e^{-ik_x l} + 2e^{ik_x l/2}\cos\left(\frac{\sqrt{3}l}{2}k_y\right)\right)$ in Eq. (1.4), and consequently, the dispersion is

$$E = V_g - \eta\gamma_0\sqrt{1 + 4\cos\left(\frac{3l}{2}k_x\right)\cos\left(\frac{\sqrt{3}l}{2}k_y\right) + 4\cos^2\left(\frac{\sqrt{3}l}{2}k_y\right)},$$

with $\eta = -(+)$ for the conduction (valence) bands.

Fig. 1.6(a-c) shows the energy band structure of armchair ribbons for three different widths, with the energy E scaled by γ_0. The top of the valence band and bottom of the conduction bands are located at $k = 0$. For this type of ribbons, the hard wall boundary conditions that must be imposed at the top and bottom fee edges lead to a quantization of transverse momentum. Therefore the width of the ribbon determines the conducting properties of the system. As such, A-GNRs are divided into three distinct families: if $W_A = 3N + 2$ with $N \in \mathbb{N}$ then the ribbon is metallic, where as for $W_A = 3N$ and $W_A = 3N + 1$ it is semiconducting. In the case of semiconducting ribbons the band gap, Fig. 1.6(d), decreases with increasing width and approaches zero in the limit of large W_A [110, 120].

Hamiltonian in the continuous model

Expanding f in terms of small deviations in momentum around the K point and making the substitution $k_x \to \delta k_x$ and $k_y \to \frac{4\pi}{3\sqrt{3}l} + \delta k_y$ [were we have assumed

$\delta kl \ll 1$], we get

$$\begin{aligned} f =& \gamma_0 \left(e^{-i\delta k_x l} + 2e^{i\delta k_x l/2} \cos\left(\frac{2\pi}{3} + \frac{\sqrt{3}l}{2}\delta k_y \right) \right) \\ \simeq& \gamma_0 \left((1 - i\delta k_x l) + 2\left(1 + i\frac{1}{2}\delta k_x l\right)\left(-\frac{1}{2} - \frac{3}{4}\delta k_y l\right) \right) \\ \simeq& -\frac{3l}{2}\gamma_0 \left(i\delta k_x + \delta k_y\right), \end{aligned}$$

we obtain the low-energy Hamiltonian at the $\boldsymbol{K}$ point

$$\mathcal{H}_K = -\frac{3l}{2}\gamma_0 \begin{pmatrix} 0 & ik_x + k_y \\ -ik_x + k_y & 0 \end{pmatrix} = v_F\hbar \begin{pmatrix} 0 & -ik_x - k_y \\ ik_x - k_y & 0 \end{pmatrix}, \quad (1.10)$$

where $v_F = \frac{3l\gamma_0}{2\hbar}$ is the Fermi velocity. The low energy Hamiltonian at the $\boldsymbol{K'}$ point is calculated in a similar fashion and is $\mathcal{H}_{K'} = -\mathcal{H}_K$.

Transverse-momentum quantization and waveguide modes

For the above derived Hamiltonian, Eq. (1.10), if the ribbon is taken to be infinite in the x direction, translational invariance ensures that the wave function can be written in the form $\Psi_\mu(\vec{r}) = e^{ik_x x}\phi_\mu(y)$, where $\mu = A, B$ denotes the inequivalent sites. Then writing $\phi = \begin{pmatrix} \phi_A \\ \phi_B \end{pmatrix}$ and imposing $\mathcal{H}\phi = E\phi$ we obtain the following set of coupled equations [16]

$$\begin{cases} (ik_x + i\partial_y)\phi_A = \tilde{E}\phi_B, \\ (-ik_x + i\partial_y)\phi_B = \tilde{E}\phi_A. \end{cases} \Rightarrow \begin{cases} (k_x^2 - \partial_y^2)\phi_A = \tilde{E}^2\phi_A, \\ (k_x^2 - \partial_y^2)\phi_B = \tilde{E}^2\phi_B. \end{cases}$$

where $\tilde{E} = E/\hbar v_F$. Next we try the ansatz $\phi_A = A_1 e^{iky} + B_1 e^{-iky}$ and $\phi_B = A_2 e^{iky} + B_2 e^{-iky}$, where $k = \sqrt{\tilde{E} - k_x^2}$, and impose the armchair boundary conditions $\phi_A(y = 0) = \phi_B(y = 0) = \phi_A(y = \sqrt{3}l(W_A+1)) = \phi_B(y = \sqrt{3}l(W_A+1)) = 0$. Finally we arrive at the quantization condition for the transverse wave number and

mode-profile [102]

$$k_n = \frac{n\pi}{\sqrt{3}l(W_A+1)} \qquad (1.11)$$
$$\Psi_{nm} = \sqrt{\frac{2}{W_A+1}}\sin\left(\frac{nm\pi}{W_A+1}\right),$$

where $n = 1, 2, ..., W_A$ is the mode index. Here we have written the transverse coordinate, in terms of discrete steps $y = m\sqrt{3}l$ where $m = 1, 2, ..., W_A$. Note that the transverse-modes form an orthogonal set $\int \Psi_{nm}\Psi_{nm'} = \delta_{m,m'}$, where n, m are integers.

1.3.2 Zigzag nanoribbons

Brillouin Zone (BZ)

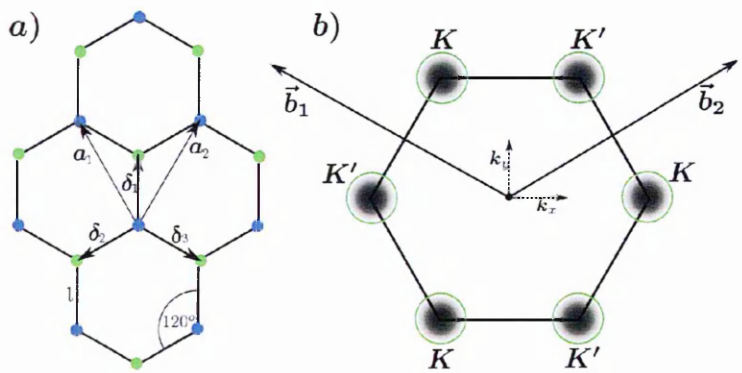

Figure 1.7: a) Real space hexagonal lattice and b) the Brillouin zone of zigzag graphene ribbons.

In Fig. 1.7 we show (c) the unit cell and (d) the BZ of the Z-GNR, where $\vec{a_1}$ and $\vec{a_2}$ are unit vectors in real space and $\vec{b_1}$ and $\vec{b_2}$ are reciprocal lattice vectors. In the cartesian coordinates, the real space and the reciprocal space unit vectors of the hexagonal lattice are

$$\vec{a}_1 = \left(-\frac{\sqrt{3}}{2}l, \frac{3}{2}l\right), \quad \vec{a}_2 = \left(\frac{\sqrt{3}}{2}l, \frac{3}{2}l\right) \qquad (1.12)$$
$$\vec{b}_1 = \left(-\frac{2\pi}{\sqrt{3}l}, \frac{2\pi}{3l}\right), \quad \vec{b}_2 = \left(\frac{2\pi}{\sqrt{3}l}, \frac{2\pi}{3l}\right)$$

respectively. Consequently, the two inequivalent high symmetry points, at the corners of the BZ, are located at $\boldsymbol{K} = \left(\frac{4\pi}{3\sqrt{3}l}, 0\right)$ and $\boldsymbol{K'} = \left(-\frac{4\pi}{3\sqrt{3}l}, 0\right)$.

Dispersion

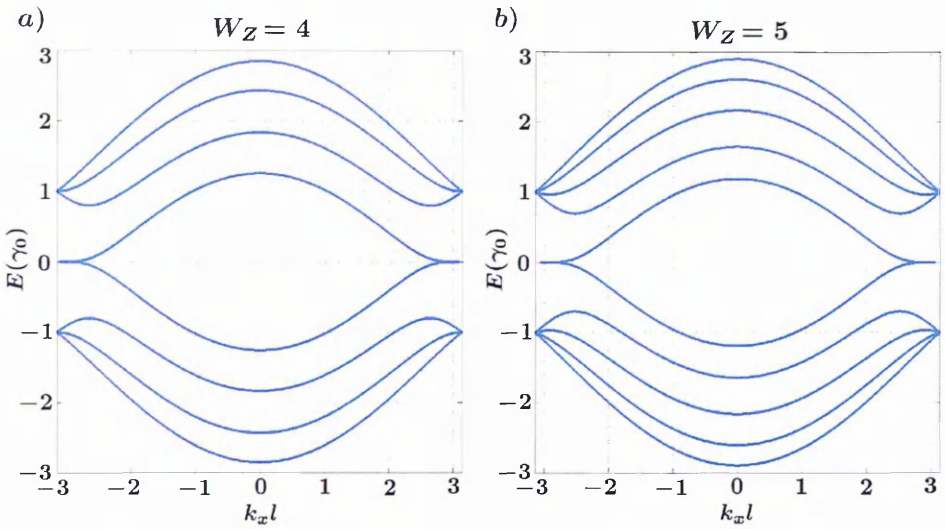

Figure 1.8: a-b) Dispersions for two Z-GNRs of different widths.

As in the case of A-GNR, the contribution of the three nearest neighbors [see Fig. 1.7(a)],

$$\vec{\delta_1} = l\,(0,1)\,, \quad \vec{\delta_2} = \frac{l}{2}\left(-\sqrt{3}, -1\right), \quad \vec{\delta_3} = \frac{l}{2}\left(\sqrt{3}, -1\right). \tag{1.13}$$

gives the explicit form of $f = \gamma_0\left(e^{-ik_y l} + 2e^{ik_y l/2}\cos\left(\frac{\sqrt{3}l}{2}k_x\right)\right)$. The dispersion for Z-GNR is then given by

$$E = V_g - \eta\gamma_0\sqrt{1 + 4\cos\left(\frac{3l}{2}k_y\right)\cos\left(\frac{\sqrt{3}l}{2}k_x\right) + 4\cos^2\left(\frac{\sqrt{3}l}{2}k_x\right)},$$

with $\eta = -(+)$ for the conduction (valence) bands.

The band structures of zigzag ribbons for two different widths are shown in Fig. 1.8. As can be seen the zigzag ribbon is metallic for all W_Z. A feature specific for this orientation of edges is the appearance of partially flat bands at the Fermi level, where electrons are strongly localized. The top of the valence band and bottom of the conduction band are always degenerate at $k_x l = \pi$. This degeneracy

does not appear due to an intrinsic property of the band structure, but rather due to the boundary conditions that must be imposed at the top and bottom edges. In contrast to A-GNRs, where the hard wall boundary conditions were imposed on the wave functions on both the A and B sublattices at the two edges, in Z-GNRs the free edges terminate on only the A sublattice at the top edge and only the B sublattice at the bottom edge or *vice versa*. Even though the edge states have a non-bonding character the overlap between the states at opposite edges form a bonding and anti-bonding configuration. This leads to the formation of the edge states, and therefore, a single transport channel for electrons [78, 119–121]. As such, the transport properties of zigzag graphene ribbons are strongly affected by the presence of these edge states.

Hamiltonian in the continuous model

Similarly to the case of A-GNR, to obtain the low energy Hamiltonian, we expand f in terms of small deviations in momentum around the K point. Making the substitution $k_y \to \delta k_y$ and $k_x \to \frac{4\pi}{3\sqrt{3}l} + \delta k_x$, where $\delta k l \ll 1$, we obtain the Hamiltonian

$$\mathcal{H}_K = -\frac{3l}{2}\gamma_0 \begin{pmatrix} 0 & k_x + ik_y \\ k_x - ik_y & 0 \end{pmatrix} = v_F \hbar \begin{pmatrix} 0 & -k_x - ik_y \\ -k_x + ik_y & 0 \end{pmatrix}, \quad (1.14)$$

where $v_F = \frac{3l\gamma_0}{2\hbar}$ is the Fermi velocity; at the K' point $\mathcal{H}_{K'} = -\mathcal{H}_K$.

Quantization of transverse momentum

For the above derived Hamiltonian, Eq. (1.14), if the ribbon is taken to be infinite in the x direction, translational invariance ensures that the wave function can be written in the form $\Psi_\mu(\vec{r}) = e^{ik_x x}\phi_\mu(y)$, where $\mu = A, B$ denotes the sites. Then writing $\phi = \begin{pmatrix} \phi_A \\ \phi_B \end{pmatrix}$ and imposing $\mathcal{H}\phi = E\phi$ we obtain the following set of

coupled equations

$$\begin{cases} (-k_x + \partial_y)\phi_A = \tilde{E}\phi_B, \\ (-k_x - \partial_y)\phi_B = \tilde{E}\phi_A. \end{cases} \Rightarrow \begin{cases} (k_x^2 - \partial_y^2)\phi_A = \tilde{E}^2\phi_A, \\ (k_x^2 - \partial_y^2)\phi_B = \tilde{E}^2\phi_B. \end{cases}$$

where $\tilde{E} = E/\hbar v_F$. Next we try the ansatz $\phi_A = A_1 e^{iky} + B_1 e^{-iky}$ and $\phi_B = A_2 e^{iky} + B_2 e^{-iky}$, where $k = \sqrt{\tilde{E} - k_x^2}$, and impose the zigzag boundary conditions $\phi_A(y = 0) = \phi_B(y = \sqrt{3}l(W_Z + 1)) = 0$. Finally we arrive at the quantization condition given by the following transcendental equation

$$\frac{k_x - ik}{k_x + ik} = e^{-2\sqrt{3}ikl(W_Z+1)}. \tag{1.15}$$

Note that the transverse momentum quantization for Z-GNR is more complex than for A-GNR, and depends not only on the width of the ribbon, but also on the longitudinal wave number, k_x [16, 99].

Chapter 2

Strain-induced modifications of the transport properties of graphene nanoribbons

Monolayer graphene [22] is capable of sustaining reversible deformations in excess of 10% [49, 61, 94] and is, thus, the strongest material ever measured [54]. The fact that controlled deformations, which result in measurable effects [81, 83], can be produced in this one-atom-thick crystalline membrane [14, 17], has created a wave of excitement among theorists and experimentalists alike, due to the peculiar way in which strain affects the already unusual electronic properties of graphene. Since graphene is a material with degenerate valleys in the band structure [46], having a linear dispersion with the valence and conduction bands touching at the Dirac points (DPs) at the inequivalent $\boldsymbol{K}$ and $\boldsymbol{K'}$ corners of the hexagonal Brillouin zone (BZ), the effect of its lattice deformations on electrons is equivalent to that of an effective gauge field [40, 94, 98, 117]. Consequently, homogeneous deformations result in a small shift of the Dirac cones from the corners of the BZ [94], whereas inhomogeneous strain influences the electron motion similarly to a valley-dependent effective pseudo-magnetic field [66, 97, 111]. This new development in graphene research, has led to the proposal of various theoretical setups, aiming at inducing energy gaps [40, 64] in the dispersion by means of strain engineer-

ing, or of controlling the electronic structure [93] by patterning the substrate on which the membrane rests. The study of the strain-modified electronic properties in graphene culminated when recent scanning-tunneling experiments on nanobubbles [56], found in graphene transferred onto a dielectric surface, revealed that even small inhomogeneous deformations can induce the formation of pseudo-magnetic fields that can reach values equivalent to hundreds of Tesla. Such strong fields result in the localization of the electronic states, and lead to the formation of a discrete 'Landau level' (LL) spectrum with the peculiar $n = 0$ LL state positioned at the DP.

Motivated by the recent developments in the production of graphene nanoribbons (GNRs) with high-quality armchair edges, obtained by the oriented growth on patterned SiC substrates [42], etching of graphene samples with catalytic nanoparticles [19], or by using chemical derivation [58], we theoretically investigate the influence of deformations on the transport properties of such structures, an area which, despite the desire of developing graphene nano-sized electronic devices [84], has remained unexplored thus far. In this Chapter, we perform a systematic analysis, within the tight-binding model, of the conductance of armchair GNRs subject to both homogeneous and inhomogeneous longitudinal deformations. Our calculations show that, under small homogeneous deformations the conductance of such ribbons can decrease, acquire a resonant structure, or be completely suppressed, depending on the amount of strain. We also study the robustness of the observed resonances in the presence of edge disorder, and determine that they are destroyed by single-atom edge defects formed by the loss of single atoms at the edges. In contrast, double-atom edge defects, determined by the loss of dimer lines at the edges, do not alter the resonant structure and can even restore the ballistic properties of the ribbon, when the conductance is initially completely suppressed by the deformations. For inhomogeneous strain we show that pseudo-magnetic LL states form in the contact regions of a stretched GNR, and give rise to characteristic signatures in the electronic transport, such as sharp and clearly defined peaks in the conductance. These features can be attributed to Fabry-Pérot-like standing

waves or resonant transmission via pseudo-magnetic Landau levels. The nature of all the observed resonances and conductance peaks is revealed through the local density of states (LDOS) profiles, which we calculate at the energies where these features occur.

All of the above mentioned results, are described in detail in Sections 2.2, in the corresponding subsections, with their graphic representation shown in Figs. 2.2-2.6. The calculations are based on the Landauer-Büttiker approach [18], with the transmission probabilities extracted from the scattering matrix, which is obtained using the recursive Green's function technique (For more details on the procedure see Appendix A.) [28, 99]. Section 2.1 introduces the considered model and identifies the electronic properties of homogeneously and inhomogeneously strained armchair GNRs.

2.1 General Hamiltonian and electronic properties of strained armchair GNRs

We consider a narrow and long strained GNR, clamped to unstrained graphitic leads and suspended over metallic contacts. The ribbon is chosen to have free standing armchair edges along the transport direction y-axis, and contacts with bulk electrodes along the x-axis, as sketched in Fig. 2.1(a). Within the tight-binding model, the ribbon can be described by the Hamiltonian [22]

$$\mathcal{H} = \sum_i V_i c_i^\dagger c_i + \sum_{\langle ij \rangle} \gamma_{ij} c_i^\dagger c_j, \tag{2.1}$$

where c_i is a fermionic annihilation operator acting on a site i and $\langle ij \rangle$ denote pairs of nearest neighbors. For strained monolayer membranes, both the on-site potential V_i as well as the hopping matrix elements γ_{ij} are modified by the deformation of the lattice. In contrast to an unstrained honeycomb lattice, with carbon-carbon bond lengths $r = 1.42\mathring{A}$, here, the on-site potential $V_i = \frac{1}{2} r \frac{\partial \epsilon_c}{\partial r} \mathrm{div} \boldsymbol{u}(\boldsymbol{r}_i)$ is modulated by the displacement field $\boldsymbol{u} = (u_x, u_y)$ of the membrane, where ϵ_c is the on-site

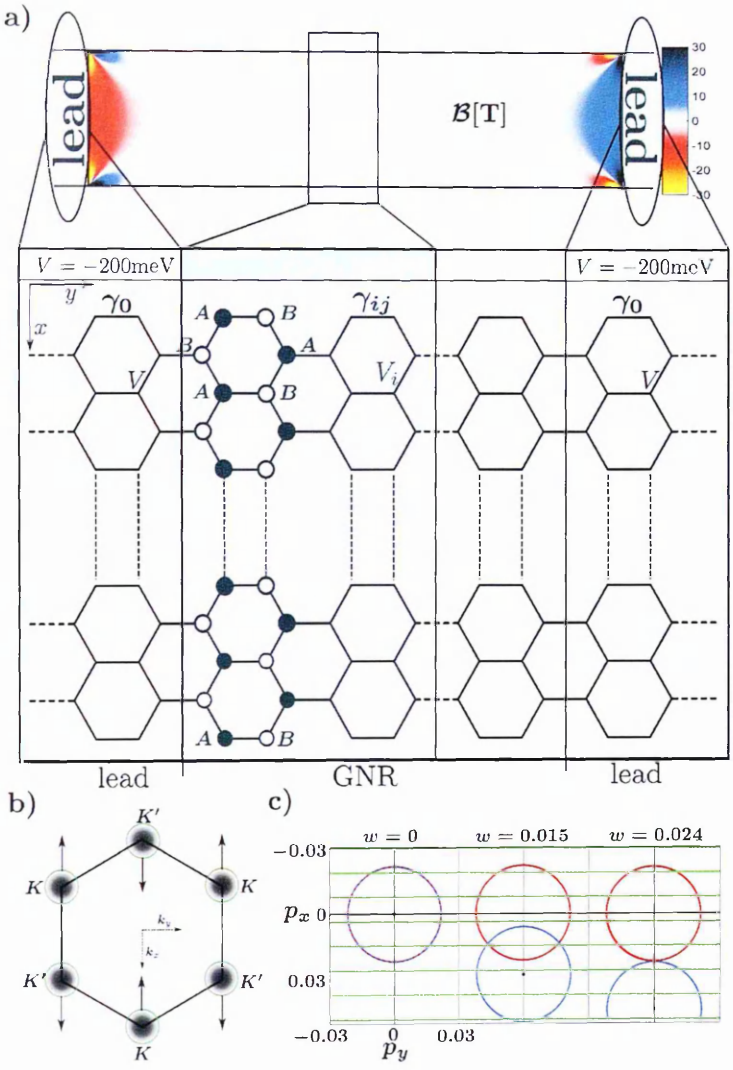

Figure 2.1: Panel (a) shows a sketch of the considered device with the characteristic distribution of the pseudo-magnetic field $\mathcal{B}$(T) for electrons in the $\boldsymbol{K}$ valley for a GNR with $W \simeq 40$nm and aspect ratio $L/W = 4$ with $w = 0.05$ inhomogeneous tensile strain in its middle part. We also sketch the honeycomb lattice corresponding to the tight-binding model in Eq. (2.1), for the two ideal heavily doped leads ($V = -200$meV) and for the central suspended region, in which strain modulates the hopping matrix elements γ_{ij} and the on-site energy V_i. b) Shift of the Dirac cones from the $\boldsymbol{K}$ and $\boldsymbol{K'}$ corners of the Brillouin zone for homogeneously strained armchair GNRs. c) Comparison between Fermi surfaces in the vicinity of the top K point of the BZ, for the GNR in a) with no strain ($w = 0$, red circle) and artificially imposed homogeneous strain ($w = 0.015$, and 0.024, blue circle), at $E_F = 100$meV from the DP. The green lines represent the quantized momenta values of the unstrained GNR.

energy of the electrons. Due to their dependence on the strain-modified distance l_{ij} between lattice sites, the hopping matrix elements $\gamma_0 \approx -3$eV must now be renormalized [94] to

$$\gamma_{ij} = \gamma_0 e^{\eta_0(l_{ij}/r-1)}, \quad l_{ij} \simeq r(1 + \boldsymbol{n}_{ij} \cdot \hat{\boldsymbol{w}}\boldsymbol{n}_{ij}), \tag{2.2}$$

where $\eta_0 = \frac{\partial\gamma_0}{\partial r}\frac{r}{\gamma_0} \approx -3$ relates the change of the nearest neighbor coupling to the change of the bond length [36], $\hat{\boldsymbol{w}}$ is the 2×2 strain tensor $w_{\alpha\beta} = \frac{1}{2}(\partial_\alpha u_\beta + \partial_\beta u_\alpha)$ with $\alpha, \beta = x$ or y, and $\boldsymbol{n}_{ij} = (0,1)$, $(\frac{\sqrt{3}}{2}, -\frac{1}{2})$, $(-\frac{\sqrt{3}}{2}, -\frac{1}{2})$ are the unit vectors along the carbon-carbon bonds in the unstrained honeycomb lattice. The strain-induced asymmetry in the hoppings between neighboring carbon sites results in the addition of a valley-dependent gauge vector potential

$$e\boldsymbol{\mathcal{A}} = \xi\frac{\hbar\eta_0}{2r}\begin{pmatrix} w_{xx} - w_{yy} \\ -2w_{xy} \end{pmatrix}, \tag{2.3}$$

to the Hamiltonian written for the states near one of the corners of the BZ, where $\xi = \pm1$ for valleys $\boldsymbol{K}$ and $\boldsymbol{K}'$.

Homogeneous strain - For an artificially imposed homogeneous deformation, where the GNR is elongated along the y-axis, the elements of the strain tensor are $w_{xx} = -\sigma w$, $w_{yy} = w$, and $w_{xy} = 0$, where $\sigma = 0.165$ is the Poisson ratio for graphite [11] and w parameterizes tensile strain. In this case, both the scalar and vector potentials V_i and $\boldsymbol{\mathcal{A}}$ are constant. The first one introduces merely a shift of the energy scale and can be ignored. The second shifts the nonequivalent Dirac cones from the $\boldsymbol{K}$ and $\boldsymbol{K}'$ corners of the BZ in opposite directions [40], as shown in Fig. 2.1(b). Infinitely wide samples are robust against such deformations [94] and their spectrum remains gapless for strains below 20%. In contrast, GNRs are markedly different due to quantum confinement effects, which allow for an opening of the gap even for small strains ($w \ll 20\%$) [59, 65, 104]. Figure 2.1(c) shows a comparison between the Fermi surfaces around the top $\boldsymbol{K}$ point in the BZ, for unstrained ($w = 0$, red circles) and homogeneously strained ($w = 0$, 0.015 and

0.024, blue circles) ribbons of width $W \simeq 40$nm at $E_F = 100$meV from the DP. When strain is smoothly increased from $w = 0$ to 0.024, the DP (black dot) crosses several quantized momenta lines (green lines) and the system undergoes multiple semiconducting-metallic-semiconducting phase transitions. Therefore, the size of the gap in the spectrum of armchair GNRs is controllable by the amount of deformation [59, 65] within a range determined by the width of the ribbon.

Inhomogeneous strain[1] - To model a more realistic deformation, we assume that a suspended ribbon is clamped at the leads and stretched along the y-axis. Because of the clamping, the resulting deformation is inhomogeneous. We neglect spontaneous wrinkling of the ribbon [24] [2] and consider this simplified problem within the two-dimensional linear elasticity theory [113]. With the center of coordinates chosen in the center of the ribbon, the displacement is then prescribed by two equations [77],

$$\begin{aligned} 2\partial_{xx}u_x + (1-\sigma)\partial_{yy}u_x + (1+\sigma)\partial_{xy}u_y = 0, \\ 2\partial_{yy}u_y + (1-\sigma)\partial_{xx}u_y + (1+\sigma)\partial_{xy}u_x = 0, \end{aligned} \tag{2.4}$$

accompanied by the clamped boundary condition for the left and right edges and free boundary condition for the top/bottom edge,

$$\begin{cases} u_x(x, \pm L/2) = 0 \\ u_y(x, \pm L/2) = \pm \frac{1}{2} wL \end{cases}, \quad \begin{cases} [\partial_x u_x + \sigma \partial_y u_y]_{x=\pm\frac{W}{2}} = 0 \\ [\partial_x u_y + \partial_y u_x]_{x=\pm\frac{W}{2}} = 0 \end{cases}. \tag{2.5}$$

Despite its simplicity, the problem of finding the displacement field satisfying Eqs. (2.4) and (2.5) does not have an analytic solution and we apply the finite element method [130] with a nine-point element to determine $\boldsymbol{u}(x, y)$. Having obtained the displacement[3], we calculate numerically the vector potential $\boldsymbol{\mathcal{A}}(x, y)$,

[1] The distribution of the pseudomagnetic fields have been obtained by Dr. Marcin Mucha-Kruczyński.

[2] Note that we have neglected the possibility of spontaneous wrinkling [24] since strain limits their formation in suspended samples by increasing the transverse rigidity [21]. We have also applied a finite cutoff to regularize the formally divergent displacements [125] one finds using linear elasticity theory [113] near the corners of the clamped ends of the ribbon.

[3] We have applied a finite cutoff to regularize the formally divergent displacements[125] one finds using linear elasticity theory near the corners of the clamped ends of the ribbon.

as predicted by the continuum model, Eq. (2.3), and the valley-dependent pseudo-magnetic field $\boldsymbol{\mathcal{B}}(x,y) = \mathrm{rot}\boldsymbol{\mathcal{A}}(x,y)$, shown in Fig. 2.1(a) for the $\boldsymbol{K}$ valley. The pseudo-magnetic field is largest [positive (blue) or negative (red)] near the contacts at the right and left ends, and is small in the middle part of the ribbon where strain is approximately homogeneous. Strong pseudo-magnetic fields may lead to the quantization of electronic states into LLs [40, 56, 77] and the appearance of gaps in the electronic spectrum. In order to investigate the effect of such strain-induced modifications of the electronic structure of armchair GNRs on their transport properties, we map the displacement directly onto the crystalline lattice of the ribbon and calculate the positions of the carbon atoms after the deformation. We recalculate the nearest-neighbor couplings according to Eq. (2.2) and use this information as input for the transport calculations. We ignore the on-site scalar potential V_i as it has been shown before that it is screened by electrons in the flake [77].

2.2 Conductance of GNRs

The phase-coherent transport properties of such two-terminal devices are encoded in the scattering matrix[7, 12, 102]

$$S = \begin{pmatrix} r & t' \\ t & r' \end{pmatrix}, \tag{2.6}$$

which we evaluate using the recursive Green's function technique[28, 99] applied to the tight-binding model in Eq. (2.1). Here, t, t' (r, r') are the transmission (reflection) amplitudes of charge carriers incident from the source or the drain leads respectively. Using the Landauer-Büttiker formalism[18] we calculate the device conductance, in the middle part of the GNR,

$$G\left(E_F\right) = \frac{2e^2}{h}\mathrm{Tr}(t^\dagger t), \tag{2.7}$$

as a function of the Fermi level E_F, where $\mathrm{Tr}(t^\dagger t)$ is the transmission coefficient, or

$$G(\mu, T) = \frac{2e^2}{h} \int dE_F \left(-\frac{\partial f_{FD}(E_F - \mu)}{\partial E_F} \right) \mathrm{Tr}(t^\dagger t), \tag{2.8}$$

as a function of chemical potential μ and temperature T. In the latter we have integrated over the electron energy as determined by the Fermi-Dirac distribution f_{FD} with finite temperature.

For a given height ($V = -200$meV) of the gate controlled potential energy step between the doped graphene leads and the suspended part, the resulting device is a p-p'-p ($E_F < -200$meV), n-p-n ($-200 < E_F < 0$meV), or n-n'-n ($E_F > 0$meV) graphene junction. In such systems most of the conductance features are determined by scattering from the strain-modified p-p', n-p, or n-n' interfaces, a behavior which can be revealed by analyzing the spatial distribution of the electronic states. Within the used formalism, the LDOS profiles at fixed energy can be obtained from [38]

$$LDOS = \frac{i}{4\pi} \mathrm{Tr} \left(S^\dagger \frac{\partial S}{\partial V} - \frac{\partial S^\dagger}{\partial V} S \right), \tag{2.9}$$

which gives the response of the scattering amplitudes to a small local perturbation δV added to the Hamiltonian in Eq. (2.1). The scattering matrix is in general a function of the incident energy of the carriers and a functional of the potential V. To linear order in perturbation,δV, the density response of the scattering problem can be expressed through Eq. (2.9).

2.2.1 Transport across homogeneously strained armchair GNRs

By evaluating Eq. (2.8) numerically for a GNR with $W \simeq 40$nm and aspect ratio $L/W = 3$ for various artificially imposed homogeneous strains, we obtain the linear response conductance, as a function of chemical potential and temperature,

shown in the panels of Fig. 2.2. For the unstrained GNR [Fig. 2.2(a)], which is semiconducting with a gap of $\simeq$ 30meV as determined by the momentum quantization, the conductance exhibits two minima at $\mu = -200$meV and 0meV and a local maximum at -100meV. The conductance oscillations away from the two DPs are due to the Fabry-Pérot-like standing wave resonances in the electron transmission across the potential barrier geometry [47, 93, 115]. This can be seen in the LDOS profile shown in the insert, which we calculated using Eq. (2.9) at energy $E_F = -129.2$meV. For homogeneously strained GNRs in Figs. 2.2(b)-(i) the results show that the conductance continues to exhibit the minima at $\mu = -200$meV and 0meV, however, depending on the strength of the deformation, $G(-200\text{meV} < \mu < 0\text{meV})$ can decrease, acquire a resonant structure, or become completely suppressed.

For deformations $w < 0.018$ [Figs. 2.2(b)-(c)] the conductance $G(-200\text{meV} < \mu < 0\text{meV})$ is decreased. The strain-induced shift of the DP, as illustrated by the example in Fig. 2.1(c), determines a misalignment between Fermi surfaces in the unstrained leads and the suspended strained region. Only the quantized momenta that cross the overlapping area of the two Fermi surfaces correspond to propagating modes in the leads that couple to propagating modes in the suspended region and therefore contribute towards transport. With increasing strain, the area of the overlap decreases and the conductance is reduced as an increasing number of conducting channels become blocked.

For strains $0.018 \leq w < 0.024$ [Figs. 2.2(d)-(h)] the conductance exhibits a series of well defined resonances. In this range of strains, the area of the overlap between Fermi surfaces is narrower than the separation between neighboring quantized momenta lines. For a fixed strain w, the width of the overlap remains constant with varying energy, in an n-p-n junction, but the overlap itself is shifted in the momentum plane along the k_x-axis. Therefore, the zero-conductance plateaus appear periodically in the range of energies where there is no quantized momenta line crossing the area of the overlap. In this case, the propagating modes in the central device only couple to evanescent modes in the leads, leading to the formation of

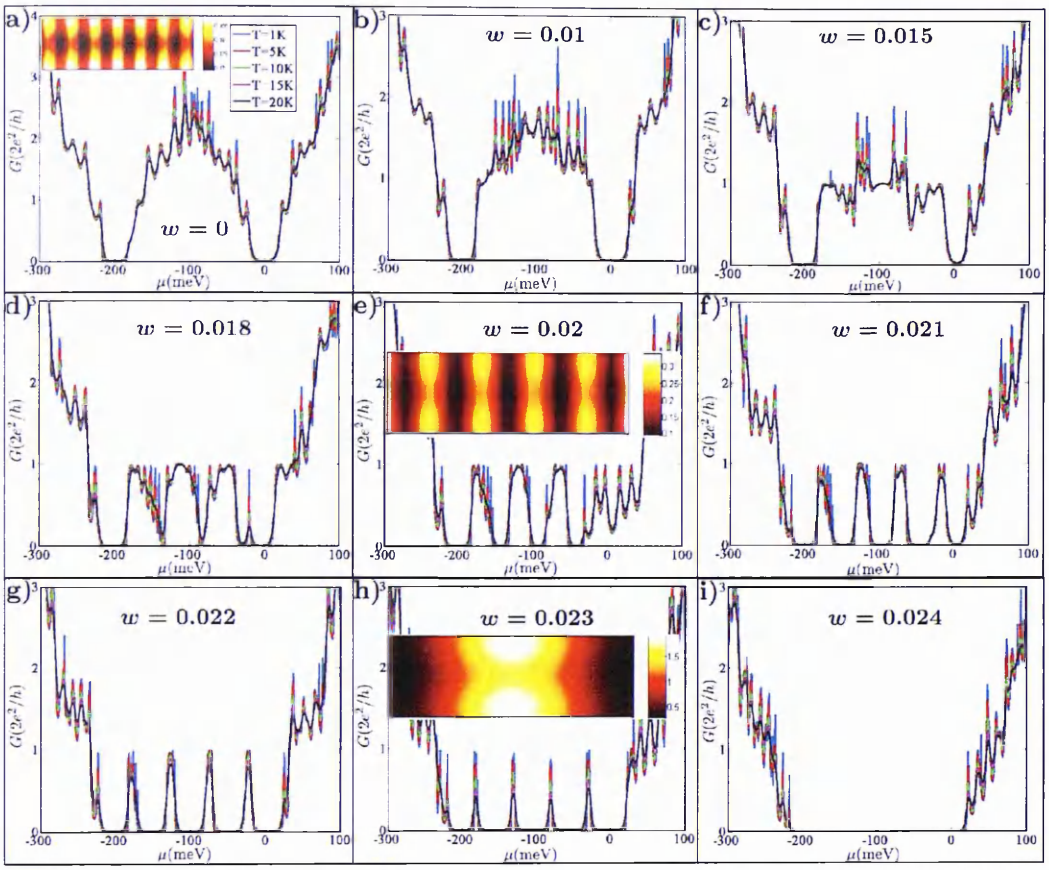

Figure 2.2: Linear response conductance, as a function of chemical potential μ at several fixed temperatures T, of the suspended GNR with $W \simeq 40$nm and aspect ratio $L/W = 3$, for various values of artificially imposed homogeneous strain shown in each panel respectively. Panels a), e) and h) also show the spatial structure of electron wave amplitudes at energy $E_F = -129.2$meV, evaluated using Eq. (2.9).

transport gaps in the system. The finite-conductance resonances are entirely due to Fabry-Pérot-like standing wave patterns, as illustrated by the LDOS profiles in Fig. 2.2(e, h).

For strains $w \geq 0.024$ [Fig. 2.2(i)] the conductance $G(-200\text{meV} < \mu < 0\text{meV})$ is suppressed. Such strong deformations determine a complete misalignment between the Fermi surfaces in the two regions, resulting in a suppression of the conductance in the ballistic regime [93]. This threshold for the insulating behavior is controlled by the parameters used in Fig. 2.2 and can be lowered (raised) by reducing (increasing) the height of the potential step between the central part of the ribbon and the contacts.

The finite-conductance resonances are characteristic for junctions between re-

gions of different polarity (n-p-n junctions) and are absent in junctions between regions of the same polarity (n-n'-n and p-p'-p junctions). This is because for $\mu < -200$meV and $\mu > 0$meV the overlap of the Fermi surfaces increases with increasing energy, and is crossed by an increasing number of quantized momenta lines. Therefore, the conditions for the appearance of the resonances will never be fulfilled. With larger strains ($w > 0.03$) the two Fermi surfaces will start overlapping at energies further from the DPs ($E_F < -200$meV or $E_F > 0$meV), which will determine a widening of the transport gap in Fig. 2.2(i). For example, at $w = 0.05$ the conductance $G \to 0$ in the entire energy range $|E_F| \leq 100$meV around the DP of the suspended region.

Ideal ribbons, with perfectly cut edges are not realistic, as most of such experimentally realized structures present a certain degree of roughness at the edges [41, 58]. Therefore, in the next subsection we discuss the effect of edge disorder on the transport properties of homogeneously strained GNRs.

Influence of edge disorder in GNRs

In this section we establish the robustness of the strain-induced conductance resonances against edge defects, for the GNRs discussed above. We introduce edge disorder in our system by randomly removing a fraction f of either the atoms within a strip of width $2r$, where $r = 1.42\text{Å}$, from the edges, [34, 57, 75, 99] or the dimer lines (pairs of C-C atoms) in the outer-most rows of the edges, [3, 57] in the suspended region. The missing atoms are modeled by setting all the nearest neighbor hopping elements γ_{ij} to zero. Figures 2.3(a)-(c) show the numerically calculated conductance, at fixed temperature $T = 20$K, of a homogeneously strained GNR of width $W \simeq 40$nm and aspect ratio $L/W = 3$ for several strains w and in the presence of various percentages f of 'single-atom' and 'double-atom' edge defects, as shown for each panel respectively.

Our results in Fig. 2.3(a) show that single-atom edges defects induce the smearing or even the suppression of the finite-conductance resonances. As compared to the results for a defect-free system, Fig. 2.2(d)-(h), the conductance is greatly

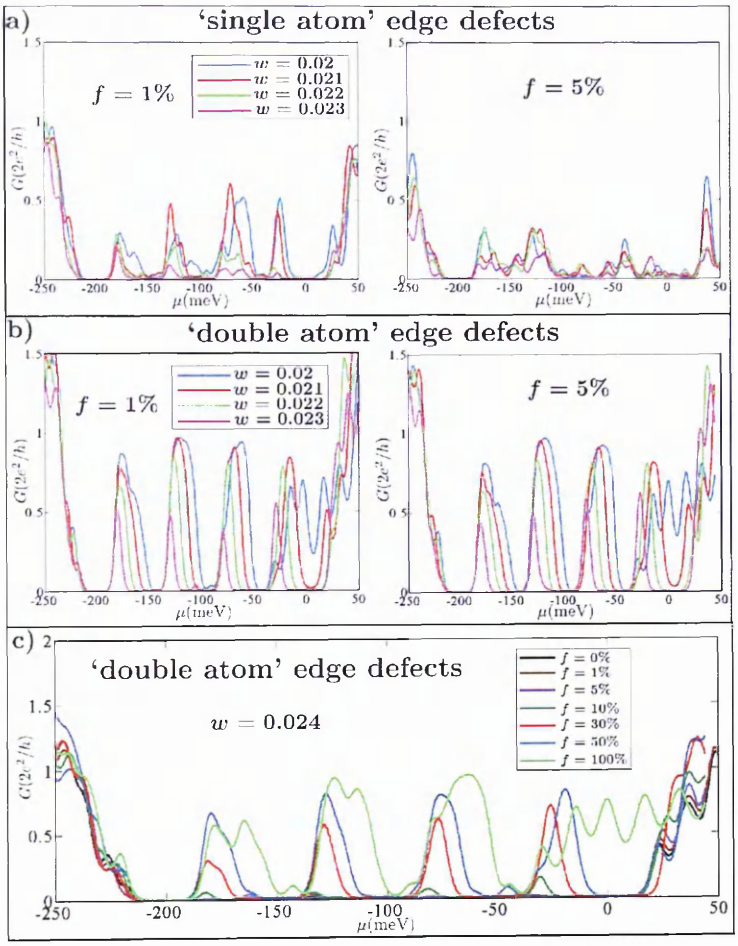

Figure 2.3: Linear response conductance as a function of chemical potential at fixed temperature $T = 20$K, for GNRs with: $f = 1\%$ and 5% a) 'single-atom' and b) 'double-atom' edge defects for $w = 0.02, 0.021, 0.022,$ and 0.023 artificially imposed homogeneous strain. c) with $w = 0.024$ artificially imposed homogeneous strain and various percentages of 'double-atom' edge defects as shown in the insert.

reduced in the presence of $f = 1\%$ edge disorder, and the resonances become barely visible when $f = 5\%$. Previous studies have shown that in the absence of strain, such edge disorders determine drastic changes in the transport properties of armchair GNRs, by inducing large fluctuations in the conductance even for small percentages of defects. By breaking the sublattice symmetry [57] and acting as short-range scatterers [34, 75], such edge defects induce backscattering, Anderson-type localization, and even the formation of conduction gaps. Similarly, our calculations also show that the conductance rapidly degrades with increasing edge disorder, as an increasing number of conductive paths become blocked, and therefore the observed resonances become washed out.

Double-atom edge defects, on the other hand, keep the sublattice symmetry intact and therefore only induce small changes in the conductance [57], as it can be seen in Fig. 2.3(b). As compared to the results for a defect-free ribbon, Fig. 2.2(d)-(h), the conductance for $f = 1\%$ and $f = 5\%$ disorder show remarkably little changes. Even at higher degrees of disorder, the resonances are still visible. The most significant result was obtained for $w = 0.024$ strain, depicted in Fig. 2.3(c) where we show the conductance calculated for various percentages of edge disorder. It can be seen that, in this case, the ballistic properties of the device are restored by such edge disorders. This behavior can be understood by comparing the two disorder extremes: $f = 0\%$ and $f = 100\%$. At $f = 0\%$ (no edge disorder), the central device and leads are perfectly matched, both having a width W and the same transverse momentum quantization. The requirement for conservation of transverse momenta leads to a complete suppression of the conductance, since the Fermi surfaces in the leads and the strained suspended region do not overlap. At $f = 100\%$ edge "disorder" the outermost rows of dimer lines at the top and bottom edges of the suspended region are completely removed. Therefore this region has a smaller width and correspondingly different quantized transverse momenta than the leads. In this case the conservation of momentum requirement is lifted and the mismatch induces a mode mixing mechanism at the interfaces between the three regions of the GNR, leading to the appearance of finite-conductance resonances even if the Fermi surfaces do not overlap. Other degrees of edge disorder will induce a random mixture of local boundary conditions [3] at the edges, and therefore yield intermediate conductance results.

To summarize, in the last two subsections we have established that the ballistic transport of GNRs, in the energy range around the DP of the suspended region at $E_F = 0\text{meV}$, is destroyed by homogeneous strains $w > 0.024$. Furthermore, this trend is not affected by reasonable amounts $f \leq 5\%$ of single-atom or double-atom edge defects which at these concentrations can only induce weak modifications in the conductance profiles.

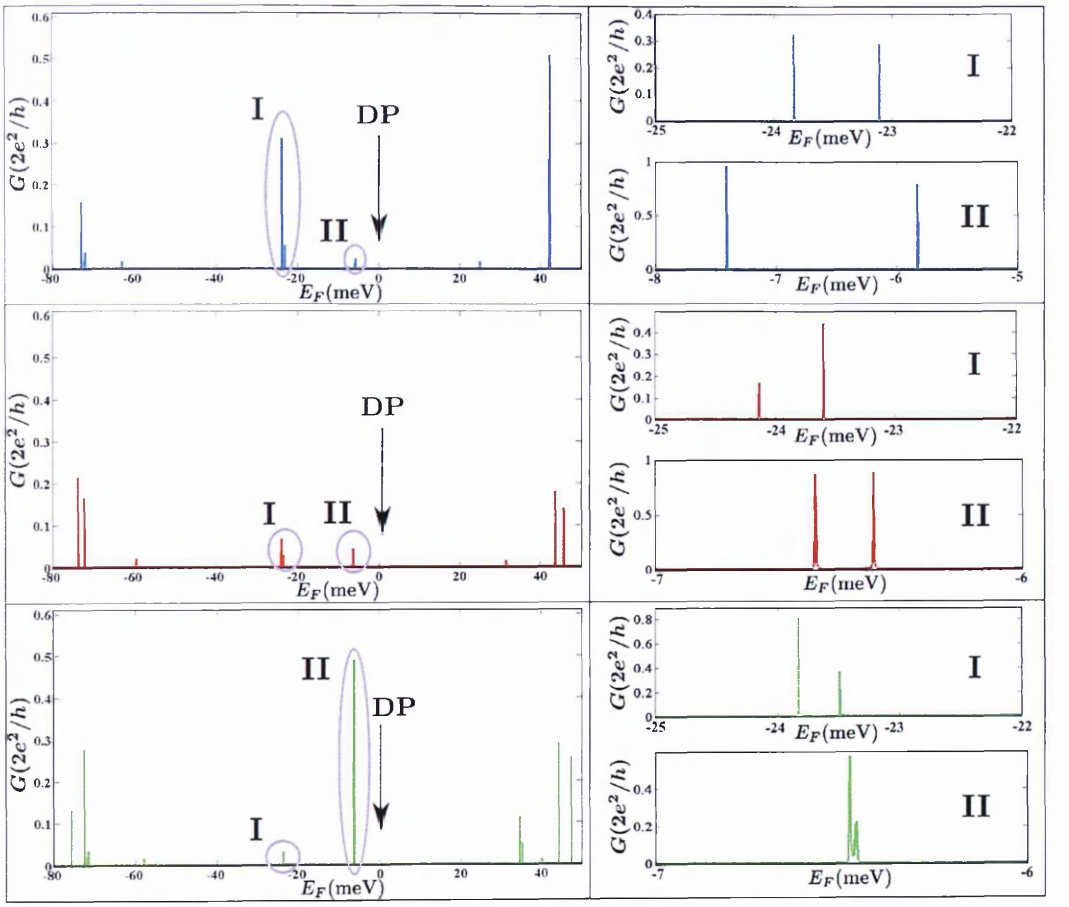

Figure 2.4: Left: Zero-temperature conductance, as a function of Fermi energy, of suspended GNRs with $W \simeq 40$nm and aspect ratios $L/W = 2$, 3, and 4 (blue, red, green), and $w = 0.05$ inhomogeneous strain, which are clamped at the highly-doped contacts. Right: High accuracy conductance results obtained for two groups of peaks identified in the panels on the left.

2.2.2 Transport across inhomogeneously strained armchair GNRs

In contrast to perfect and disordered homogeneously strained GNRs, where $G \to 0$ around the neutrality point of the suspended part, we find that $G(E_F)$ features several peculiar resonances in inhomogeneously strained ribbons, due to pseudo-magnetic fields which develop near the left and right edges. Since previous works have predicted the formation of pseudo magnetic LLs in such systems [40, 56, 77], we aim at finding whether any of the observed new features in the conductance reflect this quantization of the electronic states. We focused our study on the energy range $|E_F| < 100$meV, around the DP of the suspended region, where, if

present, the first few LLs are well resolved. Outside of this energy range, the states are likely to be broadened and smeared [40].

We consider three inhomogeneously strained ribbons, of width $W \simeq 40$nm and aspect ratios $L/W = 2$, 3 and 4 with $w = 0.05$ in their middle parts and pseudo-magnetic field distributions shown in Fig. 2.5(a). Using Eq. (2.7) we calculate their zero-temperature conductance and arrive at the results on the left hand side of Fig. 2.4. In contrast to the results obtained in the previous subsections, where the conductance was completely suppressed for homogeneous strains $w \geq 0.024$, here, we find four groups of sharp and clearly defined resonance conductance peaks for each considered aspect ratio. The two groups positioned far from the DP, at $E_F \simeq -70$meV and $\simeq 40$meV, contain several resonances with their number being proportional to the aspect ratio of the respective ribbons. For the other two groups, positioned in the energy rage $-25\text{meV} < E_F < 0\text{meV}$ just below the DP, the high accuracy conductance results, on the right hand side of Fig. 2.4, reveal that these resonances always occur in pairs of two. Furthermore, the splitting of the two peaks in each group decreases with increasing aspect ratio. To uncover the character of each group of peaks, we analyze the spatial distribution of the corresponding electronic states using Eq. (2.9), and arrive at the LDOS profiles shown in Fig. 2.5(b).

As illustrated in the top two rows, the states away from the DP correspond to Fabry-Pérot-like standing waves. Similarly to the LDOS profiles in Fig. 2.2, such states are confined in the central part of the structure, where the strain distribution is approximately homogeneous, due to multiple electron reflections from the left and right interfaces. Here, the inhomogeneity mixes the transverse quantized states at the n-p and n-n' interfaces, allows for the charge carriers to overcome the misalignment of the Fermi surfaces, described in Sec. 2.1, and therefore leads to the formation of these resonances. For the two groups in the energy range $-25\text{meV} < E_F < 0\text{meV}$, where the resonances occur in almost degenerate pairs, the LDOS profiles shown in the bottom four rows of Fig. 2.5(b) do however point towards a very different behavior. Unlike any of the resonances we found up to

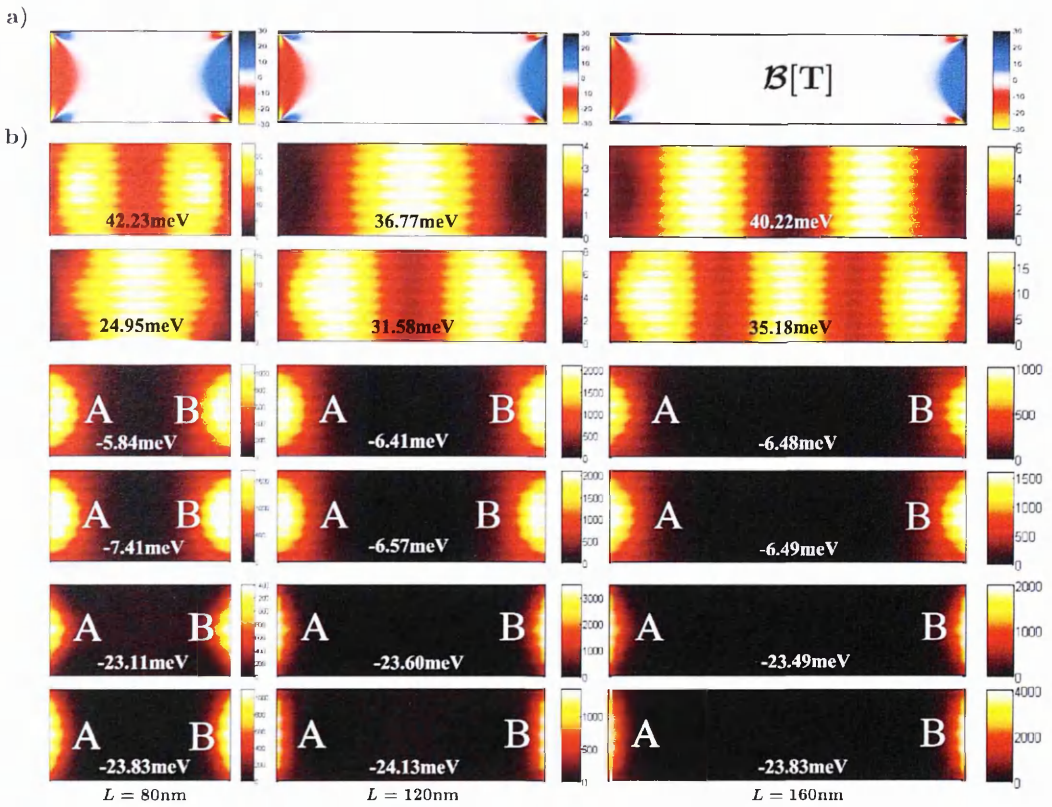

Figure 2.5: We consider transport through suspended GNRs with $W \simeq 40$nm and aspect ratios $L/W = 2, 3$, and 4, and $w = 0.05$ inhomogeneous strain, which are clamped at the highly-doped contacts. Panel (a) shows the distribution of pseudo-magnetic fields $\mathcal{B}(\mathrm{T})$ for electrons in the $\boldsymbol{K}$ valley. Panel (b) shows the spatial structure of electron wave amplitudes corresponding to several resonances identified in Fig. 2.4.

now, the spatial structure for these states clearly resembles the pseudo-magnetic field distributions, which is an indicator for the formation of LLs. We believe that this quadruplet of resonances (two groups each containing two conductance peaks) can be attributed to the $n = 0$ pseudo-magnetic Landau level induced by the inhomogeneity at the interfaces, and attempt to demonstrate this below.

Our main piece of evidence is a unique feature of this LL in graphene, namely that the electron amplitude resides either on the A or B sublattice. This can be seen from

$$v_F \begin{pmatrix} 0 & \hat{\pi}^\dagger \\ \hat{\pi} & 0 \end{pmatrix} \begin{pmatrix} |0\rangle \\ 0 \end{pmatrix} = \begin{pmatrix} 0 \\ 0 \end{pmatrix}, \tag{2.10}$$

where by acting with the low-energy [22] Hamiltonian on the $n = 0$ state with

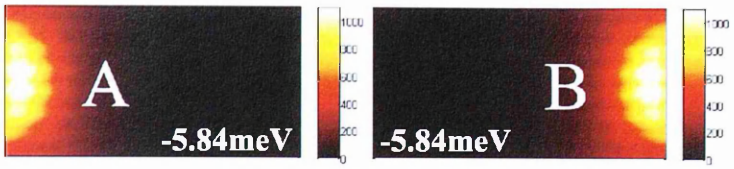

Figure 2.6: Sublattice-resolved electron amplitude for one of the resonances in Fig. 2.4 ($L/W = 2$, $E = -5.84$meV), obtained by placing the probing perturbation on the A (left panel) or B (right panel) sites.

non-zero amplitude $|0\rangle$ on the A sublattice, we obtain the $E_F = 0$ eigenvalue. This is not the case for the state with finite amplitude on the B sublattice. Here v_F is the Fermi velocity, $\hat{\boldsymbol{\pi}} = \hat{\boldsymbol{p}} + \frac{e}{c}\boldsymbol{\mathcal{A}}$ where $\hat{\boldsymbol{p}} = p_x + ip_y$ parameterizes the in-plane momentum relative to the $\boldsymbol{K}$ or $\boldsymbol{K'}$ point, $\boldsymbol{\mathcal{A}}$ is the vector potential in Eq. (2.3), and $\hat{\boldsymbol{\pi}}\,|0\rangle = 0$. The selected sublattice depends on the sign of $\mathcal{B}$ but is independent of the valley [40]. In contrast, higher order LLs and Fabry-Pérot-like resonances occupy both sublattices equally [129]. By placing the probing perturbation δV in Eq. (2.9) on either the A or on the B sites, we find, as illustrated for one example in Fig. 2.6, that the low-energy resonances are localized and have high amplitude only on the A-sites near the left interface (where $\mathcal{B} < 0$), and only on the B-sites near the right interface (where $\mathcal{B} > 0$). This is in agreement with the unique feature of the $n = 0$ LL described above.

Another fact that supports our interpretation of the origin of these states, is that we find four such low-energy resonances, with the separation between each pair inversely proportional to the aspect ratio of the ribbon. The $y \to -y$ reflection symmetry of the system maps the $\boldsymbol{K}$ and $\boldsymbol{K'}$ valleys onto each other, which results in the formation of a symmetric and an anti-symmetric superposition of the two valley manifestations of the $n = 0$ LL. This leads to a splitting of the $n = 0$ LL into two branches, corresponding to each of the two groups of resonances. The low-energy branch, located at $E_F \approx -24$meV, is valley-symmetric and displays a maximum on the symmetry axis, and the high-energy branch at $E_F \approx -7$meV is valley-antisymmetric and displays a nodal line on the symmetry axis. The tunnel coupling of the states Ψ^0_L and Ψ^0_R near the left and right ends of the ribbon, leads to the mixing and splitting of these pairs of states into even and odd linear

combinations $\frac{1}{\sqrt{2}}(\Psi_L^0 \pm \Psi_R^0)$, which results in the formation of two weakly split resonances. This is provided by the evanescent tails of the electronic wave functions in the middle part, where $\mathcal{B}$ is small. Naturally, since the overlap of the evanescent tails of Ψ_L^0 and Ψ_R^0 decreases with increasing aspect ratio, the splitting in each of these pairs is smaller in a longer ribbon, thus explaining the trend we highlighted in our discussion of the high accuracy conductance result on the right hand side of Fig. 2.4.

2.3 Conclusion

In conclusion, we performed a systematic study of the transport characteristics of homogeneously and inhomogeneously strained suspended armchair graphene nanoribbons. Our analysis revealed that the strain-induced shift of the Dirac point in the momentum plane, due to artificially imposed homogeneous deformations, coupled to the size confinement effects, leading to significant modifications in the transport properties of such systems. Namely, depending on the strength of the deformation, the conductance can decrease, acquire a resonant structure, or be completely suppressed. We have also established that the resonant structure is sensitive to 'single atom' edge defects and is destroyed by this type of edge disorder. However, it is robust against 'double atom' edge defects which have the ability to restore the ballistic transport in the case of a completely suppressed conductance. For the case of inhomogeneous deformations, we have found that the inhomogeneity developed near the contacts, aids the resonant transmission of charge carriers, either through a mode mixing mechanism, or through the sublattice-polarized $n = 0$ pseudo-magnetic Landau level. The former leads to the formation of Fabry-Pérot-like standing waves, in the central homogeneously strained part of the ribbon, which result in the formation of conductance peaks far from the Dirac point. For the latter case, the states form near the contact regions and give rise to two groups of resonances near the Dirac point, each containing a pair of conductance peaks.

Chapter 3

Conductance anomaly near the Lifshitz transition in strained bilayer graphene

3.1 Introduction

Bilayer graphene (BLG) [74, 85], a crystal consisting of two graphene monolayers arranged according to Bernal stacking [8], is a material with versatile properties. In contrast to monolayer graphene, where the linear dispersion (Dirac cones) near each corner of the Brillouin zone ($\mathbf{K}$ and $\mathbf{K}'$ points) is very difficult to alter, the low-energy band structure of BLG can be qualitatively modified by relatively weak external perturbations. For example, a transverse electric field opens a mini-gap in the BLG spectrum [20, 71, 74, 86, 87, 128]. Also, it has been shown that a relatively small uniaxial strain (of only a few percent) leads to a change in the topology of the low-energy dispersion, which then exhibits two Dirac mini-cones near each corner of the Brillouin zone (see Fig. 3.1) [55, 67, 76, 109]. Both in the conduction and valence bands, these cones are connected by a saddle point at which the Fermi lines reconnect, a configuration which is known as a Lifshitz transition (LiTr) [1, 60]. (In contrast, in a monolayer, homogeneous strain only results in a small shift of the Dirac cones away from the corners of the Brillouin

zone, without any qualitative change of the linear dispersion or the chiral properties of the electrons [23]).

In this Chapter, we study the transport characteristics of an ideally clean homogeneously strained BLG crystal, aiming to find features in the temperature and chemical potential dependence of its two-terminal conductance that would reflect the presence of the saddle point in the dispersion relation. We consider a short and infinitely wide strained BLG strip (the only geometry where strain in a two-terminal device would be homogeneous [1]), adjacent to BLG regions suspended over metallic contacts. The information encoded in the two-terminal conductance of such a device of finite length is complementary to what is manifested by the sheet conductivity of an infinite flake discussed in Ref. [27, 29]. Since contacts with metals heavily dope graphene, we model the BLG terminals with a high (*e.g.*, n-type) density of carriers, whereas the strip in the middle is considered to be at a low density of carriers (either of n- or p-type, which can be controlled by an external gate). We choose the amount of strain in the structure such that it induces a LiTr at the energy of about ± 5 meV, measured from the charge neutrality point. According to Ref. [76], such an effect on the bands can be generated by about $\sim 1\%$ of uniaxial strain. Note that in suspended graphene structures [35, 37, 68, 69, 116, 124] strain of such size may be inflicted involuntarily, either by processing and annealing of the flake, or by displacements of contacts due to the different contractions upon cooling of the substrate and of the supporting metallic electrodes.

Our findings show that the dependence of the conductance $G(\mu, T)$ on the chemical potential and temperature does indeed reflect the spectral reconstruction by strain, in the form of a conductance anomaly: a non-monotonic dependence of $G(\mu, T)$ on both parameters, μ and T. This behavior is characteristic for the regime where the chemical potential is close to the saddle point in the electron/hole spectrum on one of the sides of an n-p junction, or in the middle of an n-p-n device. The conductance anomaly is sensitive to the crystallographic orientation

[1] M. Mucha-Kruczyński and V.I. Fal'ko, (unpublished).

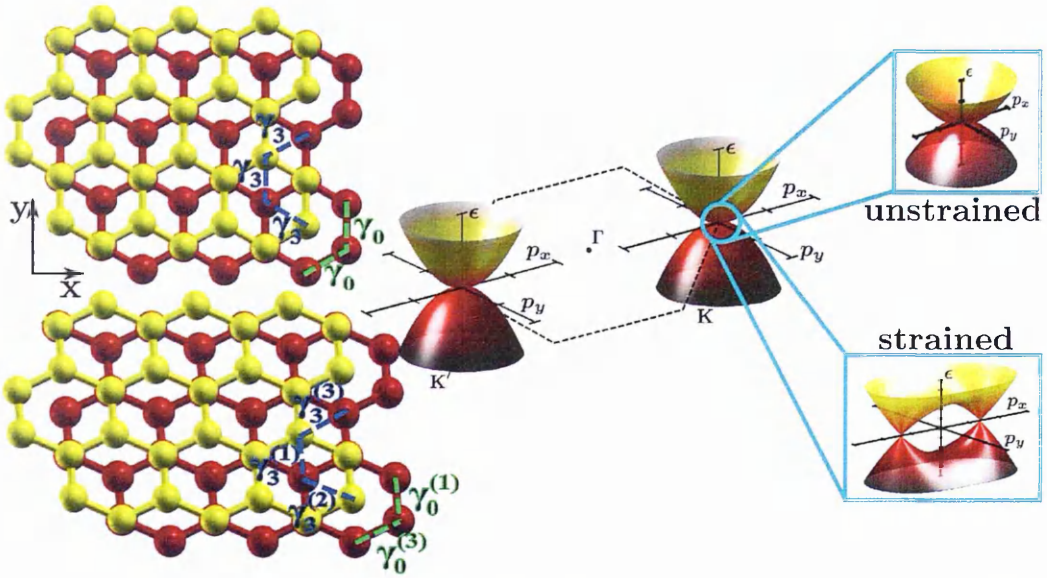

Figure 3.1: Left: Top view of an unperturbed (top panel) and a strained (bottom panel) bilayer graphene (BLG) crystal. The top and bottom layers are shown in yellow and red, respectively. Strain modifies the intra-layer nearest neighbors coupling γ_0, as well as the inter-layer coupling γ_3 between atoms at the center of the other layer's hexagons. Right: Electronic band structure in the vicinity of the Brillouin zone corners **K** and **K**′, with focus on the low-energy dispersion near the **K** point for unperturbed and strained BLG.

of the sample geometry, which determines the principal axis of the strain tensor. Similar results in strained bilayer graphene have been obtained by Ref. [90]. Our above outlined results are described in detail in Sections 3.3 and 3.4, with their graphic representation shown in Figs. 3.3 and 3.4. The calculations are based on the Landauer-Büttiker approach [18], with transmission probabilities obtained in the transfer matrix method [5, 79, 101, 103]. Section 3.2 introduces the model for a strained bilayer graphene device and identifies the propagating and evanescent modes required for these calculations.

3.2 Electron dispersion and propagating modes in strained BLG

In this section, we identify the energy dispersion and transport modes in homogeneously strained BLG regions. These results are used in the subsequent sections to study the transport in devices made out of several such regions (n-p and n-n'

junctions in Sec. 3.3, n-p-n and n-n'-n junctions in Sec. 3.4).

The lattice structure and parametrization of the minimal relevant tight-binding model for electrons in strained BLG [74, 76] are illustrated in the left panel of Fig. 3.1. The stacked layers have every A site within each layer surrounded by three B sites and *vice versa*, with intralayer coupling $\gamma_0 \sim 3$eV; A_2 sites are on top of B_1 sites, with interlayer coupling $\gamma_1 \sim 0.4$eV, while A_1/B_2 sites sit over/under the hexagons in the other layer and are coupled by the 'skew' hopping energy $\gamma_3 \sim 0.3$eV. The low-energy electronic states reside on the sites A_1 and B_2, while the sites A_2 and B_1 support states in split bands which do not contribute to low-energy transport. For unstrained BLG, the low-energy states near each corner of the Brillouin zone form two approximately parabolic bands, a valence band and a conductance band, which touch each other at the **K** or **K'** point, as shown in the top right panel of Fig. 3.1.

Uniaxial strain changes the intralayer and interlayer hopping integrals γ_0 and γ_3 by making them direction dependent, as shown in the bottom left panel of Fig. 3.1. Neglecting trigonal warping for large enough strain, the corresponding low-energy dispersion near a given corner of the Brillouin zone is described by the effective Hamiltonian[67, 76, 109]

$$\mathcal{H} = \begin{pmatrix} V(x) & -\frac{1}{2m}\left(\pi^\dagger\right)^2 + we^{-2i\phi} \\ -\frac{1}{2m}\left(\pi\right)^2 + we^{2i\phi} & V(x) \end{pmatrix}. \tag{3.1}$$

Here $m \approx 0.035m_e$ is the effective mass, $\pi = p_x + ip_y$ parametrizes the in-plane momentum relative to the **K** or **K'** point, and $we^{-2i\phi}$ accounts for the change of the couplings due to the strain, where ϕ is the angle between the principal axis of the strain tensor and the crystallographic direction of the crystal. Using the tight binding model for BLG, one finds [67, 76, 109] that $w = (3/4)(\eta_3 - \eta_0)\gamma_3(\delta - \delta')$, with $\eta_{0,3} = d\ln\gamma_{0,3}/d\ln r_{AB}$ where r_{AB} is the distance between carbon sites, while δ and δ' are the two principal values of the strain tensor.

Near each corner of the Brillouin zone, the low-energy dispersion relation obtained from Eq. (3.1) exhibits two Dirac mini-cones, which are separated from the

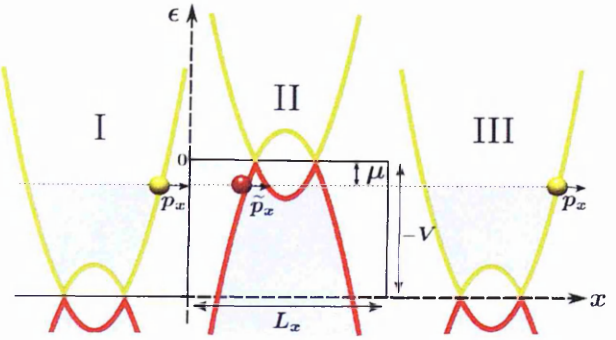

Figure 3.2: Schematic representation of a suspended BLG device with strain axis oriented along the x-direction (as defined in Fig. 3.1). The sketch illustrates the example of an n-p-n configuration of such a device ($\mu < 0$). In the highly doped contact regions the Fermi level (dotted line) lies high up in the conduction band (yellow), where the dispersion is parabolic. In the central region the Fermi level lies in the valence band (red), and is close to the charge neutrality point, where the dispersion is modified due to the two Dirac mini-cones and the saddle point associated with the Lifshitz transition. Shading indicates occupied states.

parabolic spectrum at high energies ($w \ll |\epsilon| < \gamma_1/2$) by a saddle point at $\epsilon = \pm w$ (see bottom right panel of Fig. 3.1). For energies $|\epsilon| < w$ between the saddle points, each mini-cone results in a disconnected, approximately circular Fermi line. At the saddle point, the lines connect pairwise in a LiTr, and beyond the LiTr there is only a single Fermi line encircling the **K** or **K**′ point. Relative to these corner points, the strain-induced Dirac points are positioned in the momentum plane at

$$\mathbf{p}_0 = p_0 \left(\cos\phi, \sin\phi\right), \quad p_0 = \pm\sqrt{2mw}. \tag{3.2}$$

After expanding $\mathcal{H}$ in Eq. (3.1) in momentum $\mathbf{p} - \mathbf{p}_0$ around these Dirac points (and keeping only linear terms), we find that each one is characterized by a Dirac velocity $v^* = p_0/(2m)$.

In the following, we study how this strain-induced change in the topology of the electronic bands affects the transport properties of a device made of a strained flake of BLG, where a short and wide strip of width $L_y \gg L_x$ sits between two highly doped BLG regions suspended over two metallic contacts. The band alignment in such a device is sketched in Fig. 3.2. Metallic electrodes heavily dope BLG in the vicinity of the contacts, thus determining two leads (regions I and III) with a high carrier density. An external electrostatic gate controls the doping, and, thus, the

chemical potential μ of the electrons in the middle part of the flake (region II), which we consider to be close to the neutrality point. In our model this doping profile is taken into account by potential steps at the sample edges

$$V(x) = \begin{cases} 0 & \text{if } 0 \le x \le L_x, \\ -V_0 & \text{otherwise,} \end{cases} \qquad \frac{\gamma_1}{2} \gg V_0 \gg w,\ \mu.$$

In the remainder of this section, we identify the transport modes in the various regions of the system.

The stated conditions make the energy dispersion in the leads approximately parabolic, $\epsilon \approx p^2/(2m) - V_0$, and the plane-wave states the same as chiral states in unstrained BLG[74], with a very little effect of the strain. For a given incidence angle θ of an incoming electron in the contact, we parametrize its transverse momentum along the step as $p_y = \sqrt{2m|V_0 + \epsilon|}\sin(\theta)$, and use the longitudinal component

$$p_x^{ln} = l\sqrt{2nm|V_0 + \epsilon| - p_y^2}, \quad l = \pm, \tag{3.3}$$

to characterize propagating modes ($n = +$, real momentum) and evanescent modes ($n = -$, complex momentum). For propagating modes in the conduction band of the leads, as considered here, the group velocity is directed parallel to the momentum, and thus the index l coincides with the propagation direction along the x axis, *i.e.*, $l = +$ denotes a state propagating to the right.

We now turn to the modes in the weakly doped region II. The left panels in Fig. 3.3 show the isoenergetic lines for electrons in the valence band at low energies for unperturbed [Fig. 3.3(a)] as well as strained BLG [Figs. 3.3(b)-3.3(d)], with $w = 5$ meV and for several orientations of the strain principal axis. States corresponding to plane waves moving to the right are indicated by red and green, and to the left by purple and blue. (Note that for some of these modes, the group velocity is directed opposite to their momentum.) These isoenergetic lines reflect that the low-energy dispersion relation in strained graphene is determined by the

modified condition

$$c^2 = \frac{1}{4m^2}\left(\widetilde{p}_x^2 + p_y^2\right)^2 - \frac{1}{m}w\left(\widetilde{p}_x^2 - p_y^2\right)\cos(2\phi) - \frac{1}{m}2w\widetilde{p}_x p_y \sin(2\phi) + w^2 \tag{3.4}$$

(here and in the following, an overscript tilde denotes quantities specific for region II; energy ϵ and transverse momentum p_y are conserved for elastic scattering at a straight interface). For given values of energy and transverse momentum, this equation may have four, two, or no real solutions $\widetilde{p}_x$, where the latter situation arises at any given fixed energy beyond a critical value $|p_y| = p_{y,c}$, which depends on the orientation of the applied strain. We denote the corresponding propagation direction in region I by θ_c, $p_{y,c} = \sqrt{2m|V_0 + \epsilon|}\sin(\theta_c)$, which signifies the critical angle beyond which electrons from the lead only couple into evanescent modes, which do not contribute toward transport. As such, restricting the analysis to the range of angles $(-\theta_c, \theta_c)$ is enough to capture all the essential transport features. Below the critical value and for large values of $|\epsilon|$, there are always two real and two complex solutions, while for small $|\epsilon|$, there are two or four real solutions, which depend on the propagation direction and on the orientation of the applied strain, as we now discuss in detail.

For the unstrained case [neglecting w in Eq. (3.4)], the parameters in region II are given [in analogy to Eq. (3.3)] by

$$\widetilde{p}_x^{ln} = l\ \mathrm{sign}(\epsilon)\sqrt{2nm|\epsilon| - p_y^2}. \tag{3.5}$$

Here, $\widetilde{p}_x^{++}$ ($\widetilde{p}_x^{-+}$) is real and corresponds to right-moving (left-moving) plane waves, while $\widetilde{p}_x^{--}$ ($\widetilde{p}_x^{+-}$) corresponds to evanescent waves decaying to the right (left). [The factor $\mathrm{sign}(\epsilon)$ accounts for the fact that in the valence band, the group velocity is directed opposite to the momentum.]

For strained BLG with strain orientation $\phi = 0$, we find from Eq. (3.4) that

$$\widetilde{p}_x^{ln} = l\ \mathrm{sign}(\epsilon)\sqrt{n\sqrt{4m^2\epsilon^2 - 8mwp_y^2} - p_y^2 + 2mw}, \tag{3.6}$$

where $n, l = \pm$. The left panel of Fig. 3.3(b) shows examples of several isoenergetic lines, with strain-induced Dirac points on the axis p_x in the momentum space. By inspecting Eq. (3.6), one notices that for $|\epsilon| < w$ and $p_y \leq \sqrt{m\epsilon^2/(2w)}$ [angles where $\sin(\theta) \leq \sqrt{\epsilon^2/(4w|V_0+\epsilon|)}$], all four momenta are real [$\widetilde{p}_x^{++}$ (red), $\widetilde{p}_x^{--}$ (green), $\widetilde{p}_x^{+-}$ (purple), $\widetilde{p}_x^{-+}$ (blue)] and the Fermi line is split into two pockets. When ϵ is slightly below (above) the LiTr in the valence (conduction) band, $|\epsilon| > w$, the Fermi line is continuous but deformed. For small values of $|p_y|$, Eq. (3.4) then gives two real solutions ($\widetilde{p}_x^{++}$, $\widetilde{p}_x^{-+}$) and two imaginary solutions ($\widetilde{p}_x^{--}$, $\widetilde{p}_x^{+-}$), while for larger values of $|p_y|$ (just below the critical value $p_{y,c}$) there are four real solutions.

Figure 3.3(c) illustrates the propagating modes for strain with orientation $\phi = \pi/4$, where the momenta were found numerically from Eq. (3.4). The four colors distinguish right-moving plane waves ($\widetilde{p}_x^{++}$ red, $\widetilde{p}_x^{--}$ green) and left-moving plane waves ($\widetilde{p}_x^{+-}$ purple, $\widetilde{p}_x^{-+}$ blue). We now find at most two real solutions for fixed energy and transverse momentum. Above the LiTr in the valence band, there is a range of transverse momenta around $p_y = 0$ (normal incidence from the leads) in which there are no propagating modes in region II.

For the strain axis oriented at $\phi = \pi/2$ [Fig. 3.3(d)], the four solutions of Eq. (3.4) are

$$\widetilde{p}_x^{ln} = l\ \mathrm{sign}(\epsilon)\sqrt{n\sqrt{4m^2\epsilon^2 + 8mwp_y^2} - p_y^2 - 2mw}, \tag{3.7}$$

where, as before, $n = \pm$ and $l = \pm$. By inspecting Eq. (3.7), we find that for all energies and angles below θ_c, only the momenta $\widetilde{p}_x^{l+}$ are real. In Fig. 3.3(d), the corresponding propagating waves are marked red ($\widetilde{p}_x^{++}$, right-moving) and blue ($\widetilde{p}_x^{-+}$, left-moving). Above the LiTr in the valence band, there is again a range of transverse momenta around $p_y = 0$ in which no propagating modes exist in region II.

3.3 Transport across n-p and n-n' junctions

In this section, we study how the presence of strain affects the electron transmission across a single potential step, from a heavily doped region I to the low-density region II. Depending on the sign of the doping, this can be an n-p ($\mu < 0$) or n-n' ($\mu > 0$) junction. In the Landauer-Büttiker approach [5, 18, 79, 101, 103], the conductance G of such a junction is determined by the energy and angular dependence of the transmission probability $\mathcal{T}(\epsilon, \theta)$ of an electron in the conduction band incident from the left to emerge in the valence (or conduction) band at the right of the interface.

3.3.1 Calculation of transmission probability

To calculate the transmission probability $\mathcal{T}(\epsilon, \theta)$, we employ the transfer matrix method [79]. Using separation of variables (allowed for a straight interface), the spinor eigenstates of Eq. (3.1) can be written as $\Phi_{\mathrm{I,II}}(x, y) = \Psi_{\mathrm{I,II}}(x)\, e^{ip_y y}$, where

$$\Psi_{\mathrm{I}}(x) = \sum_{l,n} \frac{a_{ln}}{\sqrt{v_{ln}}} \begin{pmatrix} 1 \\ \alpha_{ln} \end{pmatrix} e^{ip_x^{ln} x}, \tag{3.8}$$

$$\Psi_{\mathrm{II}}(x) = \sum_{l,n} \frac{b_{ln}}{\sqrt{\tilde{v}_{ln}}} \begin{pmatrix} 1 \\ \beta_{ln} \end{pmatrix} e^{i\tilde{p}_x^{ln} x},$$

$$\alpha_{ln} = \frac{-\frac{1}{2m}\left(p_x^{ln} + ip_y\right)^2}{V_0 + \epsilon},$$

$$\beta_{ln} = \frac{-\frac{1}{2m}\left(\tilde{p}_x^{ln} + ip_y\right)^2 + we^{2i\phi}}{\epsilon}.$$

Here, as before, indices I and II label regions to the left and right of the potential step, $l, n = \pm$ discriminate the branches of longitudinal momentum, a_{ln}, b_{ln} are the wave amplitudes, and $v_{ln} = \left|\partial\epsilon/\partial p_x^{ln}\right|$, $\tilde{v}_{ln} = \left|\partial\epsilon/\partial \tilde{p}_x^{ln}\right|$ are the longitudinal components of the group velocity. [Note that in the conduction band ($\epsilon > 0$) and in the valence band ($\epsilon < 0$), the group velocities for fixed electron momentum are oppositely directed.]

The transfer matrix M_1 relates the amplitudes a_{ln} and b_{ln} on the two sides of

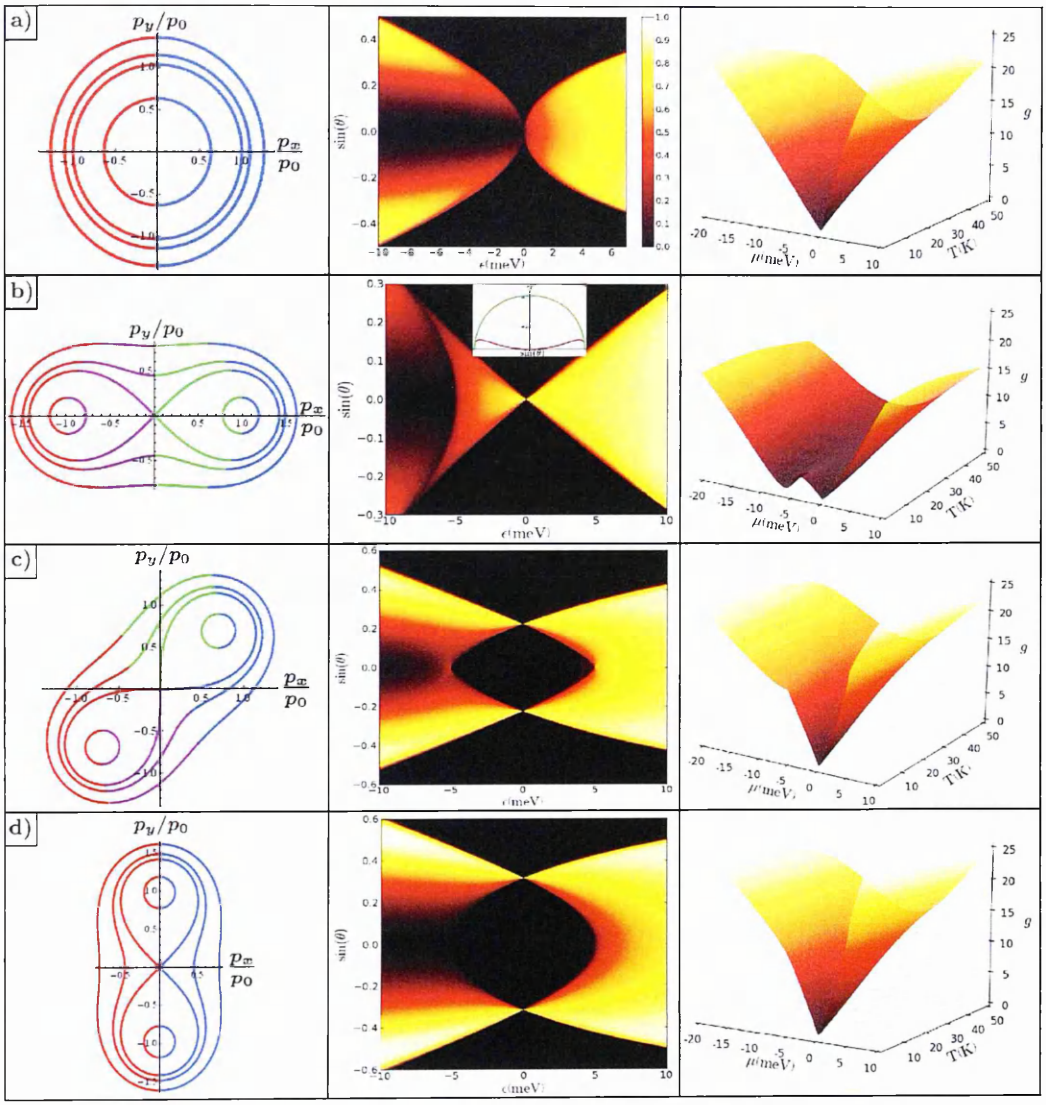

Figure 3.3: Left: isoenergetic lines at $\epsilon = -2$, -5, -6, and -8 meV for strained bilayer graphene, with $w = 5$ meV. Center: transmission probability $\mathcal{T}(\epsilon, \theta)$ across a single potential step (n-p or n-n′ junction), from a highly doped region to a barely doped region, as a function of energy and incidence angle of incoming electrons. Right: linear response conductance of the junction as a function of chemical potential μ and temperature T. Results are shown for unstrained bilayer graphene (a), as well as uniaxially strained bilayer graphene for various orientations of the strain axis with respect to the crystallographic axis x in Fig. 3.1: $\phi = 0$ (b), $\phi = \pi/4$ (c) and $\phi = \pi/2$ (d).

the interface according to

$$\begin{pmatrix} b_{++} \\ b_{-+} \\ b_{--} \\ b_{+-} \end{pmatrix} = M_1 \begin{pmatrix} a_{++} \\ a_{-+} \\ a_{--} \\ a_{+-} \end{pmatrix}. \tag{3.9}$$

To build this matrix, we employ the continuity of the electron wave function $\Psi_{\mathrm{I}}(0) = \Psi_{\mathrm{II}}(0)$ and its derivative $\Psi'_{\mathrm{I}}(0) = \Psi'_{\mathrm{II}}(0)$ at the potential step. In this way, we find that the transfer matrix takes the form

$$M_1 = B^{-1}A, \tag{3.10}$$

$$A = \begin{pmatrix} 1 & 1 & 1 & 1 \\ \alpha_{++} & \alpha_{-+} & \alpha_{--} & \alpha_{+-} \\ p_x^{++} & p_x^{-+} & p_x^{--} & p_x^{+-} \\ \alpha_{++}p_x^{++} & \alpha_{-+}p_x^{-+} & \alpha_{--}p_x^{--} & \alpha_{+-}p_x^{+-} \end{pmatrix} \times \begin{pmatrix} \frac{1}{\sqrt{v_{++}}} & 0 & 0 & 0 \\ 0 & \frac{1}{\sqrt{v_{-+}}} & 0 & 0 \\ 0 & 0 & \frac{1}{\sqrt{v_{--}}} & 0 \\ 0 & 0 & 0 & \frac{1}{\sqrt{v_{+-}}} \end{pmatrix},$$

$$B = \begin{pmatrix} 1 & 1 & 1 & 1 \\ \beta_{++} & \beta_{-+} & \beta_{--} & \beta_{+-} \\ \tilde{p}_x^{++} & \tilde{p}_x^{-+} & \tilde{p}_x^{--} & \tilde{p}_x^{+-} \\ \beta_{++}\tilde{p}_x^{++} & \beta_{-+}\tilde{p}_x^{-+} & \beta_{--}\tilde{p}_x^{--} & \beta_{+-}\tilde{p}_x^{+-} \end{pmatrix} \times \begin{pmatrix} \frac{1}{\sqrt{\tilde{v}_{++}}} & 0 & 0 & 0 \\ 0 & \frac{1}{\sqrt{\tilde{v}_{-+}}} & 0 & 0 \\ 0 & 0 & \frac{1}{\sqrt{\tilde{v}_{--}}} & 0 \\ 0 & 0 & 0 & \frac{1}{\sqrt{\tilde{v}_{+-}}} \end{pmatrix}.$$

In what follows, we characterize waves by their corresponding momentum and

amplitude. In the contact, we assume that there are right-moving propagating waves (p_x^{++}, $a_{++} = 1$) which can be transmitted into region II or reflected by the potential step V_0 back into region I. Reflected waves become left-moving propagating waves (p_x^{-+}, $a_{-+} \neq 0$) and evanescent waves decaying to the left (p_x^{--}, $a_{--} \neq 0$). From this, Eq. (3.9) becomes

$$\begin{pmatrix} b_{++} \\ b_{-+} \\ b_{--} \\ b_{+-} \end{pmatrix} = M_1 \begin{pmatrix} 1 \\ a_{-+} \\ a_{--} \\ 0 \end{pmatrix}, \tag{3.11}$$

and the transmission coefficient can be found using

$$\mathcal{T} = 1 - |a_{-+}|^2. \tag{3.12}$$

This definition is the most convenient for the problem studied here since there is only one left-propagating mode in region I, whereas there are parametric regimes in which two different right-propagating waves exist in region II. In the following, we discuss how this scheme is applied in the four characteristic cases illustrated in Fig. 3.3: (a) unstrained BLG, and (b)-(d) BLG with various angles between the principal axis of uniaxial strain and the crystallographic direction x in Fig. 3.1.

For the unstrained case, using the plane-wave parameters determined in Eq. (3.5), Eq. (3.11) becomes

$$\begin{pmatrix} b_{++} \\ 0 \\ 0 \\ b_{+-} \end{pmatrix} = M_1 \begin{pmatrix} 1 \\ a_{-+} \\ a_{--} \\ 0 \end{pmatrix}. \tag{3.13}$$

Solving for the wave amplitude a_{-+} numerically and then using Eq. (3.12), we obtain the transmission probability shown in the middle panel of Fig. 3.3(a). This reproduces the $\epsilon \to -\epsilon$ asymmetry for transmission of normally incident electrons ($\theta = 0$), with vanishing $\mathcal{T}(\epsilon, 0) = 0$ for $\epsilon < 0$ but finite $\mathcal{T}(\epsilon, 0)$ for $\epsilon > 0$, found in

earlier studies of BLG junctions and the Klein paradox [47, 96, 115] (as opposed to the perfect transmission for $\theta = 0$ in monolayer graphene junctions [47, 115]). This asymmetry can be attributed to the different chirality of charge carriers in the conduction and valence bands.

For the strain axis oriented at $\phi = 0$, using the plane-wave parameters determined in Eq. (3.6) and solving for the amplitude a_{-+} in the set of linear equations in Eq. (3.11), we numerically obtain the transmission result plotted in the middle panel of Fig. 3.3(b). Our result shows $\mathcal{T}(\epsilon, \theta = 0) \neq 0$ at any $|\epsilon| < w$, as opposed to the unstrained case in Fig. 3.3(a). The difference between the transmission at $\theta = 0$ for unstrained and strained BLG can be explained as follows. Expanding the Hamiltonian (3.1) in the momentum space around the Dirac points $\pm\mathbf{p}_0$ of the strain-induced mini-cones [Eq. (3.2)], and keeping only linear terms, we find two Hamiltonians valid at $|\epsilon| \ll w$:

$$\mathcal{H}_{\pm} \approx \pm v^* \begin{pmatrix} 0 & (e^{i\phi}\overline{\pi})^\dagger \\ e^{i\phi}\overline{\pi} & 0 \end{pmatrix}, \quad \overline{\pi} = 2\left(\delta p_x + i\delta p_y\right), \tag{3.14}$$

where $\delta\mathbf{p}$ is a small deviation of the electron momentum from $\pm\mathbf{p}_0$, $v^* = p_0/(2m)$ is the effective Dirac velocity, and $e^{i\phi}$ is a phase factor which determines the position of the Dirac points in the momentum plane. By solving the Schrödinger equation for each of these Hamiltonians and then employing Eq. (3.11), we can compute the transmission probability due to the states in each cone separately. The small insert in the middle panel of Fig. 3.3(b) shows $\mathcal{T}(\theta)$ at $\epsilon = -0.2$ meV for the left and the right Dirac mini-cones in red and green, respectively. Transmission to the left mini-cone is zero at $\theta = 0$ and increases away from normal incidence, similar to the case of parabolic dispersion. Transmission to the right mini-cone, on the other hand, exhibits a maximum at $\theta = 0$ and slowly decreases for angles away from $\theta = 0$, which resembles the situation for monolayer graphene. [25] Therefore, the strain-induced mini-cones modify the chirality of the low-energy states.

For the strain axis oriented at $\phi = \pi/4$, we first verify numerically for every angle of incidence and energy which momenta correspond to plane waves moving

to the right (left) and evanescent waves decaying to the right (left), respectively. Then, we use Eqs. (3.10) and (3.11) and solve for the amplitude a_{-+} of the wave reflected back into the lead I, taking into account all physically allowed evanescent and propagating modes in region II. The transmission shown in the middle panel of Fig. 3.3(c) exhibits two distinct peaks, as long as the Fermi line is split into two pockets. For a small energy range below the LiTr in the valence band, $\mathcal{T}(\epsilon, \theta = 0) \neq 0$, which again can be attributed to the strain-induced modification of chirality of the low-energy states. Beyond the LiTr, where the effect of strain becomes weaker and the Fermi line becomes circular, we find that $\mathcal{T}(\epsilon, \theta = 0) \to 0$.

For the strain axis oriented at $\phi = \pi/2$ [with plane-wave parameters determined in Eq. (3.7)], for all transverse momenta and energies allowing for propagating states in region II the corresponding linear system of equations is again the same as in Eq. (3.13). By solving these equations numerically, we obtain the transmission probability shown in Fig. 3.3(d). As a function of the incidence angle θ, the transmission now exhibits two distinct peaks for all energies in the considered range. As in the non-strained case [Fig. 3.3(a)], this orientation of the strain delivers $\mathcal{T}(\epsilon < 0, \theta = 0) = 0$.

Irrespective of the modifications of chirality, in all four cases there is a marked difference in the transmission strength for $\epsilon > 0$ and $\epsilon < 0$. For $\epsilon < 0$, the interface is an n-p junction and an electron incoming from the conduction band of the lead (region I) emerges in the valence band at the right of the interface (region II). For $\epsilon > 0$, the electron stays in the conduction band both at the left and right of the interface, which is a better transmitting n-n' junction.

3.3.2 Conductance of an n-p junction

Based on the above results for the transmission probability, we employ the Landauer-Büttiker formalism [18] to calculate the conductance of the n-p or n-n' junction. Taking into account two valleys and two spins, as well as integrating over the angle of incidence and electron energy (as determined by the Fermi distribution with

finite temperature T), we arrive at the junction conductance,

$$G(\mu,T) = \frac{4e^2}{h}\frac{L_y}{\lambda_F}g, \tag{3.15}$$

$$g = \frac{1}{2\pi}\frac{1}{4k_BT}\int_{-\infty}^{\infty} d\epsilon \frac{\sqrt{\frac{2m\lambda_F^2}{\hbar^2}|\epsilon+V_0|}}{\cosh^2\left(\frac{\epsilon-\mu}{2k_BT}\right)} \times \int_{-\pi/2}^{\pi/2} \mathcal{T}(\epsilon,\theta)\cos(\theta)d\theta \ .$$

Here, $\lambda_F \approx 2\pi\hbar\sqrt{1/2mV_0}$ is the Fermi wavelength in lead I, k_B is the Boltzmann constant, and $\mathcal{T}(\epsilon,\theta)$ is the transmission at fixed energy and angle of incidence, determined above. By performing the integration numerically, we obtain the conductance as a function of chemical potential and temperature, which is shown in the right panels of Fig. 3.3.

For unstrained BLG [Fig. 3.3(a)], where the dispersion is parabolic, the conductance exhibits a minimum at $\mu = 0$ and has an asymmetric but monotonic behavior for both $\mu < 0$ (n-p junction) and $\mu > 0$ (n-n' junction). Furthermore, for $\mu = 0$, the conductance increases monotonously with temperature. In the strained cases [Figs. 3.3(b)-3.3(d)], the increase in conductance with temperature is still seen. However, depending on the strain orientation ϕ, $G(\mu,T)$ can be monotonic or non-monotonic. For $\phi = 0$ [Fig. 3.3(b)], the conductance at low temperatures exhibits an anomaly: in the region $\mu < 0$, there is an additional local minimum, as well as a local maximum. The local maximum is located at $\mu \approx -w$ ($\mu \approx -5$ meV for parameters used in the figure), which corresponds to the LiTr energy. For $\phi = \pi/4$ [Fig. 3.3(c)], the conductance at low temperatures exhibits a protrusion and a shift in slope, which again occur near the LiTr in the valence band. For $\phi = \pi/2$ [Fig. 3.3(d)], the conductance $G(\mu,T)$ is monotonic and quite similar to that calculated for BLG with a parabolic spectrum.

All conductance plots show an asymmetry about the minimum at $\mu = 0$. As discussed for the transmission probability, this difference is determined by the chiral sublattice structure of the plane waves, which in BLG suppresses the transmission at a potential step between regions of opposite polarity. Note that the anomalous behavior at $\mu = -w$ is specific for the n-p junction regime of the sys-

tem, and does not occur in the n-n' junction regime, which does not exhibit an anomaly at $\mu = w$. These features allow one to single out the anomalous T and μ dependence of the conductance for junctions with different orientation of the strain.

3.4 Transport across n-p-n and n-n'-n junctions

All the features found in the parametric dependencies of the transmission across a single potential step appear also in the transport properties of the two-terminal ballistic device (with two steps) sketched in Fig. 3.2. In particular, the $\epsilon \to -\epsilon$, and $\mu \to -\mu$ asymmetry and the anomalous temperature dependence at $\mu = -w$ (in the vicinity of the saddle point in the valence band) also persist in this "potential barrier" geometry, and indeed are further enhanced. In addition to those, the energy and angle dependence of the transmission coefficient acquires a resonance structure due to the interference between multiply reflected waves (Fabry-Pérot resonances). To take this into account, we compute the transmission of the device sketched in Fig. 3.2 considering both interfaces, as well as the ballistic electron propagation between the interfaces.

The transfer matrix $M_1 = B^{-1}A$ of the first interface is given by Eq. (3.10). Due to symmetry, the transfer matrix of the second interface is $M_2 = M_1^{-1} = A^{-1}B$. The transfer matrix of the whole system (n-p-n or n-n'-n junction) is then given by

$$\Xi = M_2 S M_1 = M_1^{-1} S M_1 \ , \tag{3.16}$$

where

$$S = \begin{pmatrix} e^{i\widetilde{p}_x^{++}L_x} & 0 & 0 & 0 \\ 0 & e^{i\widetilde{p}_x^{-+}L_x} & 0 & 0 \\ 0 & 0 & e^{i\widetilde{p}_x^{--}L_x} & 0 \\ 0 & 0 & 0 & e^{i\widetilde{p}_x^{+-}L_x} \end{pmatrix} \tag{3.17}$$

describes the ballistic electron propagation inside the "barrier" region II. Note that the factors in the matrices A and B that normalize the plane-wave states in

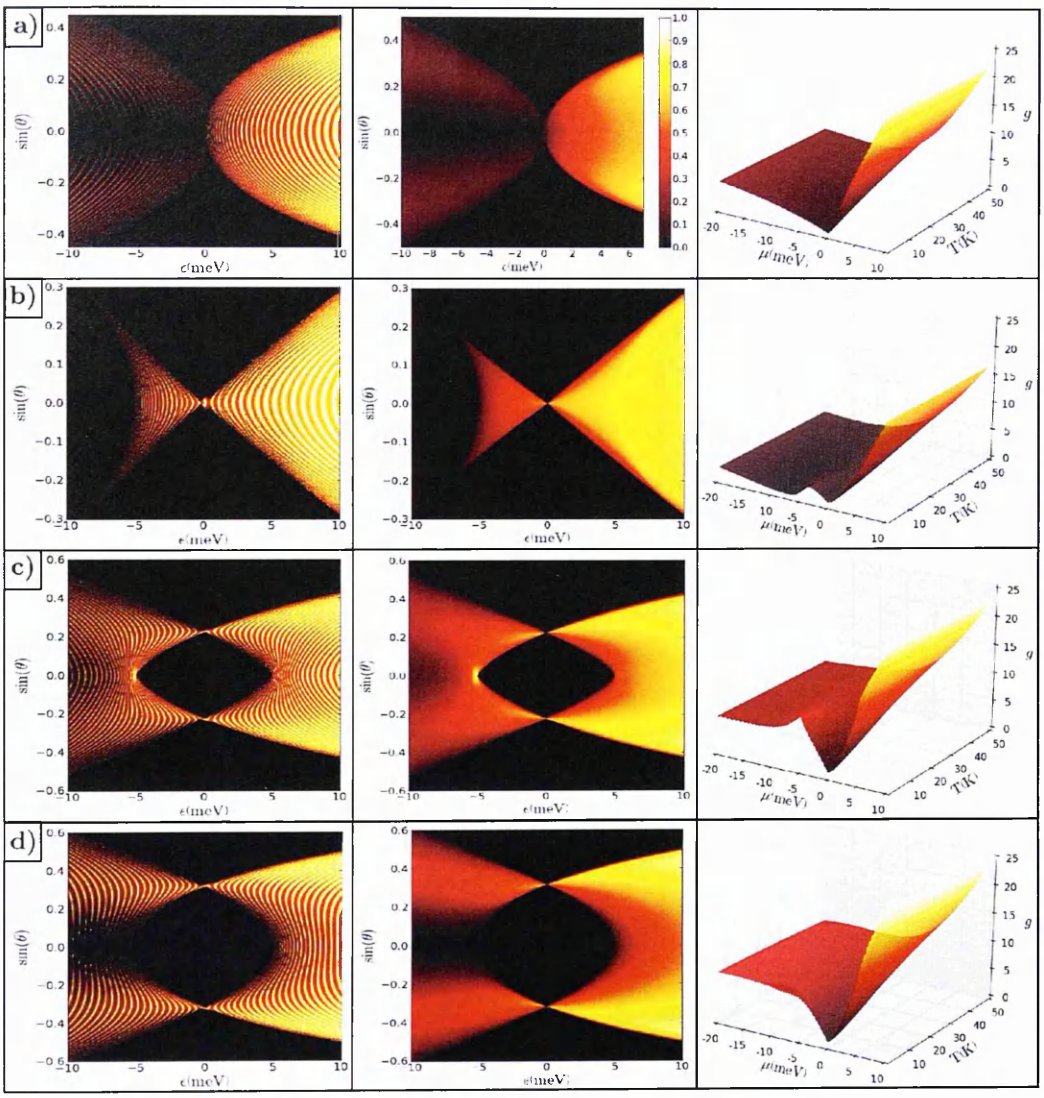

Figure 3.4: Transmission coefficient and conductance of n-p-n and n-n′-n junctions with non-strained bilayer graphene (a), as well as strained bilayer graphene with the uniaxial strain axis at an angle $\phi = 0$ (b), $\phi = \pi/4$ (c) and $\phi = \pi/2$ (d) from the crystallographic axis x. Left: transmission probability $\mathcal{T}(\epsilon, \theta)$ obtained in an exact calculation. Center: transmission probability obtained by averaging over fast oscillations after the contribution of evanescent waves is neglected. Right: linear response conductance as a function of chemical potential and temperature. All calculations are performed for experimentally accessible values $w = 5$ meV, $V_0 = 50$ meV, and $L_x = 1$ μm.

region II to normal flux cancel out in the matrix Ξ. From this, we can relate the amplitudes a_{ln} of the wave function in the source lead, Eq. (3.8), to the amplitudes c_{ln} of the wave function in the drain lead,

$$\Psi_{\mathrm{III}}(x) = \sum_{l,n} \frac{c_{ln}}{\sqrt{v_{ln}}} \begin{pmatrix} 1 \\ \alpha_{ln} \end{pmatrix} e^{ip_x^{ln} x},$$

by

$$\begin{pmatrix} c_{++} \\ c_{-+} \\ c_{--} \\ c_{+-} \end{pmatrix} = \Xi \begin{pmatrix} a_{++} \\ a_{-+} \\ a_{--} \\ a_{+-} \end{pmatrix}.$$

To determine the transmission coefficient

$$\mathcal{T}(\epsilon, \theta) = |c_{++}|^2, \tag{3.18}$$

we take boundary conditions $c_{-+} = c_{--} = a_{+-} = 0$, $a_{++} = 1$, and find c_{++} by solving the equation

$$\begin{pmatrix} c_{++} \\ 0 \\ 0 \\ c_{+-} \end{pmatrix} = \Xi \begin{pmatrix} 1 \\ a_{-+} \\ a_{--} \\ 0 \end{pmatrix}.$$

The numerically evaluated transmission probability $\mathcal{T}$ is plotted in the left panels of Fig. 3.4, for the same range of angles and energies (-10 meV$< \epsilon <$ 10 meV, $V_0 = 50$ meV and $w = 5$ meV) as in Fig. 3.3. As in Refs. [47, 108, 115], the presence of two reflective interfaces in a BLG device causes the appearance of resonances with high transmission. In the figure, these are seen as bright strips. The scale of the oscillations becomes finer for a longer sample length.

The right column in Fig. 3.4 shows the finite-temperature conductance in a long sample. The interference fringes are washed out by the smearing of the Fermi step [at $k_B T \gg \hbar^2/(mL_x^2)$] and by the integration over the angle. To obtain this finite-

temperature conductance, one can use the exactly calculated $\mathcal{T}(\epsilon,\theta)$ and insert this into Eq. (3.15). Here, we describe an accurate approximation of these results, which allows one to relate the pronounced anomalies of the finite-temperature conductance to angularly smoothed transmission probabilities $\langle\mathcal{T}\rangle$ (smeared over a small angle range $\delta\theta$ covering many oscillations), shown in the middle column in Fig. 3.4. Conveniently, in the limit of $L_x \to \infty$ but still within $\frac{L_x}{L_y} \gg 1$, evanescent modes die off before reaching the second interface, so that in region II only plane waves (with real $\widetilde{p}_x$) contribute toward transmission. To eliminate the negligible contribution of evanescent waves, we first restrict the analysis to the range of angles $\Delta\theta = 2\theta_c$ where plane waves exist inside the barrier; θ_c is energy dependent and different for each orientation of applied strain. Then, we group the exponents which emerge from Eq. (3.17) into propagating and decaying waves (where the latter have complex $\widetilde{p}_x$), and for decaying waves approximate $\tanh(|\mathrm{Im}[\widetilde{p}_x]|L_x) \to 1$ and $\cosh^{-1}(2|\mathrm{Im}[\widetilde{p}_x]|L_x) \to 0$. The conductance then follows from

$$G(\mu,T) = \frac{4e^2}{h}\frac{L_y}{\lambda_F} g \,, \tag{3.19}$$

$$g = \frac{1}{2\pi}\frac{1}{4k_BT}\int_{-\infty}^{\infty} d\epsilon \frac{\sqrt{\frac{2m\lambda_F^2}{\hbar^2}|\epsilon+V_0|}}{\cosh^2\left(\frac{\epsilon-\mu}{2k_BT}\right)} \times \int_{-\theta_c}^{\theta_c} \langle\mathcal{T}(\epsilon,\theta_0)\rangle \cos(\theta_0) d\theta_0 .$$

Since the details of the analysis of $\langle\mathcal{T}\rangle$ depend on the electron energy and on the orientation of the strain axis, we sketch the derivation separately for the corresponding characteristic parametric regimes.

Firstly, for the range of parameters for which Eq. (3.4) has only two real solutions, the described procedure leads to an expression of the form

$$\mathcal{T}(\epsilon,\theta) = \frac{X_1}{X_2 + X_3\cos\left(2\widetilde{p}_x^{++}L_x\right) + X_4\sin\left(2\widetilde{p}_x^{++}L_x\right)} .$$

Here, X_i are non-oscillating functions of p_x^{ln}, $\widetilde{p}_x^{ln}$, p_y, ϵ, V_0, w, and ϕ, which are not given explicitly due to their complexity. To average $\mathcal{T}(\epsilon,\theta)$, we first expand the real momenta in terms of small deviations $\delta\theta$ in the angle, $\theta = \theta_0 + \delta\theta$, about

some $-\theta_c < \theta_0 < \theta_c$, such that

$$\widetilde{p}_x^{++} = \widetilde{p}_x^{++}|_{\theta=\theta_0} + \delta\theta \left(\frac{\partial \widetilde{p}_x^{++}}{\partial \theta}\right)\Big|_{\theta=\theta_0}.$$

As such,

$$\mathcal{T}(\epsilon, \theta_0) = \frac{X_1}{X_2 + X_3 \cos(\Phi + \mathcal{A}\delta\theta) + X_4 \sin(\Phi + \mathcal{A}\delta\theta)},$$

where $\Phi = 2L_x\, \widetilde{p}_x^{++}|_{\theta=\theta_0}$ and $\mathcal{A} = 2L_x\, (\partial \widetilde{p}_x^{++}/\partial\theta)|_{\theta=\theta_0}$. Imposing $\mathcal{A}\Delta\delta\theta = 2\pi$, the average transmission over one period is

$$\begin{aligned}\langle \mathcal{T}(\epsilon, \theta_0)\rangle &= \frac{1}{2\pi}\int_0^{2\pi} \frac{X_1 dz}{X_2 + X_3\cos(z) + X_4 \sin(z)} \\ &= \frac{X_1}{\sqrt{X_2^2 - X_3^2 - X_4^2}}, \qquad z = \mathcal{A}\delta\theta.\end{aligned} \tag{3.20}$$

Secondly, for the range of parameters where Eq. (3.4) has four real solutions, $\widetilde{p}_x^{-+} = -\widetilde{p}_x^{++}$ and $\widetilde{p}_x^{+-} = -\widetilde{p}_x^{--}$ [such as encountered in Fig. 3.3(b)], fast oscillations in the transmission coefficient are due to combinations of $\sin(\widetilde{p}_x^{+n} L_x)$, $\sin(2\widetilde{p}_x^{+n} L_x)$, $\cos(\widetilde{p}_x^{+n} L_x)$, and $\cos(2\widetilde{p}_x^{+n} L_x)$. Expanding in terms of small deviations in angle,

$$\widetilde{p}_x^{+n} = \widetilde{p}_x^{+n}|_{\theta=\theta_0} + \delta\theta \left(\frac{\partial \widetilde{p}_x^{+n}}{\partial \theta}\right)\Big|_{\theta=\theta_0},$$

and denoting $\Phi_n = L_x\, \widetilde{p}_x^{+n}|_{\theta=\theta_0}$ and $\mathcal{A}_n = L_x\, (\partial \widetilde{p}_x^{+n}/\partial\theta)|_{\theta=\theta_0}$, we find that the interference fringes are encoded in the factors $\sin(\Phi_n + \mathcal{A}_n\delta\theta)$ and $\cos(\Phi_n + \mathcal{A}_n\delta\theta)$. Inspection of the constant pre-factors reveals that $\mathcal{A}_+ \approx \mathcal{A}_-$. Neglecting the phase Φ_n and imposing $\mathcal{A}_+\Delta\delta\theta = 2\pi$, the averaged transmission over one period can then be written as

$$\begin{aligned}\langle \mathcal{T}(\epsilon, \theta_0)\rangle &= \frac{1}{2\pi}\int_0^{2\pi} \frac{\mathcal{X}(z)}{\mathcal{Y}(z)} dz, \\ \mathcal{X}(z) &= (\bar{X}_1 \cos(z) + \bar{X}_2 \sin(z))^2, \\ \mathcal{Y}(z) &= \bar{X}_3 + \bar{X}_4 \cos(2z) + \bar{X}_5 \sin(2z) + \bar{X}_6 \cos(4z) + \bar{X}_7 \sin(4z),\end{aligned} \tag{3.21}$$

and $z = \mathcal{A}_+\delta\theta$; here $\bar{X}_i$ are non-oscillating functions of the same parameters as

in the previous cases. The specific expressions are again omitted because of their complexity.

In the analytical part of the studies of the transmission problem, all functions X_i and $\bar{X}_i$ have been found using the symbolic mathematical software Wolfram Mathematica. The results of the integrals in Eqs. (3.20) and (3.21) are shown in the central column in Fig. 3.4. The doping (chemical potential μ) and temperature dependence of the two-terminal conductance of the device follows from Eq. (3.19), and coincides with a high accuracy with the one calculated using Eq. (3.15) together with the exact values $\mathcal{T}(\epsilon, \theta)$.

The behavior of $G(\mu, T)$ in the right column of Fig. 3.4 displays all the features of the conductance of a single step in enhanced form. In particular, the conductance for $\phi = 0$ [Fig. 3.4(b)] exhibits a local maximum and a second local minimum positioned at the same chemical potentials as for a single junction. For $\phi = \pi/2$ [Fig. 3.4(d)] the conductance is monotonic. For $\phi = \pi/4$ [Fig. 3.4(c)] the protrusion in the conductance of a single junction (at the LiTr) has developed into a clear local maximum.

3.5 Conclusion

In this Chapter we have shown that the linear response conductance $G(\mu, T)$ of an *n-p-n* junction in strained bilayer graphene has a non-monotonic dependence on doping and temperature, which varies in size and form as a function of the crystallographic orientation of the principal strain axis. To understand this behavior we studied the transmission and conductance for a single interface (*n-p* junction), and used the obtained results to conclude that the non-monotonic behavior is due to the modification of chirality (thus, the feature responsible for the occurrence of the Klein paradox in graphene). Uniaxial strain changes the chirality (sublattice composition) of the electronic plane-wave states in the vicinity of the saddle point (Lifshitz transition) in the low-energy electron spectrum of strained bilayer graphene, which results in the observed non-monotonicity of the linear response conductance.

Chapter 4

Electronic properties of monolayer graphene superlattices

4.1 Introduction

Motivated by the unusual electronic properties of monolayer graphene (*i.e.* in some cases this material allows for the mimicking of QED phenomena under conditions that cannot be achieved in particle physics experiments) condensed matter physicists started extending the known properties of a two-dimensional electron gas (2DEG) in semiconductor materials to the relativistic 2D fermions (Dirac electrons) in graphene. One such system is represented by superlattice (SL) structures of periodically modulated potentials applied to graphene flakes. In this Chapter, we perform a comparison between the qualitative changes that emerge in the electronic spectrum of monolayer graphene systems due to such SL structures. First we consider a periodic modulation of the electrostatic potential profile [4, 6, 13, 43] after which we focus on spatially periodic lattice potentials [30, 53, 95, 123]. The former case can be analyzed by considering a periodically spaced square barrier system (an infinite series of n-p-n junctions) which can be achieved with the use of external gates, a construction theoretically developed by Kronig and Penney [52]. The latter scenario is obtained by placing graphene on an atomically flat crystal surface such as hexagonal boron nitride (hBN) [15, 30, 31, 48, 70, 118, 126]. The

incommensurability between graphene and the substrate, generated by the difference between their lattice constants and crystallographic misalignment, determines the formation of a hexagonal periodic structure known as a moiré pattern.

4.2 Periodic potentials in monolayer graphene

In the following, we study how a periodic modulation of the potential profile affects the electronic band structure of a device made of a wide strip of an ideally clean monolayer graphene flake. This structure, realized by a periodic array of gate electrodes that control the doping, and, thus, the Fermi energy of the electrons in each region of the flake, can be modeled as a one-dimensional square-wave potential perturbation $V(x)$, as shown in Fig. 4.1. We, therefore, consider a SL formed of an infinite number of periodically spaced barriers with unit cell length L_x with barrier and well widths αL_x and $(1-\alpha)L_x$, where $\alpha \in (0,1)$. The low-energy electronic dispersion of such a system, within the nearest-neighbor tight-binding model, is described by the effective Hamiltonian

$$\hat{H} = -\hbar v \boldsymbol{\sigma} \cdot \boldsymbol{p} + \mathbb{I} V_0 f\left(\cos\left(\frac{2\pi x}{L_x}\right)\right), \tag{4.1}$$

where $v = 10^6$ m/s is the Fermi velocity, $\boldsymbol{p}$ parameterizes the in-plane momentum relative to the $\boldsymbol{K}$ corner of the Brillouin zone, $\boldsymbol{\sigma}$ is the vector of Pauli matrices, $\mathbb{I}$ is the 2×2 unit matrix, V_0 is the height of the potential barrier, and

$$f(z) = \frac{1}{2}\left[1 + \mathrm{sign}(z - z_0(\alpha))\right], \quad z_0(\alpha) = \cos(\pi\alpha), \tag{4.2}$$

$$\mathrm{sign}(x) = \begin{cases} 1 & x \geq 0 \\ -1 & x < 0 \end{cases},$$

is a stepwise function.

To find the electronic dispersion, we employ the transfer matrix method [79]. Using separation of variables (allowed for a straight interface) the spinor eigen-

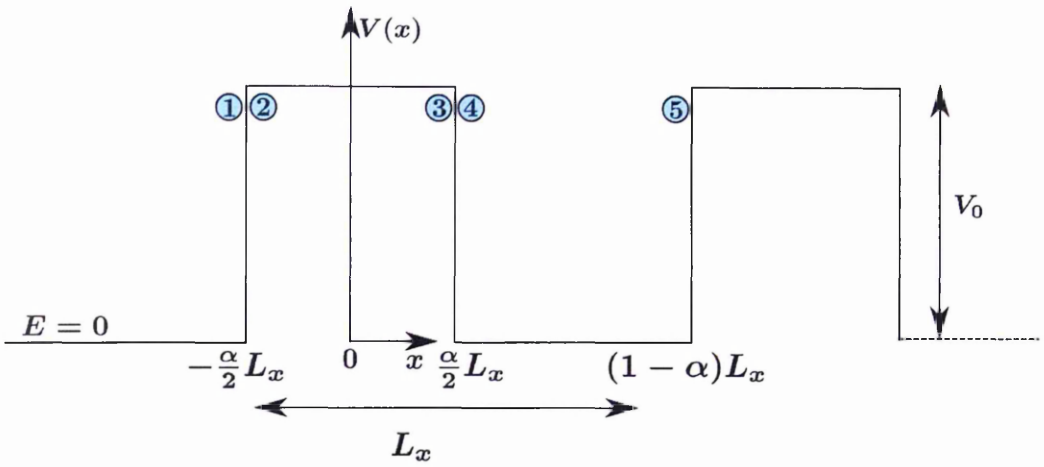

Figure 4.1: Diagram of periodic potential $V(x) = V_0 f(\cos\left(\frac{2\pi x}{L_x}\right))$ given by Eq. 4.2. The potential steps have height V_0 and width αL_x and are separated by potential wells of width $(1-\alpha)L_x$, where $\alpha \in (0,1)$. The different regions where the wave matching mechanism will be used are indicated by numbers.

states of Eq. 4.1 at $x = -\frac{\alpha}{2}L_x$ can be written as $\Phi_{1,2}(x,y) = \psi_{1,2}(x)e^{ik_y y}$, where

$$\psi_1 = a_1 \begin{pmatrix} 1 \\ a_{12} \end{pmatrix} e^{ik_x(x+\frac{\alpha}{2}L_x)} + a_2 \begin{pmatrix} 1 \\ a_{22} \end{pmatrix} e^{-ik_x(x+\frac{\alpha}{2}L_x)},$$
$$\psi_2 = b_1 \begin{pmatrix} 1 \\ b_{12} \end{pmatrix} e^{ik'_x(x+\frac{\alpha}{2}L_x)} + b_2 \begin{pmatrix} 1 \\ b_{22} \end{pmatrix} e^{-ik'_x(x+\frac{\alpha}{2}L_x)}. \tag{4.3}$$

Here indices $1,2$ indicate the first two regions of the periodic potential, and a_i, b_i where $i = 1,2$ are the wave amplitudes. [Note that primed terms are used to denote quantities inside the barrier.] The pseudospin elements and momenta are shown in Table 4.1, where for convenience we have introduced the dimensionless parameters

$$k_x = \frac{\tilde{k}_x}{L_x}, \quad k'_x = \frac{\tilde{k}'_x}{L_x}, \quad k_y = \frac{\tilde{k}_y}{L_x},$$
$$E = \tilde{E}u_0, \quad V_0 = \tilde{V}_0 u_0,$$

where $u_0 = \hbar v/L_x$. Since we assume an infinitely wide (in the transverse direction) graphene flake, the transverse momenta can be defined as $\tilde{k}_y = \tilde{k}_F \sin\theta$ (where $\tilde{k}_F$ is the Fermi momentum and θ is the angle of incidence of incoming electrons from

Elements	Momenta
$a_{12} = \frac{1}{\tilde{E}+\alpha\tilde{V}_0}(-\tilde{k}_x - i\tilde{k}_y)$	$\tilde{k}_x = \sqrt{-\tilde{k}_y^2 + \frac{1}{4}(\alpha\tilde{V}_0 + \tilde{E})^2}$
$a_{22} = \frac{1}{\tilde{E}+\alpha\tilde{V}_0}(\tilde{k}_x - i\tilde{k}_y)$	$\tilde{k}'_x = -\sqrt{-\tilde{k}_y^2 + \frac{1}{4}(\tilde{V}_0(1-\alpha) - \tilde{E})^2}$
$b_{12} = \frac{1}{\tilde{E}-(1-\alpha)\tilde{V}_0}(-\tilde{k}'_x - i\tilde{k}_y)$	$\tilde{k}_y = \tilde{k}_F \sin\theta$
$b_{22} = \frac{1}{\tilde{E}-(1-\alpha)\tilde{V}_0}(\tilde{k}'_x - i\tilde{k}_y)$	$\tilde{k}_F = \sqrt{\tilde{k}_x^2 + \tilde{k}_y^2}$

Table 4.1: Pseudospin elements and momenta for an *n-p-n* junction.

the source lead).

The transfer matrix $T_1 = B^{-1}A$, obtained using the wave matching method, relates the amplitudes a_i and b_i on the two sides of the interface between regions one and two according to

$$\begin{pmatrix} b_1 \\ b_2 \end{pmatrix} = T_1 \begin{pmatrix} a_1 \\ a_2 \end{pmatrix},$$

where

$$A = \begin{pmatrix} 1 & 1 \\ a_{12} & a_{22} \end{pmatrix} \quad B = \begin{pmatrix} 1 & 1 \\ b_{12} & b_{22} \end{pmatrix}.$$

The same procedure can be applied at the second interface at $x = \frac{\alpha}{2}L_x$ to obtain $T_2 = A^{-1}B$,

$$\begin{pmatrix} c_1 \\ c_2 \end{pmatrix} = T_2 \begin{pmatrix} b_1 \\ b_2 \end{pmatrix},$$

where we have assumed that the Fermi energy for $x < -\frac{\alpha}{2}L_x$ is the same as when $x > \frac{\alpha}{2}L_x$ (the potential steps are symmetric) and therefore the pseudospin amplitudes are the same in the two regions. Then the transfer matrix of a single symmetric *n-p-n* junction, as sketched in Fig. 4.2, is given by

$$T = T_2 S T_1 = T_1^{-1} S T_1,$$

where

$$S = \begin{pmatrix} e^{i\tilde{k}'_x \alpha L_x} & 0 \\ 0 & e^{-i\tilde{k}'_x \alpha L_x} \end{pmatrix}, \tag{4.4}$$

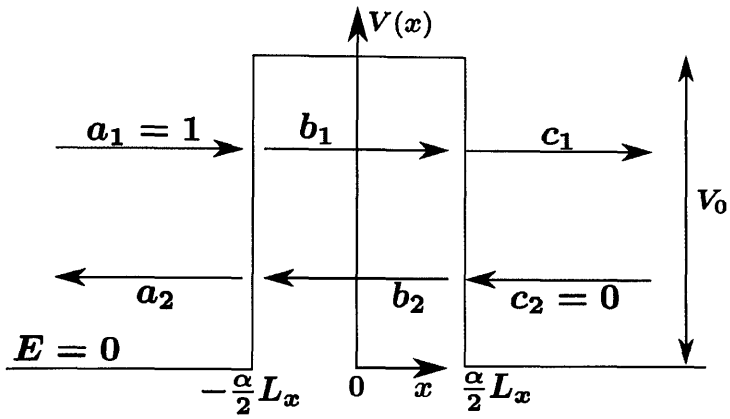

Figure 4.2: Schematics of an *n-p-n* junction in monolayer graphene with interfaces at $x = -\frac{\alpha}{2}L_x$ and $x = \frac{\alpha}{2}L_x$ respectively. The amplitudes of the incoming and outgoing plane waves, in the three regions of the junction, are also indicated.

describes the ballistic electron propagation inside the barrier region. Using T we can now relate the amplitudes a_i of the wave function in the source lead, Eq. 4.3, to the amplitudes of the wave functions in the drain lead, c_i, by

$$\begin{pmatrix} c_1 \\ c_2 \end{pmatrix} = T \begin{pmatrix} a_1 \\ a_2 \end{pmatrix}.$$

To derive the transfer matrix for quasiparticles traveling from region one to region five (across a total length L_x), $\psi_5(x) = \Xi\psi_1(x)$ we make the following remark: since, in an infinite array of potential barriers, regions one and five are identical due to symmetry, the spinor eigenstates in these two regions should be related by a Bloch phase ϕ, such that $\psi_5(x) = e^{i\phi}\psi_1$. These two equations then give the final transfer matrix

$$|\Xi - e^{i\phi}\mathbb{I}| = 0, \quad \Xi = S'A^{-1}BSB^{-1}A \tag{4.5}$$

where

$$S' = \begin{pmatrix} e^{i\tilde{k}_x(1-\alpha)L_x} & 0 \\ 0 & e^{-i\tilde{k}_x(1-\alpha)L_x} \end{pmatrix}.$$

is introduced to describe the electron propagation from region four to region five.

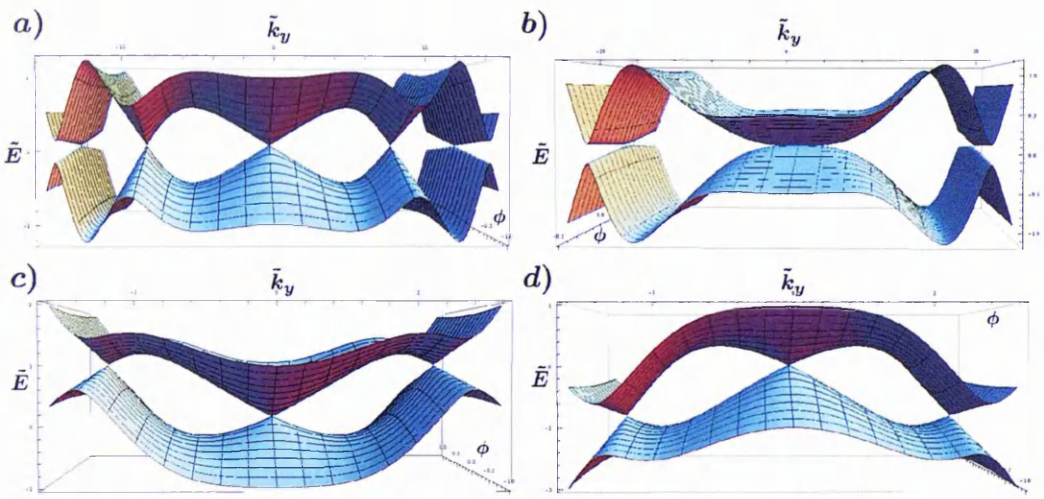

Figure 4.3: Energy dispersion surfaces with energy E plotted as a function of phase ϕ and momentum k_y for a Kronig-Penney system in monolayer graphene where the height of the potential step and its width are a) $\tilde{V}_0 = 10\pi$ and $\alpha = 0.5$, b) $\tilde{V}_0 = 4\pi$ and $\alpha = 0.5$, c)$\tilde{V}_0 = 6\pi$ and $\alpha = 0.4$, and d) $\tilde{V}_0 = 6\pi$ and $\alpha = 0.6$. These parameters were used to match the results of Ref. [4].

From Eqs. (4.5) we obtain the transcendental equation

$$\cos(\phi) - \cos[\alpha\tilde{k}_x]\cos[(\alpha-1)\tilde{k}_x] + \frac{\tilde{k}_y^2 - [\tilde{V}_0(\alpha-1)+\tilde{E}](\tilde{V}_0\alpha+\tilde{E})}{\tilde{k}_x\tilde{k}'_x}\sin[(\alpha-1)\tilde{k}_x]\sin[\alpha\tilde{k}'_x] = 0, \qquad (4.6)$$

that relates the energy $\tilde{E}$ to the momentum $\tilde{k}_y$ and phase angle ϕ. Given specific values for parameters $\tilde{V}_0$ and α, we solved Eq. 4.6 numerically and obtained the energy surface pots shown in Fig. 4.3.

As can be seen in Fig. 4.3 (a-d), the periodic modulation of the potential profile generates the appearance of additional Dirac points (DPs) in the dispersion. Using several values for the height $\tilde{V}_0$ and width αL_x of the potential barriers, we observe that the number of extra DPs varies with the potential height and that the energy at which they form depends on the barrier to well width ratio. For equal barrier and well widths, $\alpha = 0.5$, as shown in Fig. 4.3(a,b), the spectrum is symmetric about the Fermi level, $\tilde{E} = 0$, with the dispersion exhibiting two or four extra DPs about the main Dirac point. It has been shown by M. Barbier *et. al* [4, 6] that for such a SL the number of DPs in the dispersion is given by the equation $2 \times (\tilde{V}_0 \bmod 4\pi)$. Each time $\tilde{V}_0$ becomes a multiple of 4π a new pair of DPs is

generated for $k_y = 0$. This also gives the threshold of $\tilde{V}_0 = 4\pi$ as the height of the potential barrier for which the first pair is generated. For unequal barrier and well widths, Fig. 4.3 (c,d), the spectrum is no longer symmetric about the Fermi level. In these cases, the extra DPs are shifted downward (upward) in energy relative to the main Dirac point as αL_x increases (decreases). In all these cases the velocities of the new Dirac points are renormalized [4, 6]. Note that close to the main DP the electronic properties of graphene are still very well described by the 2D Dirac equation. Also, in the long wavelength limit, a Taylor expansion around $\tilde{V}_0 = 0$ restores the dispersion $\tilde{E} = \pm\sqrt{\tilde{k}_y^2 + \phi^2}$ of a single Dirac cone.

4.3 Moiré patterns in strained monolayer graphene[1]

Recent studies on monolayer graphene placed on hexagonal boron nitride (hBN), a material isostructural to graphene but with a 1.8% larger lattice constant [15, 30, 31, 48, 118, 126], showed that the crystallographic mismatch between the two lattices generates a periodic structure known as a moiré pattern [31, 50, 53, 88, 95, 123, 126, 127]. When the two honeycomb lattices are accurately aligned along their crystallographic directions, the beating of the lattice mismatch leads to the formation of a hexagonal moiré superlattice (SL) with wavelength much larger that the lattice constant [127]. The substrate-induced moiré potential [31, 126, 127] induces profound changes in the electronic spectrum of graphene, such as the appearance of second generation Dirac points (DPs) [30, 50, 51, 88, 89], observed experimentally in the tunneling density of states [127] and magnetotransport characteristics [45, 95], which are accompanied by the change of the effective sign of the charge carriers within graphene's conduction and valence bands [53, 95, 123]. Furthermore, the long wavelength periodicity of the moiré pattern provides an ideal-sized periodic modulation enabling experimental access to the rich physics expected in incommensurate quantum systems. When placing monolayer graphene hBN heterostructures in a magnetic field the spectrum develops a fractal structure known as the Hofstadter butterfly [44]. This effect is due to the interplay between

[1]Note that this section only contains preliminary results.

the characteristic lengths associated with the two quantizing fields: the magnetic field and the periodic electrostatic potential.

Such heterostructures have been created recently by transferring graphene onto hBN [45, 95, 126, 127], a process where mechanical deformations can be inflicted involuntarily. Therefore, in this Section we study the qualitative changes that can be induced in the electronic miniband spectrum of graphene on hBN by homogeneous strain. Our results show that strain couples to the misalignment angle resulting in distortions of the real space moiré pattern which amplify with increasing strain. We also identify an extreme case, where the moiré pattern becomes quasi-one-dimensional, and outline the condition for its occurrence. The considered model and all of the above mentioned results, are described in detail in Sec. 4.3.1 and in the corresponding subsections, with their graphic representations in Figs. 4.4 and 4.5.

4.3.1 Hamiltonian for a moiré superlattice in strained graphene on an almost commensurate hexagonal substrate

As previously described in Refs. [53, 123] in the case of graphene placed on hBN, the effect of the substrate perturbation on the Dirac electrons can be described phenomenologically in terms of the harmonic functions corresponding to the six smallest reciprocal lattice vectors of the moiré superlattice. At a distance d much larger than the spacing a between carbon atoms in graphene, the lateral variation of the wave function of the P^z carbon orbitals is smooth on the scale of a [10, 50, 62, 63, 127]. This observation permits an elegant continuum-model description of the interlayer coupling in structures such as graphene on hBN [53, 123] or in twisted bilayers [10, 88, 127, 127].

Here we consider a homogeneously strained graphene flake subjected to a hBN substrate with a slightly different lattice constant $(1+\delta)\sqrt{3}a$, where $|\delta| \ll 1$, as compared to that of unstrained graphene $\sqrt{3}a$, and a small misalignment angle $\theta \ll 1^o$. In contrast to an unstrained honeycomb lattice, with carbon-carbon bond length $r = 1.42\mathring{A}$, here the interatomic distances are modulated by the displacement

of the membrane and become

$$l_{ij} \simeq r(1 + \boldsymbol{n}_{ij} \cdot \hat{\boldsymbol{w}} \boldsymbol{n}_{ij}), \tag{4.7}$$

where ij denote pairs of nearest neighbors, $\boldsymbol{n}_{ij} = (0, 1), (\frac{\sqrt{3}}{2}, -\frac{1}{2}), (-\frac{\sqrt{3}}{2}, -\frac{1}{2})$ are the unit vectors along the carbon-carbon bonds in the unstrained honeycomb lattice and

$$\hat{\boldsymbol{w}} = w \begin{pmatrix} \cos^2\varphi - \sigma \sin^2\varphi & (1+\sigma)\cos\varphi \sin\varphi \\ (1+\sigma)\cos\varphi \sin\varphi & \sin^2\varphi - \sigma\cos^2\varphi \end{pmatrix} \tag{4.8}$$

is the strain tensor [94]. In the latter w parameterizes tensile strain, $\sigma = 0.165$ is the Poisson ratio for graphite [11] and φ is the angle between the principal axes of the strain tensor and the crystallographic direction of the crystal [$\varphi = 0$ ($\frac{\pi}{2}$) for strain along the zigzag (armchair) direction]. The modification of the graphene nearest neighbor bond lengths, and the fact that they become direction dependent, alters the real space moiré SL, as seen in Fig. 4.4 (Left column), and in turn, its reciprocal lattice vectors, shown in Fig. 4.4 (Central column). Then the moiré pattern harmonics are described by

$$\boldsymbol{b}_m(w, \theta) = \left[(\mathbb{I} + \hat{\boldsymbol{w}})^{-1} - (1+\delta)^{-1}\hat{R}_\theta\right] \hat{R}_{\frac{2\pi m}{6}} \begin{pmatrix} 0 \\ \frac{4\pi}{3a} \end{pmatrix}, \tag{4.9}$$

where $m = 0, \cdots, 5$ labels the reciprocal lattice vectors, $\mathbb{I}$ is the unit matrix and $\hat{R}$ represent anticlockwise rotations by θ and $\frac{2\pi m}{6}$ respectively..

When the strain is $w = 0$, the lengths of the harmonics $|\boldsymbol{b}_m| = \frac{4\pi}{3a}\sqrt{\delta^2 + \theta^2}$ are equal and they can be obtained from each other by the anticlockwise rotation $\hat{R}_{2\pi m/6}$ as discussed in Ref. [123]. In contrast, when the graphene lattice is strained, $w \neq 0$, the lengths of the reciprocal lattice vectors are no longer equal, see Fig. 4.4 (Center column). Furthermore, as the strain tensor $\hat{\boldsymbol{w}}$ and the anticlockwise rotations $\hat{R}_{\frac{2\pi m}{6}}$ do not commute, it is no longer true that the moiré harmonics can be obtained from each other by simple transformations. In this case Eq. (4.9) must be used to generate each harmonic individually. [Note that

the coupling between strain and rotations enhances the resulting deformation of the moiré superlattice.]

Even though on a substrate such as hBN, in which one of the atoms affects the graphene electrons more strongly than the other, the moiré potential can be modeled as a combination of a dominant inversion-symmetric part plus a small inversion-asymmetric perturbation. As the second term only brings small changes to the electronic spectrum, it can be neglected. Using a microscopic model [see Appendix B for a complete derivation] that is compatible with the symmetries of the system [9, 114, 123], and modeling the hBN substrate as a lattice of positively charged nitrogen nuclei in a homogeneous background of electron P^z orbitals, we arrive at the Hamiltonian

$$\hat{H}(w,\theta,\varphi=0) = v\boldsymbol{p}\cdot\boldsymbol{\sigma} + u_0\left[-\frac{1}{2}f_1(\boldsymbol{r},w,\theta)\mathbb{I} + \frac{\sqrt{3}}{2}f_2(\boldsymbol{r},w,\theta)\sigma_z\tau_z + \left(\hat{R}_{\frac{-\pi}{2}}\boldsymbol{f}_3(\boldsymbol{r},w,\theta)\right)\cdot\boldsymbol{\sigma}\tau_z\right]. \tag{4.10}$$

The Hamiltonian $\hat{H}$ acts on the four-component wave functions, $(\Psi_{AK}, \Psi_{BK}, \Psi_{BK'}, -\Psi_{AK'})^T$, which describe the electron amplitudes on the graphene A and B sublattices in the two valleys $\boldsymbol{K}$ and $\boldsymbol{K'}$. Here we have used the direct products $\sigma_i\tau_j$ of Pauli matrices where σ_i and τ_j act on the sublattice and valley indices respectively. The first term in $\hat{H}$ is the Dirac Hamiltonian, where $\boldsymbol{p} = -i\nabla$ is the momentum relative to one of the corners of the moiré Brillouin zone (BZ). The term with $f_1(\boldsymbol{r},w,\theta) = \sum_{m=0..5} e^{i\boldsymbol{b}_m(w,\theta)\cdot\boldsymbol{r}}$, describes a simple potential modulation. The third term, with $f_2(\boldsymbol{r},w,\theta) = i\sum_{m=0..5}(-1)^m e^{i\boldsymbol{b}_m(w,\theta)\cdot\boldsymbol{r}}$, accounts for the $A-B$ sublattice asymmetry locally imposed by the substrate. The last element, containing the vector $\boldsymbol{f}_3(\boldsymbol{r},w,\theta) = \sum_{m=0..5}(-1)^m\hat{\boldsymbol{b}_m}(0,0)e^{i\boldsymbol{b}_m(w,\theta)\cdot\boldsymbol{r}}$ where $\hat{\boldsymbol{b}_m}(0,0)$ are the reciprocal lattice unit vectors with $w=0$ and $\theta=0$, is a complex combination of two terms: one of which has zero rotor and can be gauged away and a second, with nonzero rotor, which describes the influence of the substrate on the $A-B$ hopping. The latter term can not be gauged away and can be interpreted as a pseudomagnetic field which has opposite signs in the two valleys $\boldsymbol{K}$ and $\boldsymbol{K'}$. The

coefficient $u_0 = 1/15$ in Eq. (4.10) is a dimensionless phenomenological parameter which was used in numerical calculations to set the strength of the perturbation.

4.3.2 Generic miniband spectra

To calculate the spectrum of Dirac electrons, as described by $\hat{H}$, we perform zone folding (in the graphene $\boldsymbol{K}$ valley) by bringing the states with momenta related by the reciprocal lattice vectors of the moiré pattern, $n_1\boldsymbol{b1} + n_2\boldsymbol{b2}$ (where n_1 and n_2 are integers) to the same point of the superlattice BZ, as shown in the panels of Fig. 4.4 (Center column). We then calculate the matrix elements of $\hat{H}$ between those states for each considered set of parameters (w, θ) and diagonalize the corresponding Heisenberg matrix numerically. The size of the matrix is chosen to ensure the convergence of the calculated energies for the three lowest conduction and valence minibands. Below we discuss the general features of the numerically calculated moiré miniband spectra obtained for the set of parameters $(w, \theta) = (0\%, 0^o)$, $(0.5\%, 0.23^o)$, $(1\%, 0.46^o)$, $(1.5\%, 0.69^o)$, and $(2\%, 0.92^o)$ respectively.

For the zero-energy Dirac point in graphene, only the $\boldsymbol{p} = 0$ states in each valley appear at $E = 0$ upon zone folding. As can be seen in all panels of Fig. 4.4 (Right column), for all considered parametric combinations (w, θ), the inversion-symmetric moiré perturbations does not open a gap in the Dirac spectrum at low energies, at the edge between the valence and conduction bands. [Note that the inversion-asymmetric perturbation can open a minigap [123] in the spectrum even in the absence of strain]. In a suspended monolayer graphene sheet, homogeneous strain only results in a small shift of the Dirac cones from the corners of the hexagonal Brillouin zone, without any qualitative change of the linear dispersion or the chiral properties of the electrons [23]. In the case of a graphene sheet on a hBN substrate a consequence of homogeneous deformations is also to slightly shift the main Dirac cone in the moiré miniband spectra. For the considered system, the shift of the otherwise unaltered main Dirac cone is directly proportional to the strength of the deformation and occurs along the k_x-axis.

The first considered parametric regime $(w, \theta) = (0\%, 0^o)$, shown in the top

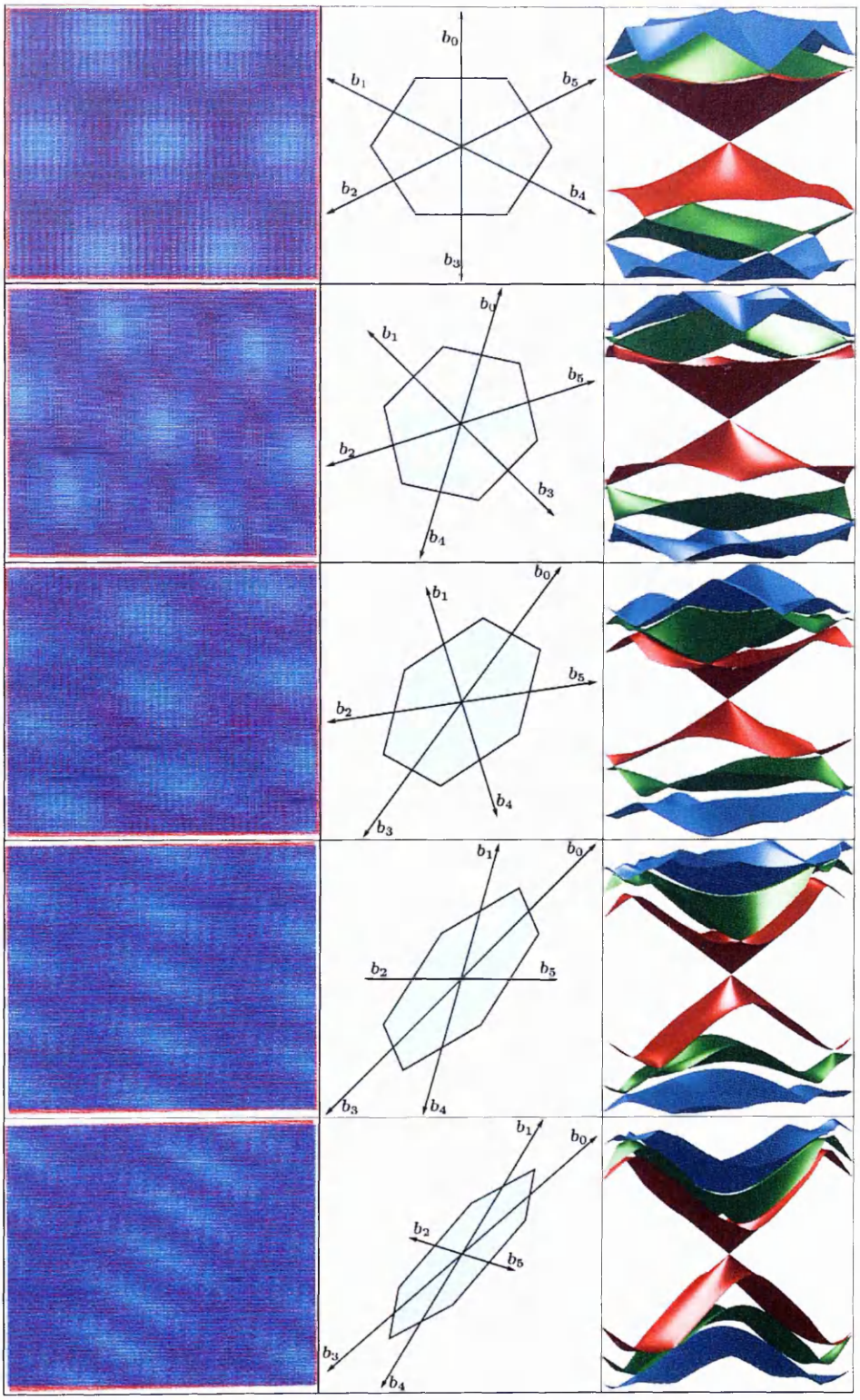

Figure 4.4: Left column: Real space moiré pattern for combinations of strain and misalignment angle: $(w, \theta) = (0\%, 0^o)$, $(0.5\%, 0.23^o)$, $(1\%, 0.46^o)$, $(1.5\%, 0.69^o)$, and $(2\%, 0.92^o)$ respectively. Center column: The corresponding reciprocal lattice vectors and the moiré superlattice BZ. Right column: The corresponding dispersions within the first BZ.

row of Fig. 4.4, describes a heterostructure with no misalignment angle and in the absence of strain. The spectrum of such a system exhibits several second generation DPs in the valence bands, at the edge of the first BZ. In contrast, in the conduction bands similar features are obscured by overlapping spectral branches. All other considered parametric regimes, ($w \neq 0\%, \theta \neq 0^o$), display strained real space moiré patterns (Left column) and BZs (Central column), which translate into deformed dispersions, as shown in Fig. 4.4 (Right column). We observe that in almost all of the above plots, with the exception being the last case with ($w = 2\%, \theta = 0.92^o$), mechanical deformations of the graphene lattice do not interfere with the formation of anisotropic mini Dirac cones in the valence bands, however, they do lead to the opening of minigaps. For the parametric regime with ($w = 2\%, \theta = 0.92^o$), the spectral minibands become clearly separated and curved, obscuring the presence of any secondary Dirac point. In all considered cases, the Dirac spectrum is not symmetric between the valence and conduction bands and, if present, the mini Dirac cones in the conduction bands are always concealed.

Notice that for the parameters used in Fig. 4.4 the superlattice BZ becomes narrower as the strain and misalignment angle are increased, however, this trend is non-monotonic. For specific values of θ the superlattice BZ becomes completely flat (with $S_{BZ} = 0$ area) and the real space moiré pattern becomes quasi-1D periodic. Any further increase in the value of θ would start restoring the 2D character of the superlattice and increase the BZ size.

4.3.3 Strain-induced crossover from 2D to a quasi-1D moiré pattern

As described above, the main consequence of homogeneous deformations in a graphene layer on a hBN substrate is that the real space moiré pattern and implicitly the superlattice BZ become strained. In the remainder of this chapter we explore an extreme scenario, where the superlattice BZ exhibits a singular behavior (by becoming completely flat), and describe its consequences on the moiré spectral minibands.

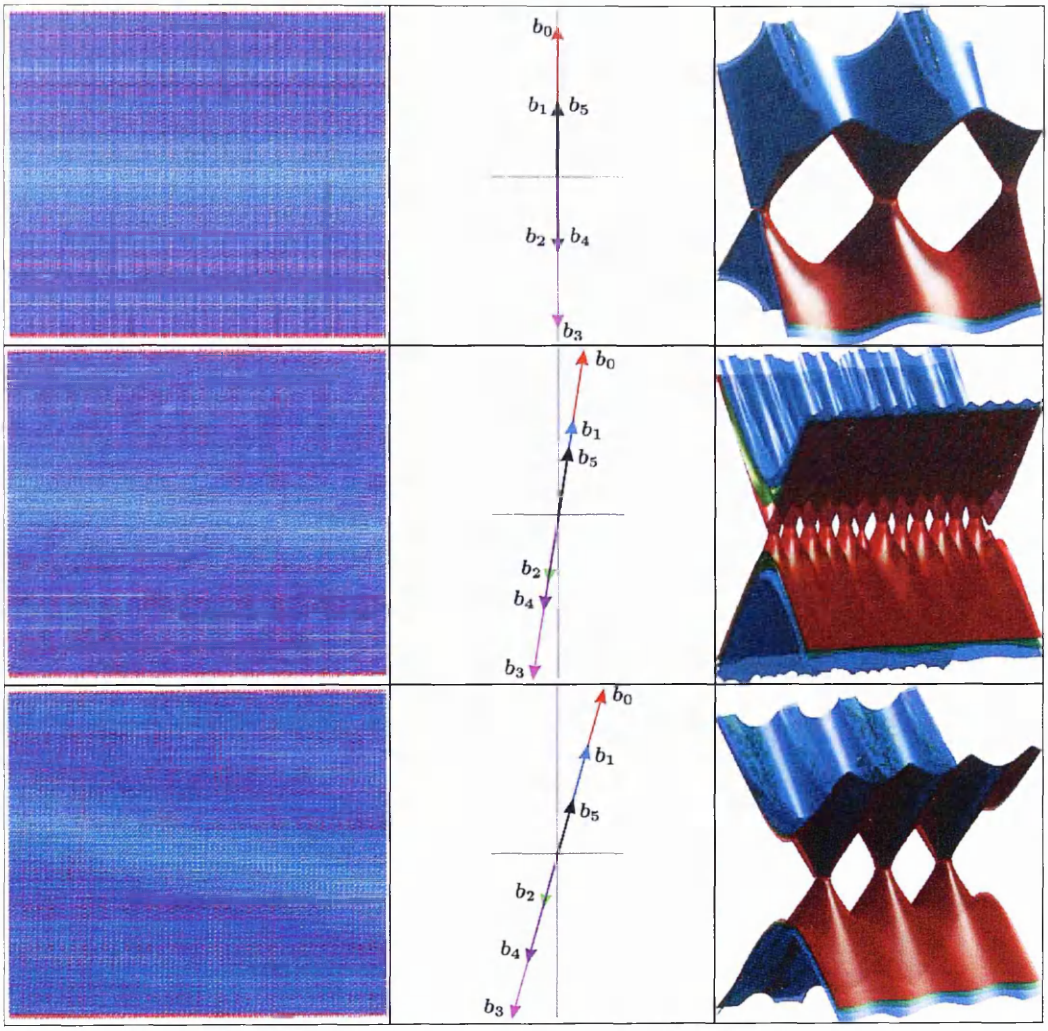

Figure 4.5: Left column: Real space quasi-one-dimensional moiré pattern for combinations of strain and misalignment angle: $(w_c, \theta) = (1.8\%, 0^o)$, $(1.82\%, 0.12^o)$ and $(1.88\%, 0.23^o)$ respectively. Center column: The corresponding reciprocal lattice vectors $\boldsymbol{b}_m$ with $m = 0, \cdots, 5$ (red, blue, green, magenta, purple, black) and the flatten moiré superlattice BZ. Right column: The corresponding dispersions.

The complete flattening of the superlattice BZ implies that all the reciprocal lattice vectors $\boldsymbol{b}_m$ become parallel (aligned along the same line). By imposing this condition on the six smallest moiré harmonics, we arrive at the following requirement for the critical value of homogeneous strain,

$$w_c(\theta) = \frac{1}{2\sigma}\Big[(1-\sigma)[1-(1+\delta)\cos\theta] + \sqrt{(1-\sigma)^2[1-(1+\delta)\cos\theta]^2 + 4\sigma[1+(1+\delta)^2-2(1+\delta)\cos\theta]}\Big], \quad (4.11)$$

which is independent of the orientation of applied strain φ. The above equation

implies that for each value of the misalignment angle θ, there is a value of strain for which the moiré superlattice BZ becomes a line.

Using parametric regimes (w_c, θ) that satisfy the condition in Eq. 4.11 we obtain the results shown in Fig. 4.5. The first consequence of the complete flattening of the superlattice BZ, is that the real space moiré pattern undergoes a transition from 2D to quasi-1D, as seen in Fig. 4.5 (Left column). For the first considered parametric regime ($w_c = 1.8\%, \theta = 0^o$), which is also the first pair of parameters that satisfy Eq 4.11, the graphene sheet is stretched along the x-axis to exactly compensate the lattice mismatch with the hBN substrate. In this scenario the moiré pattern is infinitely periodic in the direction perpendicular to the harmonics and has a vary large periodicity in the direction along the harmonics. In contrast, for all other parametric regimes [$(1.82\%, 0.12^o)$ and $(1.88\%, 0.23^o)$ respectively], the periodicity of the moiré pattern in the direction along the reciprocal lattice vectors decreases with increasing misalignment angle and strain. Another observable difference, seen in Fig. 4.5 (Center column), is that the reciprocal lattice vectors are commensurate only for the first parametric regime, with $\boldsymbol{b}_0$ and $\boldsymbol{b}_3$ being twice the size of $\boldsymbol{b}_1 = \boldsymbol{b}_5$ and $\boldsymbol{b}_2 = \boldsymbol{b}_4$ respectively. In all other cases the usual relationships among harmonics remain unchanged (for example $\boldsymbol{b}_0 = \boldsymbol{b}_1 + \boldsymbol{b}_5$) however they are not commensurate.

As the moiré BZ becomes flat, the coupling between states in the first BZ and in the higher order BZs increases. As such, to calculate the dispersion of the quasi-1D moiré patterns we must consider an increased number of states and therefore a larger size for the Heisenberg matrix when performing zone folding, to ensure convergence for the three lowest valence and conduction bands. The results of our numerical calculation for the miniband spectra are shown in Fig. 4.5 (Right column). As it can be seen in all figures, the effect of homogeneous deformations has a much greater impact in this case and results in qualitative changes of the moiré miniband spectra as opposed to simple shifts of the main Dirac cone in the momentum plane. The first and the last considered set of parameters $(w_c, \theta) = (1.8\%, 0^o)$ and $(1.88\%. 0.23^o)$ reveal strongly altered dispersions, where the three lowest va-

lence and conduction bands are closely packed. More interestingly, for the second set of parameters $(1.82\%, 0.12^o)$, the complexity of the moiré spectra increases and the three valence and conduction bands become slightly separated. The observed difference is due to the incommensurability of the reciprocal lattice vectors in the second case, where the various beatings lead to the formation of additional Dirac cones in the first BZ. [Note that in the last case $(w_c, \theta) = (1.88\%, 0.23^o)$ the reciprocal lattice vectors are almost commensurate. Therefore, the dispersion resembles the one obtained for $(w_c, \theta) = (1.8\%, 0^o)$.]

4.4 Conclusion

Using a general symmetry based approach, we study the generic miniband structure for electrons in homogeneously strained monolayer graphene placed on a hexagonal boron nitride substrate. In particular we find that mechanical deformations couple to the misalignment angle between the two honeycomb lattices, alters the beating of the lattice mismatch, and leads to the formation of strained moiré superlattices. We also observe that in some cases, this leads to the opening of minigaps in the anisotropic mini Dirac cones in the valence bands at the edge of the first Brillouin zone of the superlattice. Furthermore, we identify an extreme parametric regime where the moiré patterns become quasi-1D, and emphasize that in this case homogeneous deformations lead to qualitative changes in the moiré miniband spectrum.

Chapter 5

General Conclusions

Since graphene uniquely combines a series of properties like mechanical strength, high electronic and thermal conductivities and impermeability, this material is a suitable candidate for numerous future applications such as, for example, flexible and/or transparent electronics, fast photo-detectors, effective photocells, and chemical sensors, to name just a few. Recent works on the effect of lattice deformations in graphene, revealed that this crystal behaves like an elastic membrane that is capable of withstanding reversible deformations of up to 10%. The peculiar way in which strain affects the already unusual electronic properties of this material stimulated the proposal of various setups aiming at controlling the electronic structure of graphene by means of strain engineering. Prompted by the constant need for the miniaturization of electronic devices as well as the desire of developing graphene nano-sized electronics, in this thesis we theoretically investigated the influence of mechanical deformations on the electronic transport properties of graphene structures, an area which remained unexplored thus far.

Our results show that artificially imposed homogeneous deformations coupled to the size confinement effects, in graphene nanoibbons, lead to the appearance of transport gaps and resonances in the conductance of such systems. We also outline that the observed resonances are robust in the presence of 'double atom' edge defects, but are destroyed by 'single atom' edge defects. For the case of inhomogeneous mechanical deformations, we have found that the inhomogeneity

developed near the contacts aids the resonant transmission of charge carriers either through a mode mixing mechanism or through the sublattice-polarized $n = 0$ pseudo-magnetic Landau level. The former leads to the formation of Fabry-Pérot-like standing waves, in the central homogeneously strained part of the ribbon, which result in the formation of conductance peaks far from the Dirac point. For the latter case, the states form near the contact regions and give rise to two groups of resonances near the Dirac point, each containing a pair of conductance peaks.

In the case of homogeneously strained bilayer graphene we have shown that the linear response conductance of an n-p-n junction has a non-monotonic dependence on doping and temperature, which varies in size and form as a function of the crystallographic orientation of the principal strain axis. We began our analysis by studying the transport properties of a single interface (n-p junction), and used the obtained results on transmission and conductance to conclude that the non-monotonic behavior is due to the modification of the chirality of the low-energy electronic states. Therefore, uniaxial strain changes the sublattice composition of the electronic plane-wave states in the vicinity of the Lifshitz transition in the low-energy electron spectrum of strained bilayer graphene, which leads to the observed non-monotonicity of the linear response conductance.

We finalize this work with a study of the generic miniband structure for electrons in homogeneously strained monolayer graphene placed on a hexagonal boron nitride substrate. In this work we found that mechanical deformations alter the beating of the lattice mismatch between the two lattices, and lead to the formation of strained moiré superlattices. We also observe that in some cases, this determines the opening of minigaps in the mini Dirac cones in the valence bands at the edge of the first Brillouin zone of the superlattice. Furthermore, we identify an extreme parametric regime where the moiré patterns become quasi-1D, and emphasize that in this case homogeneous deformations lead to the appearance of additional Dirac cones in the spectrum.

Appendix A

Recursive Green's functions method

A.1 Introduction

In the following notes we will describe a general mechanism that makes use of the recursive Green's function method to find the transport properties of nanostructures. We will describe, in detail, the general method, in Sec. A.2, without referencing to a particular shape or orientation of the lattice structure of either the leads nor the scattering region. Our only assumption is that the semi-infinite leads are described by a periodically repeated unit block chosen such that only interactions between adjacent cells exist. In Chapter 2 we make use of this mechanism to study the transport properties of armchair graphene nanoribbons.

A.2 Recursive Green's function method

A.2.1 Model for the leads

Eigenfunctions and eigenvalues

The semi-infinite leads are composed of a periodically repeated unit cell, chosen large enough such that all couplings are only between adjacent cells. The Hamil-

tonian and eigenfunctions of the leads are

$$\mathcal{H}_L = \begin{pmatrix} \ddots & \vdots & \vdots & \vdots & \vdots \\ \cdots & H_0 & V_L & 0 & 0 \\ \cdots & V_L^\dagger & H_0 & V_L & 0 \\ \cdots & 0 & V_L^\dagger & H_0 & V_L \\ \cdots & 0 & 0 & V_L^\dagger & H_0 \end{pmatrix}, \quad \varphi_L = \begin{pmatrix} \lambda_{Lm}^{-n}\psi_{Lm} \\ \vdots \\ \lambda_{Lm}^{-2}\psi_{Lm} \\ \lambda_{Lm}^{-1}\psi_{Lm} \\ \psi_{Lm} \end{pmatrix}, \tag{A.1}$$

$$\mathcal{H}_R = \begin{pmatrix} H_0 & V_R & 0 & 0 & \cdots \\ V_R^\dagger & H_0 & V_L & 0 & \cdots \\ 0 & V_R^\dagger & H_0 & V_R & \cdots \\ 0 & 0 & V_R^\dagger & H_0 & \cdots \\ \vdots & \vdots & \vdots & \vdots & \ddots \end{pmatrix}, \quad \varphi_R = \begin{pmatrix} \psi_{Rm} \\ \lambda_{Rm}^{1}\psi_{Rm} \\ \lambda_{Rm}^{2}\psi_{Rm} \\ \vdots \\ \lambda_{Rm}^{n}\psi_{Rm} \end{pmatrix}, \tag{A.2}$$

where we enumerate the blocks by an index $n \geq 0$, so that the first block in both the left and right lead is $n = 0$. Then the wave function in the n^{th} block is $\psi^{(n)}$. Bloch's theorem guarantees that we can find solutions of the form

$\star$ Right Lead:

$$\psi_{Rm}^{(n)} = \lambda_{Rm}^n \psi_{Rm}^{(0)} = \lambda_{Rm}^n \psi_{Rm} \tag{A.3}$$

where ψ_{Rm} is the solution in the $n = 0$ block [Note n increases in the positive x direction]. Then, omitting the subscript m, one obtains

$$\begin{aligned} &V_R^\dagger(\lambda^{n-1}\psi_R) + (H_0 - E)(\lambda^n\psi_R) + V_R(\lambda^{n+1}\psi_R) = 0 \\ &\Rightarrow (E - H_0)\psi_R - V_R^\dagger(\lambda^{-1}\psi_R) = V_R(\lambda\psi_R). \end{aligned} \tag{A.4}$$

Using the substitution $\phi = \lambda^{-1}\psi_R$ we convert this into a generalized eigenvalue problem

$$\begin{pmatrix} 0 & 1 \\ -V_R^\dagger & E - H_0 \end{pmatrix} \begin{pmatrix} \phi \\ \psi_R \end{pmatrix} = \lambda \begin{pmatrix} 1 & 0 \\ 0 & V_R \end{pmatrix} \begin{pmatrix} \phi \\ \psi_R \end{pmatrix}. \tag{A.5}$$

⋆ Left Lead:

$$\psi_{Lm}^{(-n)} = \lambda_{Lm}^{-n}\psi_{Lm}^{(0)} = \lambda_{Lm}^{-n}\psi_{Lm} \tag{A.6}$$

where ψ_{Lm} is the solution in the $n = 0$ block [Note n increases in the negative x direction]. Then, omitting the subscript m, one obtains

$$\begin{aligned} &V_L^\dagger(\lambda^{-n-1}\psi_L) + (H_0 - E)(\lambda^{-n}\psi_L) + V_L(\lambda^{-n+1}\psi_L) = 0 \\ &\Rightarrow (E - H_0)\psi_L - V_L^\dagger(\lambda^{-1}\psi_L) = V_L(\lambda\psi_L). \end{aligned} \tag{A.7}$$

Using, again, the substitution $\psi = \lambda^{-1}\Psi_L$ we convert this into a generalized eigenvalue problem

$$\begin{pmatrix} 0 & 1 \\ -V_L^\dagger & E - H_0 \end{pmatrix} \begin{pmatrix} \phi \\ \psi_L \end{pmatrix} = \lambda \begin{pmatrix} 1 & 0 \\ 0 & V_L \end{pmatrix} \begin{pmatrix} \phi \\ \psi_L \end{pmatrix}. \tag{A.8}$$

If the leads are identical, with $V_L = V_R$, the generalized eigenvalue problems are identical as well. It is then enough to solve for the eigenvalues and eigenvectors in the right lead, for example, and use them to build the wave functions for the left lead.

Characterization of modes

To discriminate between right and left propagating or decaying modes we use the suggestion of Ref. [28] and incorporate the boundary conditions into the eigenvalue problem itself. This amounts to adding a small imaginary part η to the energy. If $\eta > 0$ then the wavenumber acquires a positive imaginary component, which makes the Advanced Green's function (incoming mode) grow indefinitely as we move deeper into the leads. Because a correct solution must be bounded, only the Retarded Green's function (outgoing mode)is acceptable as a solution. Oppositely if $\eta < 0$ only the Advanced Green's function is bounded, and thus the acceptable solution, where as the Retarded Green's function grows indefinitely. For evanescent modes, the addition of a small imaginary part to the energy makes virtually no difference.

Therefore we solve the eigenvalue problem for the right lead and group the resulting eigenvectors into rectangular matrices of column vectors according to the following selection rules:

- Ψ_R : all solutions ψ_{Rm} with $0 < |\lambda_{Rm}(E + i0^+)| < 1$. These are outgoing (right-going) propagating modes or evanescent modes that decay for $n \to \infty$.
- Ψ'_R: all solutions ψ_{Rm} with $0 < |\lambda_{Rm}(E - i0^+)| < 1$. These are incoming(left-going) propagating modes or evanescent modes that decay for $n \to \infty$.
- $\tilde{\Psi}_R$: all solutions $\psi_{Rm}m$ with $|\lambda_{Rm}(E+i0^+)| > 1$. These are either incoming(left-going) propagating modes or the unphysical evanescent modes that increase for $n \to \infty$.

We also define diagonal matrices Λ_R, Λ'_R, and $\tilde{\Lambda}_R$, comprised of the corresponding eigenvalues λ_{Rm} of each respective set.

Because the eigenvalue problems, in the two leads, are identical we define $\Psi_L = \Psi_R$, $\Psi'_L = \Psi'_R$, $\tilde{\Psi}_L = \tilde{\Psi}_R$, $\Lambda_L = \Lambda_R$, $\Lambda'_L = \Lambda'_R$, and $\tilde{\Lambda}_L = \tilde{\Lambda}_R$. Note that if the form of their corresponding Hamiltonians is kept as above and $V_L = V_R$, then the two leads would match commensurably if connected directly to each other (They would form a continuous ribbon). Then, using the interface connecting the leads as a reference, right-propagating modes in the right/left lead are outgoing/incoming.

Since we did not specify anything concrete about the lattice structure we must mention that for some structures, bound states might appear. They can span several unit cells and still couple to the system. In the generalized eigenvalue problem they are singular and appear at certain fixed energies, however they have undetermined eigenvalues λ_m, which is why the sets of Bloch states described above are not always complete. When these bound states couple to the scatterer they become relevant for all energies. We will however, only use this mechanism for armchair graphene nanoribbons. For zigzag edge ribbons such bound states do not appear, however for the armchair edge they might appear at certain widths. In Chapter 2 we will consider such configurations of the lattice, such that bound states do not couple to the system and thus neglect them in our calculations.

Orthogonality of Bloch modes with indices $n \neq m$

From the Schrödinger's equation, Eq. A.5, and using Bloch's theorem, Eq. A.4, we obtained for the right lead (omitting the subscript R)

$$(E - H_0)\psi_m = V^\dagger \psi_m \lambda_m^{-1} + V\psi_m \lambda_m, \tag{A.9}$$

$$(E - H_0)\psi_n = V^\dagger \psi_n \lambda_n^{-1} + V\psi_n \lambda_n, \tag{A.10}$$

for states with different indices $m \neq n$. Then

$$\psi_n^\dagger (E - H_0)\psi_m = \psi_n^\dagger V^\dagger \psi_m \lambda_m^{-1} + \psi_n^\dagger V\psi_m \lambda_m. \tag{A.11}$$

But because H_0 is Hermitian

$$\begin{aligned}
\psi_n^\dagger (E - H_0)\psi_m &= [(E - H_0)\psi_n]^\dagger \psi_m \\
&= [V^\dagger \psi_n \lambda_n^{-1} + V\psi_n \lambda_n]^\dagger \psi_m \\
&= [\lambda_n^{*^{-1}} \psi_n^\dagger V + \lambda_n^* \psi_n^\dagger V^\dagger]\psi_m \\
&= \lambda_n^{*^{-1}} \psi_n^\dagger V\psi_m + \lambda_n^* \psi_n^\dagger V^\dagger \psi_m.
\end{aligned} \tag{A.12}$$

Thus we obtain the equality

$$\psi_n^\dagger V^\dagger \psi_m \lambda_m^{-1} + \psi_n^\dagger V\psi_m \lambda_m = \lambda_n^{*^{-1}} \psi_n^\dagger V\psi_m + \lambda_n^* \psi_n^\dagger V^\dagger \psi_m, \tag{A.13}$$

which gives

$$\psi_n^\dagger V^\dagger \psi_m \lambda_m^{-1} - \lambda_n^{*^{-1}} \psi_n^\dagger V\psi_m = 0. \tag{A.14}$$

From the above results we can write

$$\begin{cases} \psi_n^\dagger V^\dagger \psi_m \lambda_m^{-1} - \lambda_n^{*^{-1}} \psi_n^\dagger V \psi_m = 0 \\ \psi_m^\dagger V^\dagger \psi_n \lambda_n^{-1} - \lambda_m^{*^{-1}} \psi_m^\dagger V \psi_n = 0 \end{cases},$$

$$\Rightarrow 0 = (\psi_n^\dagger V^\dagger \psi_m \lambda_m^{-1} + \psi_m^\dagger V^\dagger \psi_n \lambda_n^{-1}) - (\psi_m^\dagger V^\dagger \psi_n \lambda_n^{-1} + \psi_n^\dagger V^\dagger \psi_m \lambda_m^{-1})^\dagger$$

$$\Rightarrow 2i\mathrm{Im}(\psi_n^\dagger V^\dagger \psi_m \lambda_m^{-1} + \psi_m^\dagger V^\dagger \psi_n \lambda_n^{-1}) = 0$$

$$\Rightarrow \frac{2}{\hbar}\mathrm{Im}(\psi_n^\dagger V^\dagger \psi_m \lambda_m^{-1} + \psi_m^\dagger V^\dagger \psi_n \lambda_n^{-1}) = 0. \tag{A.15}$$

Eq. A.15 gives the orthogonality relation for two Bloch states with different indices. From this we can also write

$$\Psi_R^\dagger V_R^\dagger \tilde{\Psi}_R \tilde{\Lambda}_R^{-1} = \Lambda_R^{*^{-1}} \Psi_R^\dagger V_R \tilde{\Psi}_R, \tag{A.16}$$

$$\Psi_L^\dagger V_L^\dagger \tilde{\Psi}_L \tilde{\Lambda}_L^{-1} = \Lambda_L^{*^{-1}} \Psi_L^\dagger V_L \tilde{\Psi}_L \Leftrightarrow \Lambda_L^* \Psi_L^\dagger V_L^\dagger \tilde{\Psi}_L = \Psi_L^\dagger V_L \tilde{\Psi}_L \tilde{\Lambda}_L, \tag{A.17}$$

for the two leads. These formulae are necessary in the proof of unitarity of the scattering matrix.

Calculation of Currents

From the Schrödinger equation ($i\hbar\frac{\partial\psi}{\partial t} = \mathcal{H}\psi$) we can obtain the continuity equation

$$\frac{d}{dt}|\psi^{(n)}|^2 = I^{(n-1,n)} - I^{(n,n+1)}, \tag{A.18}$$

for both the left and right leads, which gives the probability conservation locally[105], at position n, as the "in flow" minus the "out flow".[Note that $n < 0$ in the left lead.] The probability current (the rate at which probability is "flowing") is given by

$$I_m^{(n,n+1)} = \frac{2}{\hbar}\,\mathrm{Im}(\psi_m^{\dagger(n+1)} V^\dagger \psi_m^{(n)}). \tag{A.19}$$

Imposing current conservation ($\frac{d}{dt}|\psi^{(n)}|^2 = 0$) and using the orthogonality of Bloch modes we obtain the identities

$$\Psi_L^\dagger V_L^\dagger \Psi_L \Lambda_L^{-1} - \Lambda_L^{*^{-1}} \Psi_L^\dagger V_L \Psi_L = \Lambda_L^* \Psi_L^\dagger V_L^\dagger \Psi_L - \Psi_L^\dagger V_L \Psi_L \Lambda_L = ic\mathbb{I}, \tag{A.20}$$

$$\Psi_R^\dagger V_R^\dagger \Psi_R \Lambda_R^{-1} - \Lambda_R^{*^{-1}} \Psi_R^\dagger V_R \Psi_R = ic\mathbb{I}, \tag{A.21}$$

for the left and right lead respectively. Here c is a constant. We outline the proof below, for the left lead. For the right lead the procedure is identical.

Proof: The Schrödinger equation gives

$$\frac{\partial}{\partial t}\psi_m^{(-n)} = \frac{1}{i\hbar}\left\{V^\dagger \psi_m^{(-n-1)} + H_0 \psi_m^{(-n)} + V\psi_m^{(-n+1)}\right\},$$
$$\frac{\partial}{\partial t}\psi_m^{\dagger(-n)} = \frac{1}{i\hbar}\left\{\psi_m^{\dagger(-n-1)} V + \psi_m^{\dagger(-n)} H_0 + \psi_m^{\dagger(-n+1)} V\right\},$$

where we have used that the Hamiltonian is Hermitian [$H_0^\dagger = H_0$]. The equations above can then be used to find the probability

$$\frac{\partial}{\partial t}|\psi_m^{(-n)}|^2 = \psi_m^{\dagger(-n)}\left(\frac{\partial \psi_m^{(-n)}}{\partial t}\right) + \left(\frac{\partial \psi_m^{\dagger(-n)}}{\partial t}\right)\psi_m^{(-n)}. \tag{A.22}$$

Expanding the terms in parenthesis,

$$\begin{aligned}
\frac{\partial}{\partial t}|\psi_m^{(-n)}|^2 &= \frac{1}{i\hbar}\left\{\psi_m^{\dagger(-n)} V^\dagger \psi_m^{(-n-1)} + \psi_m^{\dagger(-n)} H_0 \psi_m^{(-n)} + \psi_m^{\dagger(-n)} V \psi_m^{(-n+1)}\right. \\
&\quad \left. - \psi_m^{\dagger(-n-1)} V \psi_m^{(-n)} - \psi_m^{\dagger(-n)} H_0 \psi_m^{(-n)} - \psi_m^{\dagger(-n+1)} V^\dagger \psi_m^{(-n)}\right\} \\
&= \frac{1}{i\hbar}\left\{\psi_m^{\dagger(-n)} V^\dagger \psi_m^{(-n-1)} - \left(\psi_m^{\dagger(-n)} V^\dagger \psi_m^{(-n-1)}\right)^\dagger + \left(\psi_m^{\dagger(-n+1)} V^\dagger \psi_m^{(-n)}\right)^\dagger\right. \\
&\quad \left. - \psi_m^{\dagger(-n+1)} V^\dagger \psi_m^{(-n)}\right\} \\
&= \frac{1}{i\hbar}\left\{2i\,\mathrm{Im}\left[\psi_m^{\dagger(-n)} V^\dagger \psi_m^{(-n-1)}\right] - 2i\,\mathrm{Im}\left[\psi_m^{\dagger(-n+1)} V^\dagger \psi_m^{(-n)}\right]\right\} \\
&= \frac{2}{\hbar}\,\mathrm{Im}\left[\psi_m^{\dagger(-n)} V^\dagger \psi_m^{(-n-1)}\right] - \frac{2}{\hbar}\,\mathrm{Im}\left[\psi_m^{\dagger(-n+1)} V^\dagger \psi_m^{(-n)}\right]
\end{aligned}$$

we obtain the continuity equation

$$\frac{\partial}{\partial t}|\psi_m^{(-n)}|^2 = I^{(-n-1,-n)} - I^{(-n,-n+1)}.$$

The probability current is

$$I^{(-n,-n+1)} = \frac{2}{\hbar} \operatorname{Im}\left[\psi_m^{\dagger(-n+1)} V^\dagger \psi_m^{(-n)}\right],$$

and can be obtained from Eq. (A.19) by replacing $n \to -n$.

Using the orthogonality of the Bloch modes, Eq. (A.17), together with the probability conservation, Eq. (A.18), we can flux-normalize all propagating modes without worrying about interferences. Furthermore, the continuity relation guarantees that the flux of evanescent modes and bound states vanishes.

A.2.2 Evaluation of the Scattering Matrix

Analytical calculation

The Hamiltonian and eigenfunction of the entire system are:

$$\mathcal{H}_{\text{tot}} = \begin{pmatrix}
\ddots & \vdots & \vdots & \vdots & \vdots & \vdots & \vdots & \vdots & \vdots & \vdots & \ddots \\
\cdots & H_0 & V_L & 0 & 0 & 0 & 0 & 0 & 0 & 0 & \cdots \\
\cdots & V_L^\dagger & H_0 & V_L & 0 & 0 & 0 & 0 & 0 & 0 & \cdots \\
\cdots & 0 & V_L^\dagger & H_0 & V_L & 0 & 0 & 0 & 0 & 0 & \cdots \\
\cdots & 0 & 0 & V_L^\dagger & H_0 & W_L & 0 & 0 & 0 & 0 & \cdots \\
\cdots & 0 & 0 & 0 & W_L^\dagger & H_S & W_R & 0 & 0 & 0 & \cdots \\
\cdots & 0 & 0 & 0 & 0 & W_R^\dagger & H_0 & V_R & 0 & 0 & \cdots \\
\cdots & 0 & 0 & 0 & 0 & 0 & V_R^\dagger & H_0 & V_R & 0 & \cdots \\
\cdots & 0 & 0 & 0 & 0 & 0 & 0 & V_R^\dagger & H_0 & V_R & \cdots \\
\cdots & 0 & 0 & 0 & 0 & 0 & 0 & 0 & V_R^\dagger & H_0 & \cdots \\
\ddots & \vdots & \vdots & \vdots & \vdots & \vdots & \vdots & \vdots & \vdots & \vdots & \ddots
\end{pmatrix},$$

$$\varphi = \begin{pmatrix} \vdots \\ \Psi_L \Lambda_L^{-n} a_{in} + \tilde{\Psi}_L \tilde{\Lambda}_L^{-n} a_{out} \\ \vdots \\ \Psi_L \Lambda_L^{-1} a_{in} + \tilde{\Psi}_L \tilde{\Lambda}_L^{-1} a_{out} \\ \Psi_L a_{in} + \tilde{\Psi}_L a_{out} \\ \mathcal{X}_S \\ \Psi_R b_{out} + \tilde{\Psi}_R b_{in} \\ \Psi_R \Lambda_R b_{out} + \tilde{\Psi}_R \tilde{\Lambda}_R b_{in} \\ \vdots \\ \Psi_R \Lambda_R^n b_{out} + \tilde{\Psi}_R \tilde{\Lambda}_R^n b_{in} \\ \vdots \end{pmatrix}. \tag{A.23}$$

The leads are identical, with $V_L = V_R$, and would form a continuous nano-ribbon in the absence of the conductor. Here we ave also taken into account that even though $\Psi_R = \Psi_L$, they correspond to right-propagating modes which are outgoing for the right lead but incoming for the left lead. The reverse is applicable to $\tilde{\Psi}_R = \tilde{\Psi}_L$. Then the Scgrödinger equation gives:

• <u>In the Leads</u>

$$\begin{aligned} \text{Left:} \quad & V_L^\dagger(\Psi_L \Lambda_L^{-1} a_{in} + \tilde{\Psi}_L \tilde{\Lambda}_L^{-1} a_{out}) + (H_0 - E)(\Psi_L a_{in} + \tilde{\Psi}_L a_{out}) \\ & + V_L(\Psi_L \Lambda_L a_{in} + \tilde{\Psi}_L \tilde{\Lambda}_L a_{in}) = 0, \\ \text{Right:} \quad & V_R^\dagger(\Psi_R \Lambda_R^{-1} b_{out} + \tilde{\Psi}_R \tilde{\Lambda}_R^{-1} b_{in}) + (H_0 - E)(\Psi_R b_{out} + \tilde{\Psi}_R b_{in}) \\ & + V_R(\Psi_R \Lambda_R b_{out} + \tilde{\Psi}_R \tilde{\Lambda}_R b_{in}) = 0. \end{aligned}$$

• <u>At the contacts</u>

$$\begin{aligned} \text{Left:} \quad & V_L^\dagger(\Psi_L \Lambda_L^{-1} a_{in} + \tilde{\Psi}_L \tilde{\Lambda}_L^{-1} a_{out}) + (H_0 - E)(\Psi_L a_{in} + \tilde{\Psi}_L a_{out}) + W_L \mathcal{X}_S = 0, \\ \text{Right:} \quad & W_R \mathcal{X}_S + (H_0 - E)(\Psi_R b_{out} + \tilde{\Psi}_R b_{in}) + V_R(\Psi_R \Lambda_R b_{out} + \tilde{\Psi}_R \tilde{\Lambda}_R b_{in}) = 0. \end{aligned}$$

Combining the above equations we obtain the continuity conditions at the two

interfaces:

$$\text{Left:} \quad W_L \mathcal{X}_S = V_L(\Psi_L \Lambda_L a_{in} + \tilde{\Psi}_L \tilde{\Lambda}_L a_{in}), \tag{A.24}$$

$$\text{Right:} \quad W_R \mathcal{X}_S = V_R^\dagger(\Psi_R \Lambda_R^{-1} b_{out} + \tilde{\Psi}_R \tilde{\Lambda}_R^{-1} b_{in}). \tag{A.25}$$

• In the conductor

$$\begin{aligned} W_L^\dagger(\Psi_L a_{in} + \tilde{\Psi}_L a_{out}) + (H_S - E)\mathcal{X}_S + W_R(\Psi_R b_{out} + \tilde{\Psi}_R b_{in}) = 0, \\ \Rightarrow (H_S - E)^{-1} W_L^\dagger(\Psi_L a_{in} + \tilde{\Psi}_L a_{out}) + \mathcal{X}_S + (H_S - E)^{-1} W_R(\Psi_R b_{out} + \tilde{\Psi}_R b_{in}) = 0. \end{aligned} \tag{A.26}$$

Multiplying Eq. (A.26) to the left by W_L and $W_R^\dagger$ and using the continuity Eqs. (A.24) and (A.25) we obtain

$$\begin{aligned} & V_L(\Psi_L \Lambda_L a_{in} + \tilde{\Psi}_L \tilde{\Lambda}_L a_{out}) + W_L(H_S - E)^{-1} W_L^\dagger(\Psi_L a_{in} + \tilde{\Psi}_L a_{out}) \\ & + W_L(H_S - E)^{-1} W_R(\Psi_R b_{out} + \tilde{\Psi}_R b_{in}) = 0, \\ & V_R^\dagger(\Psi_R \Lambda_R^{-1} b_{out} + \tilde{\Psi}_R \tilde{\Lambda}_R^{-1} b_{in}) + W_R^\dagger(H_S - E)^{-1} W_L^\dagger(\Psi_L a_{in} + \tilde{\Psi}_L a_{out}) \\ & + W_R^\dagger(H_S - E)^{-1} W_R(\Psi_R b_{out} + \tilde{\Psi}_R b_{in}) = 0. \end{aligned}$$

Grouping the *in* and *out* amplitudes and multiplying the first equation by $\tilde{\Psi}_L^\dagger$ and the second by $\Psi_R^\dagger$ (since Ψ and $\tilde{\Psi}$ are in general rectangular matrices we have to perform this multiplication so that we can invert the resulting matrices) we obtain

a relation between the *in* and *out* amplitudes

$$\begin{pmatrix} \tilde{\Psi}_L^\dagger V_L \tilde{\Psi}_L \tilde{\Lambda}_L - \tilde{\Psi}_L W_L (E - H_S)^{-1} W_L^\dagger \tilde{\Psi}_L & -\Psi_R^\dagger W_R^\dagger (E - H_S)^{-1} W_L^\dagger \tilde{\Psi}_L \\ -\tilde{\Psi}_L^\dagger W_L (E - H_S)^{-1} W_R \Psi_R & \Psi_R^\dagger V_R^\dagger \Psi_R \Lambda_R^{-1} - \Psi_R^\dagger W_R^\dagger (E - H_S)^{-1} W_R \Psi_R \end{pmatrix} \times \begin{pmatrix} a_{out} \\ b_{out} \end{pmatrix} =$$
$$- \begin{pmatrix} \tilde{\Psi}_L^\dagger V_L \Psi_L \Lambda_L - \tilde{\Psi}_L W_L (E - H_S)^{-1} W_L^\dagger \Psi_L & -\Psi_R^\dagger W_R^\dagger (E - H_S)^{-1} W_L^\dagger \Psi_L \\ -\tilde{\Psi}_L^\dagger W_L (E - H_S)^{-1} W_R \tilde{\Psi}_R & \Psi_R^\dagger V_R^\dagger \tilde{\Psi}_R \tilde{\Lambda}_R^{-1} - \Psi_R^\dagger W_R^\dagger (E - H_S)^{-1} W_R \tilde{\Psi}_R \end{pmatrix} \times \begin{pmatrix} a_{in} \\ b_{in} \end{pmatrix}. \tag{A.27}$$

This delivers

$$\left.\begin{pmatrix} a_{out} \\ b_{out} \end{pmatrix}\right|_{pm} = S \left.\begin{pmatrix} a_{in} \\ b_{in} \end{pmatrix}\right|_{pm} \tag{A.28}$$

where *pm* indicates restriction to propagating modes. [Note the restriction to propagating modes must be done after the matrix inversion. This is because even though evanescent modes do not contribute towards transport, they are important in establishing continuity of the waves at the interfaces.] Next we employ the important identities $\tilde{\Psi}_L^\dagger V_L \Psi_L \Lambda_L = \tilde{\Lambda}^* \tilde{\Psi}_L^\dagger V_L^\dagger \Psi_L$ and $\Psi_R^\dagger V_R^\dagger \tilde{\Psi}_R \tilde{\Lambda}_R^{-1} = \Lambda_R^{*-1} \Psi_R^\dagger V_R \tilde{\Psi}_R$

and obtain the scattering matrix

$$S=-\begin{pmatrix} \tilde{\Psi}_L^\dagger V_L \tilde{\Psi}_L \tilde{\Lambda}_L - \tilde{\Psi}_L W_L (E-H_S)^{-1} W_L^\dagger \tilde{\Psi}_L & -\tilde{\Psi}_L^\dagger W_L (E-H_S)^{-1} W_R \Psi_R \\ -\Psi_R^\dagger W_R^\dagger (E-H_S)^{-1} W_L^\dagger \tilde{\Psi}_L & \Psi_R^\dagger V_R^\dagger \Psi_R \Lambda_R^{-1} - \Psi_R^\dagger W_R^\dagger (E-H_S)^{-1} W_R \Psi_R \end{pmatrix}^{-1}$$
$$\times \begin{pmatrix} \tilde{\Lambda}_L^* \tilde{\Psi}_L^\dagger V_L^\dagger \Psi_L - \tilde{\Psi}_L W_L (E-H_S)^{-1} W_L^\dagger \Psi_L & -\tilde{\Psi}_L^\dagger W_L (E-H_S)^{-1} W_R \tilde{\Psi}_R \\ -\Psi_R^\dagger W_R^\dagger (E-H_S)^{-1} W_L^\dagger \Psi_L & \Lambda_R^{*^{-1}} \Psi_R^\dagger V_R \tilde{\Psi}_R - \Psi_R^\dagger W_R^\dagger (E-H_S)^{-1} W_R \tilde{\Psi}_R \end{pmatrix} \Bigg|_{pm} . \tag{A.29}$$

Eliminating the conductor (which is equivalent to setting $WL = WR = 0$) the system will be comprised of two decoupled semi-infinite leads. The hard wall boundary conditions at the finite edges ensure only elastic scattering occurs in each lead. Because of that the scattering matrix must be unitary to ensure conservation of probability:

Proof:

$$\left.\begin{aligned} a_{out} &= S a_{in} \\ |a_{out}|^2 &= |a_{in}|^2 \end{aligned}\right\} \Rightarrow \quad a_{out}^\dagger a_{out} = a_{in}^\dagger a_{in}$$
$$(a_{in}^\dagger S^\dagger)(S a_{in}) = a_{in}^\dagger a_{in}$$
$$a_{in}^\dagger (S^\dagger S) a_{in} = a_{in}^\dagger a_{in}$$
$$\Rightarrow S^\dagger S = \mathbb{I}.$$

Furthermore, unitarity of the scattering matrix for $W_L = W_R = 0$ guarantees that $\Psi_L|_{pm} = \tilde{\Psi}_L\Big|_{pm} U_L$ and $\tilde{\Psi}_R\Big|_{pm} = \Psi_R|_{pm} U_R$, where U_L and U_R are unitary matrices.

Proof: If $W_L = W_R = 0$ then the S matrix is

$$S = -\underbrace{\begin{pmatrix} \tilde{\Psi}_L^\dagger V_L \tilde{\Psi}_L \tilde{\Lambda}_L & 0 \\ 0 & \Psi_R^\dagger V_R^\dagger \Psi_R \Lambda_R^{-1} \end{pmatrix}^{-1}}_{P=\begin{pmatrix} p_L & 0 \\ 0 & p_R \end{pmatrix}} \times \underbrace{\begin{pmatrix} \tilde{\Lambda}^* \tilde{\Psi}_L^\dagger V_L^\dagger \Psi_L & 0 \\ 0 & \Lambda_R^{*^{-1}} \Psi_R^\dagger V_R \tilde{\Psi}_R \end{pmatrix}}_{Q=\begin{pmatrix} q_L & 0 \\ 0 & q_R \end{pmatrix}} \Bigg|_{pm}.$$

Denoting the two matrices with P and Q then $S = -P^{-1}Q$, $S^\dagger = -Q^\dagger (P^{-1})^\dagger$, $S^{-1} = -Q^{-1}P$ and we must show that $S^{-1} = S^\dagger$:

$$S^{-1} = S^\dagger \Rightarrow QQ^\dagger = PP^\dagger \Rightarrow \begin{pmatrix} q_L q_L^\dagger & 0 \\ 0 & q_R q_R^\dagger \end{pmatrix} = \begin{pmatrix} p_L p_L^\dagger & 0 \\ 0 & p_R p_R^\dagger \end{pmatrix}.$$

However, from the current conservation we know that

$$q_L^\dagger - q_L = ic\mathbb{I} \Rightarrow \underbrace{\begin{cases} q_l^\dagger q_L^\dagger - q_L q_L^\dagger = icq_L^\dagger \\ q_l^\dagger q_L^\dagger - q_L^\dagger q_L = icq_L^\dagger \end{cases}}_{q_L^\dagger q_L = q_L q_L^\dagger}$$

$$\Rightarrow \tilde{\Lambda}_L^* \tilde{\Psi}_L V_L^\dagger \tilde{\Psi}_L \tilde{\Psi}_L^\dagger V_L \tilde{\Psi}_L = \tilde{\Lambda}_L^* \tilde{\Psi}_L V_L^\dagger \Psi_L \Psi_L^\dagger V_L \tilde{\Psi}_L. \qquad \text{(A.30)}$$

This means $\tilde{\Psi}_L \tilde{\Psi}_L^\dagger = \Psi_L \Psi_L^\dagger$, which is only true if $\Psi_L = \tilde{\Psi}_L U_L$ and U_L is a unitary matrix that can be absorbed into the definition of incoming modes. Applying the

same procedure to the right lead we find that $\tilde{\Psi}_R = \Psi_R U_R$. Then the S matrix is

$$S = -\begin{pmatrix} \tilde{\Psi}_L^\dagger V_L \tilde{\Psi}_L \tilde{\Lambda}_L - \tilde{\Psi}_L W_L (E - H_S)^{-1} W_L^\dagger \tilde{\Psi}_L & -\tilde{\Psi}_L^\dagger W_L (E - H_S)^{-1} W_R \Psi_R \\ -\Psi_R^\dagger W_R^\dagger (E - H_S)^{-1} W_L^\dagger \tilde{\Psi}_L & \Psi_R^\dagger V_R^\dagger \Psi_R \Lambda_R^{-1} - \Psi_R^\dagger W_R^\dagger (E - H_S)^{-1} W_R \Psi_R \end{pmatrix}^{-1}$$
$$\times \begin{pmatrix} \tilde{\Lambda}_L^* \tilde{\Psi}_L^\dagger V_L^\dagger \tilde{\Psi}_L - \tilde{\Psi}_L W_L (E - H_S)^{-1} W_L^\dagger \tilde{\Psi}_L & -\tilde{\Psi}_L^\dagger W_L (E - H_S)^{-1} W_R \Psi_R \\ -\Psi_R^\dagger W_R^\dagger (E - H_S)^{-1} W_L^\dagger \tilde{\Psi}_L & \Lambda_R^{*-1} \Psi_R^\dagger V_R \Psi_R - \Psi_R^\dagger W_R^\dagger (E - H_S)^{-1} W_R \Psi_R \end{pmatrix} \Bigg|_{pm} \tag{A.31}$$

$$= -\mathbb{I} + \begin{pmatrix} \tilde{\Psi}_L^\dagger V_L \tilde{\Psi}_L \tilde{\Lambda}_L - \tilde{\Psi}_L W_L (E - H_S)^{-1} W_L^\dagger \tilde{\Psi}_L & -\tilde{\Psi}_L^\dagger W_L (E - H_S)^{-1} W_R \Psi_R \\ -\Psi_R^\dagger W_R^\dagger (E - H_S)^{-1} W_L^\dagger \tilde{\Psi}_L & \Psi_R^\dagger V_R^\dagger \Psi_R \Lambda_R^{-1} - \Psi_R^\dagger W_R^\dagger (E - H_S)^{-1} W_R \Psi_R \end{pmatrix}^{-1}$$
$$\times \begin{pmatrix} \tilde{\Psi}_L^\dagger V_L \tilde{\Psi}_L \tilde{\Lambda}_L - \tilde{\Lambda}_L^* \tilde{\Psi}_L^\dagger V_L^\dagger \tilde{\Psi}_L & 0 \\ 0 & \Psi_R^\dagger V_R^\dagger \Psi_R \Lambda_R^{-1} - \Lambda_R^{*-1} \Psi_R^\dagger V_R \Psi_R \end{pmatrix} \Bigg|_{pm} . \tag{A.32}$$

Using the orthogonality of Bloch modes and current conservation, one can prove the S matrix is indeed unitary.

Proof of unitarity: Let us write the S matrix in Eq. (A.31) as

$$S = -\begin{pmatrix} p_L - q_{LL} & -q_{LR} \\ -q_{RL} & p_R - q_{RR} \end{pmatrix}^{-1} \times \begin{pmatrix} p_L^\dagger - q_{LL} & -q_{LR} \\ -qRL & p_R^\dagger - q_{RR} \end{pmatrix},$$
$$= K^{-1} K^\dagger,$$

where $q_{LL}^\dagger = q_{LL}$, $q_{RR}^\dagger = q_{RR}$, $q_{LR}^\dagger = q_{RL}$, and $q_{RL}^\dagger = q_{LR}$. We will also use $p_L p_L^\dagger = p_L^\dagger p_L$ and $p_R p_R^\dagger = p_R^\dagger p_R$ which we have shown using flux-normalization in Eq. (A.30). Next, we must show that $S^\dagger = S^{-1} \Rightarrow K(K^{-1})^\dagger = (K^\dagger)^{-1} K \Rightarrow$

$K^\dagger K = KK^\dagger$. This implies that

$$K^\dagger K = \begin{pmatrix} (p_L^\dagger - q_{LL})(p_L - q_{LL}) + q_{LR}q_{RL} & -(p_L^\dagger - q_{LL})q_{LR} - q_{LR}(p_R - q_{RR}) \\ -q_{RL}(p_L - q_{LL}) - (p_R^\dagger - q_{RR})q_{RL} & q_{RL}q_{LR} + (p_R^\dagger - q_{RR})(p_R - q_R R) \end{pmatrix}$$

$$= \begin{pmatrix} (p_L - q_{LL})(p_L^\dagger - q_{LL}) + q_{LR}q_{RL} & -(p_L - q_{LL})q_{LR} - q_{LR}(p_R^\dagger - q_{RR}) \\ -q_{RL}(p_L^\dagger - q_{LL}) - (p_R - q_{RR})q_{RL} & q_{RL}q_{LR} + (p_R - q_{RR})(p_R^\dagger - q_R R) \end{pmatrix}$$

$$= KK^\dagger. \tag{A.33}$$

1°.

$$(p_L^\dagger - q_{LL})(p_L - q_{LL}) + q_{LR}q_{RL} = (p_L - q_{LL})(p_L^\dagger - q_{LL}) + q_{LR}q_{RL}$$

$$-p_L^\dagger q_{LL} - q_{LL}p_L = -p_L q_{LL} - q_{LL}p_L^\dagger$$

$$(p_L - p_L^\dagger)q_{LL} = q_{LL}(p_L - p_L^\dagger)$$

$$(ic)q_{LL} = q_{LL}(ic) \quad \checkmark$$

2°.

$$-q_{RL}(p_L - q_{LL}) - (p_R^\dagger - q_{RR})q_{RL} = -q_{RL}(p_L^\dagger - q_{LL}) - (p_R - q_{RR})q_{RL}$$

$$-q_{RL}p_L - p_R^\dagger q_{RL} = -q_{RL}p_L^\dagger - p_R q_{RL}$$

$$(p_R - p_R^\dagger)q_{RL} = q_{RL}(p_R - p_R^\dagger)$$

$$(ic\mathbb{I})q_{RL} = q_{RL}(ic\mathbb{I}) \quad \checkmark$$

3°.

$$-(p_L^\dagger - q_{LL})q_{LR} - q_{LR}(p_R - q_{RR}) = -(p_L - q_{LL})q_{LR} - q_{LR}(p_R^\dagger - q_{RR})$$

$$-p_L^\dagger q_{LR} - q_{LR}p_R = -p_L q_{LR}p_R^\dagger$$

$$(p_L - p_L^\dagger)q_{LR} = q_{LR}(p_L - p_L^\dagger)$$

$$(ic\mathbb{I})q_{LR} = q_{LR}(ic\mathbb{I}) \quad \checkmark$$

4°.

$$q_{RL}q_{LR} + (p_R^\dagger - q_{RR})(p_R - q_{RR}) = q_{RL}q_{LR} + (p_R - q_R R)(q_P^\dagger - q_R R)$$
$$-p_R^\dagger q_{RR} - q_{RR}p_R = -p_R q_{RR} - q_{RR}p_R^\dagger$$
$$(p_R - p_R^\dagger)q_{RR} = q_{RR}(p_R - p_R^\dagger) \quad \checkmark$$

Therefore the S matrix in the form of both Eq. (A.31) and Eq. (A.32) is indeed unitary.

Numerical calculation

Before performing numerical calculations, we can simplify the above S matrix to make it more transparent. Let $q_L^{-1} = \tilde{\Psi}_L^\dagger V_L \tilde{\Psi}_L \tilde{\Lambda}_L$ and $q_R^{-1} = \Psi_R^\dagger V_R^\dagger \Psi_R \Lambda_R^{-1}$. Then

$$\begin{aligned}
S =& -\mathbb{I} + \left[\begin{pmatrix} q_L^{-1} & 0 \\ 0 & q_R^{-1} \end{pmatrix} - \begin{pmatrix} \tilde{\Psi}_L W_L (E - H_S)^{-1} W_L^\dagger \tilde{\Psi}_L & \tilde{\Psi}_L^\dagger W_L (E - H_S)^{-1} W_R \Psi_R \\ \Psi_R^\dagger W_R^\dagger (E - H_S)^{-1} W_L^\dagger \tilde{\Psi}_L & \Psi_R^\dagger W_R^\dagger (E - H_S)^{-1} W_R \Psi_R \end{pmatrix} \right]^{-1} \\
& \times \begin{pmatrix} q_L^{-1} - (q_L^\dagger)^{-1} & 0 \\ 0 & q_R^{-1} - (q_R^\dagger)^{-1} \end{pmatrix} \Bigg|_{pm}, \\
=& -\mathbb{I} + \left[\begin{pmatrix} q_L^{-1} & 0 \\ 0 & q_R^{-1} \end{pmatrix} - \begin{pmatrix} \tilde{\Psi}_L^\dagger W_L \\ \Psi_R^\dagger W_R^\dagger \end{pmatrix} (E - H_S)^{-1} \begin{pmatrix} \tilde{\Psi}_L^\dagger W_L \\ \Psi_R^\dagger W_R^\dagger \end{pmatrix}^\dagger \right]^{-1} \\
& \times \begin{pmatrix} q_L^{-1} - (q_L^\dagger)^{-1} & 0 \\ 0 & q_R - (q_R^\dagger)^{-1} \end{pmatrix} \Bigg|_{pm}, \\
=& -\mathbb{I} + \left[q^{-1} - V(E - H_S)^{-1} V^\dagger \right]^{-1} \left(q - q^\dagger \right)^{-1} \Big|_{pm}, \\
=& -\mathbb{I} + \left[q + qV(E - H_S - V^\dagger q V)^{-1} V^\dagger q \right] \left(q - q^\dagger \right)^{-1} \Big|_{pm},
\end{aligned} \tag{A.34}$$

where we have used the substitution $q = \left(\begin{smallmatrix} q_L & 0 \\ 0 & q_R \end{smallmatrix}\right)$ and $V = \left(\begin{smallmatrix} \tilde{\Psi}_L^\dagger W_L \\ \Psi_R^\dagger W_R^\dagger \end{smallmatrix}\right)$. Note that both matrices q and V are invertible even though the matrices $\tilde{\Psi}_L$ and Ψ_R are not quadratic but rectangular.

This S matrix gives the amplitudes of the modes between the two leads. The Green's function term $G = (E - H_S - V^\dagger q V)^{-1}$ describes the propagation of

electrons between two points within the conductor, while taking into account the effect of the leads through the term $\Sigma = V^{\dagger}qV$ [28]. This is the so called self energy of the leads, and can be understood as an effective Hamiltonian describing the interaction between the leads and the scatterer.

A.3 Transport properties

The purpose of these calculations is to find and use an effective method of studying transport properties of a two-terminal graphitic device, with detailed properties described above. At low bias (when the phase coherence length is larger than the system size), the phase-coherent properties of a two terminal mesoscopic device are encoded in the scattering matrix[7, 12]

$$S = \begin{pmatrix} r & t' \\ t & r' \end{pmatrix}, \tag{A.35}$$

where t, t', r, and r' are transmission and reflection amplitudes of charge carriers that originate in the source or drain leads respectively. To characterize transport properties we start by finding this S matrix from which the transmission matrix (containing the transmission amplitudes of the waves traveling from source to drain leads or *vice versa*) can be extracted. Further, the Landauer conductance or shot-noise Fano factor[108] can be found directly from the above equation as

$$G(E) = \frac{2e^2}{h} Tr(t^{\dagger}t), \quad F(E) = 1 - \frac{Tr(t^{\dagger}tt^{\dagger}t)}{Tr(t^{\dagger}t)}. \tag{A.36}$$

Based on the above results for the transmission probability, in Chapter 2 we employ the Landauer-Büttiker formalism [18] to calculate the conductance of an *n-p-n* junction. Taking into account two valleys, as well as integrating over the electron energy (as determined by the Fermi distribution with finite temperature

T), we arrive at the junction conductance,

$$G(\mu, T) = \frac{2e^2}{h} \int_{-\infty}^{\infty} d\epsilon \frac{1}{4k_B T} \frac{1}{\cosh^2\left(\frac{E-\mu}{2k_B T}\right)} \sum_n |t_n|^2.$$

Here, k_B is the Boltzmann constant, and $\sum_n |t_n|^2 = Tr(t^\dagger t)$ is the transmission over all modes at fixed energy. By performing the integration numerically, we obtain the conductance as a function of chemical potential and temperature.

Appendix B

Microscopic model

B.1 Introduction

In the following we will describe the mechanism used to derive the Hamiltonian for a monolayer graphene flake subject to a hBN substrate. Here we use a microscopic model that is compatible with the symmetries of the system [123] and model the hBN substrate as a lattice of positively charged nitrogen nuclei in a homogeneous background of electron P^z orbitals. These results are used in Chapter 4.

B.2 Dirac Hamiltonian

We start with the Dirac Hamiltonian

$$\hat{H} = v\boldsymbol{p} \cdot \boldsymbol{\sigma}\tau_0 + \delta\hat{H} \tag{B.1}$$

which is perturbed with $\delta\hat{H}$ by the hBN substrate. Here $\boldsymbol{p} = -i\nabla$ is the momentum relative to one of the corners of the moiré Brillouin zone (BZ), and $\boldsymbol{\sigma}$ is the vector of Pauli matrices. Here we have used the direct products $\sigma_i\tau_j$ of Pauli matrices where σ_i and τ_j act on the sublattice and valley indices respectively. The

eigenfunctions of the Hamiltonian are

$$\Psi_{K\zeta+\boldsymbol{k}}(\boldsymbol{r}) = \begin{pmatrix} \psi^A_{K\zeta+\boldsymbol{k}}(\boldsymbol{r}) \\ \psi^B_{K\zeta+\boldsymbol{k}}(\boldsymbol{r}) \\ \psi^B_{K\zeta+\boldsymbol{k}}(\boldsymbol{r}) \\ \psi^A_{K\zeta+\boldsymbol{k}}(\boldsymbol{r}) \end{pmatrix} = \frac{1}{\sqrt{2}L} \begin{pmatrix} \delta_{\zeta,1} \\ s\delta_{\zeta,1}e^{i\theta_{\boldsymbol{k}}} \\ \delta_{\zeta,-1} \\ s\delta_{\zeta,-1}e^{i\theta_{\boldsymbol{k}}} \end{pmatrix} e^{i\boldsymbol{k}\cdot\boldsymbol{r}} \tag{B.2}$$

where $K_\pm$ denote the two valleys, $\boldsymbol{k}$ is a small step in the momentum space, L is the length of the system used for normalization, $s = \pm 1$ for the conduction or the valence bands, and $\theta_{\boldsymbol{k}}$ is the direction angle for $\boldsymbol{k}$. $\Phi^A_{K\zeta}$ is the envelope function at valley $K\zeta$.

B.3 Bloch wave functions

The Bloch wave functions with the k.p approximation[2] are

$$\begin{aligned} \Phi_{I,K\zeta+\boldsymbol{k}} &= \frac{1}{\sqrt{N}} \sum_{\boldsymbol{R_0}} e^{i(K+\boldsymbol{k})\cdot(\boldsymbol{R_0}+\tau_I)} \varphi_z(\boldsymbol{r} - \boldsymbol{R_0} - \tau_I) \\ &\simeq \frac{1}{\sqrt{N}} e^{i\boldsymbol{k}\cdot\boldsymbol{r}} \sum_{\boldsymbol{R_0}} e^{iK\cdot(\boldsymbol{R_0}+\tau_I)} \varphi_z(\boldsymbol{r} - \boldsymbol{R_0} - \tau_I). \end{aligned} \tag{B.3}$$

Here N is the number of unit cells, the vector $\boldsymbol{R} = \boldsymbol{R_0} - \tau_I$ represents the position of the atom where $\boldsymbol{R_0} = n_1 t_1 + n_2 t_2$ is the translation vector of the origin of the system and τ_I with $I = A$, B is the vector from the center of the hexagon to the A or B sites. Note that Ψ is determined by the atomic wave function in the φ atomic orbital, which brings in the z dependence. Then we can see that in real space the Dirac eigenfunctions (the electronic states) are written as a product between Bloch functions and the envelope functions:

$$\Psi_{K\zeta+\boldsymbol{k}}(\boldsymbol{r}, z) = L\psi^A_{K\zeta+\boldsymbol{k}}(\boldsymbol{r})\Phi_{A,K\zeta}(\boldsymbol{r}, z) + L\psi^B_{K\zeta+\boldsymbol{k}}(\boldsymbol{r})\Phi_{B,K\zeta}(\boldsymbol{r}, z). \tag{B.4}$$

The electronic states in the $K_\pm$ valleys do not interact (no intervalley scattering takes place) however in the case where interactions do occur, the summation of

the two must considered in both valleys. The length L must be included to ensure the proper normalization $\langle \Psi_{K\zeta+\boldsymbol{k}} | \Psi_{K\zeta+\boldsymbol{k}} \rangle = 1$. In the above analysis we have assumed that $\psi^I_{\boldsymbol{k}}(\boldsymbol{r})$ varies slowly over the unit cell, but $\Phi_{I,K\zeta}(\boldsymbol{r}, z)$ varies rapidly and is periodic over the unit cell. Using Fourier transformations, the Bloch wave functions can be written as

$$\Phi_{I,\boldsymbol{k}} = \frac{2\pi}{A_g\sqrt{N}} \sum_{\boldsymbol{g}} \tilde{\Psi}_z(\boldsymbol{k}-\boldsymbol{g}) e^{i\boldsymbol{k}\cdot\tau_I} e^{i(\boldsymbol{k}-\boldsymbol{g})\cdot(\boldsymbol{r}-\tau_I)}, \tag{B.5}$$

where A_g is the area of the unit cell of graphene, and $\tilde{\Psi}_z(\boldsymbol{k}-\boldsymbol{g})$ is the in-plane Fourier transform of the P^z orbital.

B.4 Perturbation Hamiltonian

The potential from the hBN substrate is

$$u(\boldsymbol{r}, z) = \sum_{\boldsymbol{R}_s} V(\boldsymbol{r}-\boldsymbol{R}_s, z) = \frac{2\pi}{A_s} \sum_{\boldsymbol{g}_s} \tilde{V}(\boldsymbol{g}_s, z) e^{i\boldsymbol{g}_s\cdot\boldsymbol{r}}, \tag{B.6}$$

where $\boldsymbol{R}_s$ are vectors to the center of the hexagons in the lattice of hBN, A_s is the area of the unit cell of the substrate and $\boldsymbol{g}_s = m_1\mathbf{b}_{1s} + m_2\mathbf{b}_{2s}$ are the reciprocal lattice vectors of the substrate. Then the matrix elements can be written as

$$\begin{aligned} \langle \Psi_{K\zeta+\boldsymbol{k1}} | u(\boldsymbol{r}, z) | \Psi_{K\zeta+\boldsymbol{k2}} \rangle &= L^2 \int \Psi^\dagger_{K\zeta+\boldsymbol{k1}}(\boldsymbol{r}, z) u(\boldsymbol{r}, z) \Psi_{K\zeta+\boldsymbol{k2}}(\boldsymbol{r}, z) dr dz \\ &= \int e^{i(\boldsymbol{k2}-\boldsymbol{k1})\cdot\boldsymbol{r}} \bar{\Psi}^\dagger_{K\zeta+\boldsymbol{k1}} \delta\bar{H} \bar{\Psi}_{K\zeta+\boldsymbol{k2}} dr \end{aligned} \tag{B.7}$$

where

$$\bar{\Psi}_{K\zeta+\boldsymbol{k}} = \begin{pmatrix} \Psi^A_{K\zeta+\boldsymbol{k}} \\ \Psi^B_{K\zeta+\boldsymbol{k}} \end{pmatrix}, \quad \delta\bar{H} = \begin{pmatrix} \delta\hat{H}_{AA} & \delta\hat{H}_{AB} \\ \delta\hat{H}_{BA} & \delta\hat{H}_{BB} \end{pmatrix},$$

$$\delta\hat{H}_{ij} = L^2 \int \Phi^*_{i,\boldsymbol{K}\zeta}(\boldsymbol{r},z)u(\boldsymbol{r},z)\Phi_{j,\boldsymbol{K}\zeta}(\boldsymbol{r},z)dz, \quad i,j = A \text{ or } B. \tag{B.8}$$

Evaluating the terms in Eq. (B.8) we obtain the perturbation Hamiltonian,

$$\begin{aligned}\delta\hat{H}_{ij} &= \frac{(2\pi)^3}{A_g^2 As}\frac{L^2}{N}\sum_{\boldsymbol{g},\boldsymbol{g}',\boldsymbol{g}_s} e^{(\boldsymbol{g}_s-\boldsymbol{g}+\boldsymbol{g}')\cdot\boldsymbol{r}} e^{i(\boldsymbol{g}\cdot\tau_i-\boldsymbol{g}'\cdot\tau_j)} \int dz\tilde{\varphi}^*_z(\boldsymbol{K}+\boldsymbol{g})\tilde{u}(\boldsymbol{g}_s,z)\tilde{\varphi}_z(\boldsymbol{K}+\boldsymbol{g}'), \\ &= \frac{(2\pi)^3}{A_g^2 As}\frac{L^2}{N} I \sum_{\substack{\boldsymbol{Q},\boldsymbol{Q}' \in \boldsymbol{K}_1,\boldsymbol{K}_2,\boldsymbol{K}_3 \\ \boldsymbol{g}_s = \boldsymbol{g}_s | i = 1\cdots 5}} e^{i(-\boldsymbol{Q}+\boldsymbol{Q}'+\boldsymbol{g}_s)\cdot\boldsymbol{r}} e^{i\boldsymbol{Q}\cdot\tau_i} e^{-i\boldsymbol{Q}'\cdot\tau_j}\end{aligned} \tag{B.9}$$

where $\tilde{\varphi}_z$ is the in-plane Fourier transform of the P^z orbital, $\tilde{u}$ is the Fourier transform of the potential perturbation due to the substrate. In the second line we made the substitutions $\boldsymbol{Q} = \boldsymbol{K}_1 + \boldsymbol{g}$ and $\boldsymbol{Q}' = \boldsymbol{K}_1 + \boldsymbol{g}'$ where $\boldsymbol{K}_1$, $\boldsymbol{K}_2$ and $\boldsymbol{K}_3$ are the corners of the graphene BZ. [Also note that $\boldsymbol{g} \Rightarrow \boldsymbol{g} + \boldsymbol{K}_1$.] In the above equation, $\boldsymbol{b}_m = -\boldsymbol{Q} + \boldsymbol{Q}' + \boldsymbol{g}_s$ are the moiré reciprocal lattice vectors which we will be using from now on.

We assume that the integral is a rapidly decaying function of its arguments $\boldsymbol{g}$, $\boldsymbol{g}'$, $\boldsymbol{g}_s$, which allow us to truncate the summation. In particular $\boldsymbol{g}_s$ is restricted to the first set of vectors, and $\boldsymbol{g}$, $\boldsymbol{g}'$ must take values to maintain $\boldsymbol{K}+\boldsymbol{g}$ and $\boldsymbol{K}+\boldsymbol{g}'$ within the first BZ (the conditions fix $\boldsymbol{g}$, $\boldsymbol{g}'$ for a particular value of $\boldsymbol{g}_s$). Upon evaluation of the integral one finds that is one of the arguments increases, the function will decay rapidly.

Performing the calculations we obtain the following Hamiltonian written in

terms of the Pauli matrices

$$\delta\hat{H} = \begin{pmatrix} \delta\hat{H}_{AA} & \delta\hat{H}_{AB} \\ \delta\hat{H}_{BA} & \delta\hat{H}_{BB} \end{pmatrix} = \left(\frac{\delta\hat{H}_{AA} + \delta\hat{H}_{BB}}{2}\right)\mathbb{I} + \left(\frac{\delta\hat{H}_{AB} + \delta\hat{H}_{BA}}{2}\right)\sigma_x + i\left(\frac{\delta\hat{H}_{AB} - \delta\hat{H}_{BA}}{2}\right)\sigma_y + \left(\frac{\delta\hat{H}_{AA} - \delta\hat{H}_{BB}}{2}\right)\sigma_z. \tag{B.10}$$

Using the moiré reciprocal lattice vectors

$$\boldsymbol{b}_m = \left(\frac{\delta}{(1+\delta)}\right)\hat{R}_{\frac{2\pi m}{6}}\left(0, \frac{4\pi}{3a}\right), \tag{B.11}$$

and grouping the terms we obtain

$$\delta\hat{H} = \frac{(2\pi)^3}{A_g^2 A_s}\frac{L^2}{N} I\left[-\frac{1}{2}f_1(\boldsymbol{r})\mathbb{I} + \frac{\sqrt{3}}{2}f_2(\boldsymbol{r})\sigma_z + \frac{1}{|\boldsymbol{b}_m|}[\hat{\boldsymbol{l}}_z \times \nabla f_2(\boldsymbol{r})]\cdot\boldsymbol{\sigma}\right]. \tag{B.12}$$

In the above equation the term with $f_1(\boldsymbol{r}) = \sum_{m=0..5} e^{i\boldsymbol{b}_m(w,\theta)\cdot\boldsymbol{r}}$ describes a simple potential modulation. The second term, with $f_2(\boldsymbol{r}) = i\sum_{m=0..5}(-1)^m e^{i\boldsymbol{b}_m(w,\theta)\cdot\boldsymbol{r}}$, accounts for the $A-B$ sublattice asymmetry locally imposed by the substrate, and finally, the last term with $\hat{\boldsymbol{l}}_z$ describes the influence of the substrate on the $A-B$ hopping and can be interpreted as a pseudomagnetic field which has opposite signs in the two valleys $\boldsymbol{K}$ and $\boldsymbol{K}'$.

In the above derivation we have only accounted for the lattice mismatch between the graphene flake and the hBN substrate and therefore assumed the misalignment angle $\theta = 0$. The derivation up to Eq. (B.10) is general and can be used to consider more complicated scenarios, however, the reciprocal lattices vectors in Eq. (B.11) and implicitly Eq. (B.12) will change depending on the number of free parameters in the system (e.g. a missalignment angle, strength of mechanical deformations, or orientation of applied strain). Such a scenario is discussed in Chapter 4.

Bibliography

[1] A. A. Abrikosov. *Fundamentals of the theory of metals.* Elsevier Science Pub. Co. Inc. New York, NY, 1988.

[2] T. Ando. Theory of electronic states and transport in carbon nanotubes. *Journal of the Physical Society of Japan*, 74:777, 2005.

[3] D. A. Areshkin, D. Gunlycke, and C. T. White. Ballistic transport in graphene nanostrips in the presence of disorder: Importance of edge effects. *Nano Letters*, 7:204, 2007.

[4] M. Barbier, P. Vasilopoulos, and F. M. Peeters. Extra Dirac points in the energy spectrum for superlattices on single-layer graphene. *Phys. Rev. B*, 81:075438, 2010.

[5] M. Barbier, P. Vasilopoulos, and F. M. Peeters. Kronig-penney model on bilayer graphene: Spectrum and transmission periodic in the strength of the barriers. *Phys. Rev. B*, 82:235408, 2010.

[6] M. Barbier, P. Vasilopoulos, and F. M. Peeters. Single-layer and bilayer graphene superlattices: collimation, additional Dirac points and dirac lines. *Philosophical Transactions of the Royal Society A: Mathematical, Physical and Engineering Sciences*, 368:5499, 2010.

[7] C. W. J. Beenakker. Random-matrix theory of quantum transport. *Rev. Mod. Phys.*, 69:731, 1997.

[8] J. D. Bernal. The structure of graphite. *Proceedings of the Royal Society of London. Series A, Containing Papers of a Mathematical and Physical Character*, 106:749, 1924.

[9] G. L. Bir, G. E. Pikus, P. Shelnitz, and D. Louvish. *Symmetry and strain-induced effects in semiconductors*, volume 624. Wiley New York, 1974.

[10] R. Bistritzer and A. H. MacDonald. Transport between twisted graphene layers. *Phys. Rev. B*, 81:245412, 2010.

[11] O. L. Blakslee, D. G. Proctor, E. J. Seldin, G. B. Spence, and T. Weng. Elastic constants of compression-annealed pyrolytic graphite. *Journal of Applied Physics*, 41:3373, 1970.

[12] Y. M. Blanter and M. Büttiker. Shot noise in mesoscopic conductors. *Physics Reports*, 336:1, 2000.

[13] Y. P. Bliokh, V. Freilikher, S. Savel'ev, and F. Nori. Transport and localization in periodic and disordered graphene superlattices. *Phys. Rev. B*, 79:075123, 2009.

[14] T. J. Booth, P. Blake, R. R. Nair, D. Jiang, E. W. Hill, U. Bangert, A. Bleloch, M. Gass, K. S. Novoselov, and M. I. Katsnelson. Macroscopic graphene membranes and their extraordinary stiffness. *Nano letters*, 8:2442, 2008.

[15] M. S. Bresnehan, M. J. Hollander, M. Wetherington, M. LaBella, K. A. Trumbull, R. Cavalero, D. W. Snyder, and J. A. Robinson. Integration of hexagonal boron nitride with quasi-freestanding epitaxial graphene: Toward wafer-scale, high-performance devices. *ACS nano*, 6:5234, 2012.

[16] L. Brey and H. A. Fertig. Electronic states of graphene nanoribbons studied with the Dirac equation. *Phys. Rev. B*, 73:235411, 2006.

[17] J. S. Bunch, S. S. Verbridge, J. S. Alden, A. M. van der Zande, J. M. Parpia, H. G. Craighead, and P. L. McEuen. Impermeable atomic membranes from graphene sheets. *Nano letters*, 8:2458, 2008.

[18] M. Büttiker. Four-terminal phase-coherent conductance. *Phys. Rev. Lett.*, 57:1761, 1986.

[19] L. C. Campos, V. R. Manfrinato, J. D. Sanchez-Yamagishi, J. Kong, and P. Jarillo-Herrero. Anisotropic etching and nanoribbon formation in single-layer graphene. *Nano letters*, 9:260, 2009.

[20] E. V. Castro, K. S. Novoselov, S. V. Morozov, N. M. R. Peres, J. M. B. L. dos Santos, J. Nilsson, F. Guinea, A. K. Geim, and A. H. C. Neto. Biased bilayer graphene: Semiconductor with a gap tunable by the electric field effect. *Phys. Rev. Lett.*, 99:216802, 2007.

[21] E. V. Castro, H. Ochoa, M. I. Katsnelson, R. V. Gorbachev, D. C. Elias, K. S. Novoselov, A. K. Geim, and F. Guinea. Limits on charge carrier mobility in suspended graphene due to flexural phonons. *Phys. Rev. Lett.*, 105:266601, 2010.

[22] A. H. Castro Neto, F. Guinea, N. M. R. Peres, K. S. Novoselov, and A. K. Geim. The electronic properties of graphene. *Rev. Mod. Phys.*, 81:109, 2009.

[23] A. H. Castro Neto, F. Guinea, N. M. R. Peres, K. S. Novoselov, and A. K. Geim. The electronic properties of graphene. *Rev. Mod. Phys.*, 81:109, 2009.

[24] E. Cerda and L. Mahadevan. Geometry and physics of wrinkling. *Phys. Rev. Lett.*, 90:074302, 2003.

[25] V. V. Cheianov and V. I. Fal'ko. Selective transmission of Dirac electrons and ballistic magnetoresistance of n-p junctions in graphene. *Phys. Rev. B*, 74:041403, 2006.

[26] V. V. Cheianov, V. I. Fal'ko, and B. L. Altshuler. The focusing of electron flow and a veselago lens in graphene pn junctions. *Science*, 315:1252, 2007.

[27] J. Cserti, A. Csordás, and G. Dávid. Role of the trigonal warping on the minimal conductivity of bilayer graphene. *Phys. Rev. Lett.*, 99:066802, 2007.

[28] S. Datta. *Electronic transport in mesoscopic systems.* Cambridge university press, 1997.

[29] G. Dávid, P. Rakyta, L. Oroszlány, and J. Cserti. Effect of the band structure topology on the minimal conductivity for bilayer graphene with symmetry breaking. *Phys. Rev. B*, 85:041402, 2012.

[30] C. R. Dean, A. F. Young, I. Meric, C. Lee, L. Wang, S. Sorgenfrei, K. Watanabe, T. Taniguchi, P. Kim, and K. L. Shepard. Boron nitride substrates for high-quality graphene electronics. *Nature nanotechnology*, 5:722, 2010.

[31] R. Decker, Y. Wang, V. W. Brar, W. Regan, H.-Z. Tsai, Q. Wu, W. Gannett, A. Zettl, and M. F. Crommie. Local electronic properties of graphene on a bn substrate via scanning tunneling microscopy. *Nano letters*, 11:2291, 2011.

[32] G. Dresselhaus. Graphite landau levels in the presence of trigonal warping. *Phys. Rev. B*, 10:3602, 1974.

[33] M. S. Dresselhaus and G. Dresselhaus. Intercalation compounds of graphite. *Advances in Physics*, 30:139, 1981.

[34] M. Evaldsson, I. V. Zozoulenko, H. Xu, and T. Heinzel. Edge-disorder-induced anderson localization and conduction gap in graphene nanoribbons. *Phys. Rev. B*, 78:161407, 2008.

[35] B. E. Feldman, J. Martin, and A. Yacoby. Broken-symmetry states and divergent resistance in suspended bilayer graphene. *Nature Physics*, 5:889, 2009.

[36] R. Ferone, J. R. Wallbank, V. Zólyomi, E. McCann, and V. I. Falko. Manifestation of lo–la phonons in raman scattering in graphene. *Solid State Communications*, 151:1071, 2011.

[37] F. Freitag, J. Trbovic, M. Weiss, and C. Schönenberger. Spontaneously gapped ground state in suspended bilayer graphene. *Phys. Rev. Lett.*, 108:076602, 2012.

[38] V. Gasparian, T. Christen, and M. Büttiker. Partial densities of states, scattering matrices, and green's functions. *Phys. Rev. A*, 54:4022, 1996.

[39] A. K. Geim and K. S. Novoselov. The rise of graphene. *Nature materials*, 6:183, 2007.

[40] F. Guinea, M. I. Katsnelson, and A. K. Geim. Energy gaps and a zero-field quantum hall effect in graphene by strain engineering. *Nature Physics*, 6:30, 2009.

[41] M. Y. Han, B. Özyilmaz, Y. Zhang, and P. Kim. Energy band-gap engineering of graphene nanoribbons. *Phys. Rev. Lett.*, 98:206805, 2007.

[42] J. Hicks, A. Tejeda, A. Taleb-Ibrahimi, M. S. Nevius, F. Wang, K. Shepperd, J. Palmer, F. Bertran, P. Le Fèvre, and J. Kunc. A wide-bandgap metal-semiconductor-metal nanostructure made entirely from graphene. *Nature Physics*, 2012.

[43] J. H. Ho, Y. H. Chiu, S. J. Tsai, and M. F. Lin. Semimetallic graphene in a modulated electric potential. *Phys. Rev. B*, 79:115427, 2009.

[44] D. R. Hofstadter. Energy levels and wave functions of Bloch electrons in rational and irrational magnetic fields. *Phys. Rev. B*, 14:2239, 1976.

[45] B. Hunt, J. D. Sanchez-Yamagishi, A. F. Young, M. Yankowitz, B. J. LeRoy, K. Watanabe, T. Taniguchi, P. Moon, M. Koshino, and P. Jarillo-Herrero. Massive Dirac fermions and hofstadter butterfly in a van der waals heterostructure. *Science*, 340:1427, 2013.

[46] S. V. Iordanski and A. E. Koshelev. Dislocations and localization effects in multivalley conductors. *ZhETF Pis ma Redaktsiiu*, 41:471, 1985.

[47] M. I. Katsnelson, K. S. Novoselov, and A. K. Geim. Chiral tunnelling and the klein paradox in graphene. *Nature Physics*, 2:620, 2006.

[48] E. Kim, T. Yu, E. Sang Song, and B. Yu. Chemical vapor deposition-assembled graphene field-effect transistor on hexagonal boron nitride. *Applied Physics Letters*, 98:262103, 2011.

[49] K. S. Kim, Y. Zhao, H. Jang, S. Y. Lee, J. M. Kim, K. S. Kim, J.-H. Ahn, P. Kim, J.-Y. Choi, and B. H. Hong. Large-scale pattern growth of graphene films for stretchable transparent electrodes. *Nature*, 457:706, 2009.

[50] M. Kindermann, B. Uchoa, and D. L. Miller. Zero-energy modes and gate-tunable gap in graphene on hexagonal boron nitride. *Phys. Rev. B*, 86:115415, 2012.

[51] M. Kindermann, B. Uchoa, and D. L. Miller. Zero-energy modes and gate-tunable gap in graphene on hexagonal boron nitride. *Phys. Rev. B*, 86:115415, 2012.

[52] R. d. L. Kronig and W. G. Penney. Quantum mechanics of electrons in crystal lattices. *Proceedings of the Royal Society of London. Series A*, 130:499, 1931.

[53] M. Kruczyński, J. Wallbank, and V. I. Fal'ko. Bilayer graphene heterostructures with hbn: Interplay between misalignment, interlayer asymmetry, and trigonal warping. *arXiv preprint arXiv:1304.1734*, 2013.

[54] C. Lee, X. Wei, J. W. Kysar, and J. Hone. Measurement of the elastic properties and intrinsic strength of monolayer graphene. *science*, 321:385, 2008.

[55] Y. Lemonik, I. L. Aleiner, C. Toke, and V. I. Fal'ko. Spontaneous symmetry breaking and lifshitz transition in bilayer graphene. *Phys. Rev. B*, 82:201408, 2010.

[56] N. Levy, S. A. Burke, K. L. Meaker, M. Panlasigui, A. Zettl, F. Guinea, A. H. Castro Neto, and M. F. Crommie. Strain-induced pseudo–magnetic fields greater than 300 tesla in graphene nanobubbles. *Science*, 329:544, 2010.

[57] T. C. Li and S.-P. Lu. Quantum conductance of graphene nanoribbons with edge defects. *Phys. Rev. B*, 77:085408, 2008.

[58] X. Li, X. Wang, L. Zhang, S. Lee, and H. Dai. Chemically derived, ultrasmooth graphene nanoribbon semiconductors. *Science*, 319:1229, 2008.

[59] Y. Li, X. Jiang, Z. Liu, and Z. Liu. Strain effects in graphene and graphene nanoribbons: The underlying mechanism. *Nano Research*, 3:545, 2010.

[60] I. M. Lifshitz. Anomalies of electron characteristics of a metal in the high pressure region. *Sov. Phys. JETP*, 11:1130, 1960.

[61] F. Liu, P. Ming, and J. Li. *Ab initio* calculation of ideal strength and phonon instability of graphene under tension. *Phys. Rev. B*, 76:064120, 2007.

[62] J. M. B. Lopes dos Santos, N. M. R. Peres, and A. H. Castro Neto. Graphene bilayer with a twist: Electronic structure. *Phys. Rev. Lett.*, 99:256802, 2007.

[63] J. M. B. Lopes dos Santos, N. M. R. Peres, and A. H. Castro Neto. Continuum model of the twisted graphene bilayer. *Phys. Rev. B*, 86:155449, 2012.

[64] T. Low, F. Guinea, and M. I. Katsnelson. Gaps tunable by electrostatic gates in strained graphene. *Phys. Rev. B*, 83:195436, 2011.

[65] Y. Lu and J. Guo. Band gap of strained graphene nanoribbons. *Nano Research*, 3:189, 2010.

[66] J. L. Mañes. Symmetry-based approach to electron-phonon interactions in graphene. *Phys. Rev. B*, 76:045430, 2007.

[67] E. Mariani, A. J. Pearce, and F. von Oppen. Fictitious gauge fields in bilayer graphene. *Physical Review B*, 86:165448, 2012.

[68] J. Martin, B. E. Feldman, R. T. Weitz, M. T. Allen, and A. Yacoby. Local compressibility measurements of correlated states in suspended bilayer graphene. *Phys. Rev. Lett.*, 105:256806, 2010.

[69] A. S. Mayorov, D. C. Elias, M. Kruczyński, R. V. Gorbachev, T. Tudorovskiy, A. Zhukov, S. V. Morozov, M. I. Katsnelson, A. K. Geim, and K. S. Novoselov. Interaction-driven spectrum reconstruction in bilayer graphene. *Science*, 333:860, 2011.

[70] A. S. Mayorov, R. V. Gorbachev, S. V. Morozov, L. Britnell, R. Jalil, L. A. Ponomarenko, P. Blake, K. S. Novoselov, K. Watanabe, and T. Taniguchi. Micrometer-scale ballistic transport in encapsulated graphene at room temperature. *Nano letters*, 11:2396, 2011.

[71] E. McCann. Asymmetry gap in the electronic band structure of bilayer graphene. *Phys. Rev. B*, 74:161403, 2006.

[72] E. McCann, D. S. L. Abergel, and V. I. Falko. Electrons in bilayer graphene. *Solid state communications*, 143:110, 2007.

[73] E. McCann and V. I. Fal'ko. Landau-level degeneracy and quantum hall effect in a graphite bilayer. *Phys. Rev. Lett.*, 96:086805, 2006.

[74] E. McCann and V. I. Fal'ko. Landau-level degeneracy and quantum hall effect in a graphite bilayer. *Phys. Rev. Lett.*, 96:086805, 2006.

[75] E. R. Mucciolo, A. H. Castro Neto, and C. H. Lewenkopf. Conductance quantization and transport gaps in disordered graphene nanoribbons. *Phys. Rev. B*, 79:075407, 2009.

[76] M. Mucha-Kruczyński, I. L. Aleiner, and V. I. Fal'ko. Strained bilayer graphene: Band structure topology and landau level spectrum. *Phys. Rev. B*, 84:041404, 2011.

[77] M. Mucha-Kruczyński and V. I. Fal'ko. Pseudo-magnetic field distribution and pseudo-landau levels in suspended graphene flakes. *Solid State Communications*, 152:1442, 2012.

[78] K. Nakada, M. Fujita, G. Dresselhaus, and M. S. Dresselhaus. Edge state in

graphene ribbons: Nanometer size effect and edge shape dependence. *Phys. Rev. B*, 54:17954, 1996.

[79] Y. V. Nazarov and Y. M. Blanter. *Quantum transport: introduction to nanoscience.* Cambridge University Press, 2009.

[80] Z. H. Ni, H. M. Wang, Y. Ma, J. Kasim, Y. H. Wu, and Z. X. Shen. Tunable stress and controlled thickness modification in graphene by annealing. *ACS nano*, 2:1033, 2008.

[81] Z. H. Ni, H. M. Wang, Y. Ma, J. Kasim, Y. H. Wu, and Z. X. Shen. Tunable stress and controlled thickness modification in graphene by annealing. *ACS nano*, 2:1033, 2008.

[82] Z. H. Ni, T. Yu, Y. H. Lu, Y. Y. Wang, Y. P. Feng, and Z. X. Shen. Uniaxial strain on graphene: Raman spectroscopy study and band-gap opening. *Acs Nano*, 2:2301, 2008.

[83] Z. H. Ni, T. Yu, Y. H. Lu, Y. Y. Wang, Y. P. Feng, and Z. X. Shen. Uniaxial strain on graphene: Raman spectroscopy study and band-gap opening. *Acs Nano*, 2:2301, 2008.

[84] K. S. Novoselov, V. I. Fal'ko, L. Colombo, P. R. Gellert, M. G. Schwab, and K. Kim. A roadmap for graphene. *Nature*, 490:192, 2012.

[85] K. S. Novoselov, E. McCann, S. V. Morozov, V. I. Falko, M. I. Katsnelson, U. Zeitler, D. Jiang, F. Schedin, and A. K. Geim. Unconventional quantum hall effect and Berrys phase of 2π in bilayer graphene. *Nature Physics*, 2:177, 2006.

[86] T. Ohta, A. Bostwick, T. Seyller, K. Horn, and E. Rotenberg. Controlling the electronic structure of bilayer graphene. *Science*, 313:951, 2006.

[87] J. B. Oostinga, H. B. Heersche, X. Liu, A. F. Morpurgo, and L. M. K. Vandersypen. Gate-induced insulating state in bilayer graphene devices. *Nature materials*, 7:151, 2007.

[88] C. Ortix, L. Yang, and J. van den Brink. Graphene on incommensurate substrates: Trigonal warping and emerging Dirac cone replicas with halved group velocity. *Phys. Rev. B*, 86:081405, 2012.

[89] C.-H. Park, L. Yang, Y.-W. Son, M. L. Cohen, and S. G. Louie. New generation of massless Dirac fermions in graphene under external periodic potentials. *Phys. Rev. Lett.*, 101:126804, 2008.

[90] A. J. Pearce, F. Cavaliere, and E. Mariani. Conductance and shot noise in strained bilayer graphene. *Journal of Physics: Condensed Matter*, 25:375301, 2013.

[91] J. Pendry. Optics: Positively negative. *Nature*, 423:22, 2003.

[92] J. B. Pendry. Negative refraction makes a perfect lens. *Phys. Rev. Lett.*, 85:3966, 2000.

[93] V. M. Pereira and A. H. Castro Neto. Strain engineering of graphene's electronic structure. *Phys. Rev. Lett.*, 103:046801, 2009.

[94] V. M. Pereira, A. H. Castro Neto, and N. M. R. Peres. Tight-binding approach to uniaxial strain in graphene. *Phys. Rev. B*, 80:045401, 2009.

[95] L. A. Ponomarenko, R. V. Gorbachev, G. L. Yu, D. C. Elias, R. Jalil, A. A. Patel, A. Mishchenko, A. S. Mayorov, C. R. Woods, and J. R. Wallbank. Cloning of Dirac fermions in graphene superlattices. *Nature*, 497:594, 2013.

[96] C. J. Poole. On the applicability of the two-band model to describe transport across n–p junctions in bilayer graphene. *Solid State Communications*, 150:632, 2010.

[97] E. Prada, P. San-Jose, G. León, M. M. Fogler, and F. Guinea. Singular elastic strains and magnetoconductance of suspended graphene. *Phys. Rev. B*, 81:161402, 2010.

[98] D. Rainis, F. Taddei, M. Polini, G. León, F. Guinea, and V. I. Fal'ko. Gauge fields and interferometry in folded graphene. *Phys. Rev. B*, 83:165403, 2011.

[99] J. P. Robinson and H. Schomerus. Electronic transport in normal-conductor/graphene/normal-conductor junctions and conditions for insulating behavior at a finite charge-carrier density. *Phys. Rev. B*, 76:115430, 2007.

[100] R. Saito, G. Dresselhaus, and M. S. Dresselhaus. *Physical Properties of Carbon Nanotubes*. Imperial College Press, London, 1998.

[101] P. San-Jose, E. Prada, E. McCann, and H. Schomerus. Pseudospin valve in bilayer graphene: Towards graphene-based pseudospintronics. *Phys. Rev. Lett.*, 102:247204, 2009.

[102] H. Schomerus. Effective contact model for transport through weakly-doped graphene. *Phys. Rev. B*, 76:045433, 2007.

[103] H. Schomerus. Helical scattering and valleytronics in bilayer graphene. *Phys. Rev. B*, 82:165409, 2010.

[104] S. H. R. Sena, J. M. Pereira Jr, G. A. Farias, F. M. Peeters, and R. N. Costa Filho. The electronic properties of graphene and graphene ribbons under simple shear strain. *Journal of Physics: Condensed Matter*, 24:375301, 2012.

[105] R. Shankar. *Principles of quantum mechanics*, volume 233. Plenum Press New York, 1994.

[106] N. H. Shon and T. Ando. Quantum transport in two-dimensional graphite system. *JOURNAL-PHYSICAL SOCIETY OF JAPAN*, 67:2421, 1998.

[107] J. C. Slonczewski and P. R. Weiss. Band structure of graphite. *Phys. Rev.*, 109:272, 1958.

[108] I. Snyman and C. W. J. Beenakker. Ballistic transmission through a graphene bilayer. *Phys. Rev. B*, 75:045322, 2007.

[109] Y.-W. Son, S.-M. Choi, Y. P. Hong, S. Woo, and S.-H. Jhi. Electronic topological transition in sliding bilayer graphene. *Phys. Rev. B*, 84:155410, 2011.

[110] Y.-W. Son, M. L. Cohen, and S. G. Louie. Energy gaps in graphene nanoribbons. *Phys. Rev. Lett.*, 97:216803, 2006.

[111] H. Suzuura and T. Ando. Phonons and electron-phonon scattering in carbon nanotubes. *Phys. Rev. B*, 65:235412, 2002.

[112] R. C. Tatar and S. Rabii. Electronic properties of graphite: A unified theoretical study. *Phys. Rev. B*, 25:4126, 1982.

[113] S. P. Timoshenko and J. N. Goodier. Theory of elasticity. *International Journal of Bulk Solids Storage in Silos*, 1:567, 2011.

[114] M. Tinkham. *Group theory and quantum mechanics*. DoverPublications. com, 1964.

[115] T. Tudorovskiy, K. J. A. Reijnders, and M. I. Katsnelson. Chiral tunneling in single-layer and bilayer graphene. *Physica Scripta*, T146:014010, 2012.

[116] J. Velasco Jr, L. Jing, W. Bao, Y. Lee, P. Kratz, V. Aji, M. Bockrath, C. N. Lau, C. Varma, and R. Stillwell. Transport spectroscopy of symmetry-broken insulating states in bilayer graphene. *Nature nanotechnology*, 7:156, 2012.

[117] M. A. H. Vozmediano, M. I. Katsnelson, and F. Guinea. Gauge fields in graphene. *Physics Reports*, 496:109, 2010.

[118] H. W., T. Taychatanapat, A. Hsu, K. Watanabe, T. Taniguchi, P. Jarillo-Herrero, and T. Palacios. Bn/graphene/bn transistors for rf applications. *Electron Device Letters, IEEE*, 32:1209, 2011.

[119] K. Wakabayashi and T. Aoki. Electrical conductance of zigzag nanographite ribbons with locally applied gate voltage. *International Journal of Modern Physics B*, 16:4897, 2002.

[120] K. Wakabayashi, K. Sasaki, T. Nakanishi, and T. Enoki. Electronic states of graphene nanoribbons and analytical solutions. *Science and Technology of Advanced Materials*, 11:054504, 2010.

[121] K. Wakabayashi and M. Sigrist. Zero-conductance resonances due to flux states in nanographite ribbon junctions. *Phys. Rev. Lett.*, 84:3390, 2000.

[122] P. R. Wallace. The band theory of graphite. *Phys. Rev.*, 71:622, 1947.

[123] J. R. Wallbank, A. A. Patel, M. Kruczyński, A. K. Geim, and V. I. Fal'ko. Generic miniband structure of graphene on a hexagonal substrate. *Phys. Rev. B*, 87:245408, 2013.

[124] R. T. Weitz, M. T. Allen, B. E. Feldman, J. Martin, and A. Yacoby. Broken-symmetry states in doubly gated suspended bilayer graphene. *Science*, 330:812, 2010.

[125] M. L. Williams. Stress singularities resulting from various boundary conditions in angular corners of plates in extension. *J. appl. Mech*, 19(4):526, 1952.

[126] J. Xue, J. Sanchez-Yamagishi, D. Bulmash, P. Jacquod, A. Deshpande, K. Watanabe, T. Taniguchi, P. Jarillo-Herrero, and B. J. LeRoy. Scanning tunnelling microscopy and spectroscopy of ultra-flat graphene on hexagonal boron nitride. *Nature materials*, 10:282, 2011.

[127] M. Yankowitz, J. Xue, D. Cormode, J. D. Sanchez-Yamagishi, K. Watanabe, T. Taniguchi, P. Jarillo-Herrero, P. Jacquod, and B. J. LeRoy. Emergence of superlattice Dirac points in graphene on hexagonal boron nitride. *Nature Physics*, 8:382, 2012.

[128] Y. Zhang, T.-T. Tang, C. Girit, Z. Hao, M. C. Martin, A. Zettl, M. F. Crommie, Y. R. Shen, and F. Wang. Direct observation of a widely tunable bandgap in bilayer graphene. *Nature*, 459:820, 2009.

[129] Y. Zheng and T. Ando. Hall conductivity of a two-dimensional graphite system. *Phys. Rev. B*, 65:245420, 2002.

[130] O. C. Zienkiewicz and R. L. Taylor. *The finite element method*, volume 3. McGraw-Hill London, 1977.